UNIVERSITY OF CALIFORNIA

Los Angeles

On the Mesoscale Structure and Dynamics of Precipitating Stratocumulus

A dissertation submitted in partial satisfaction of the
requirements for the degree Doctor of Philosophy
in Atmospheric Sciences

by

Verica Savic-Jovcic

2008

The dissertation of Verica Savic-Jovcic is approved.

James C. McWilliams

Robert G. Fovell

Steven A. Margulis

Bjorn B. Stevens, Committee Chair

University of California, Los Angeles

2008

DEDICATION

mojim dragim roditeljima

List of Figures

List of Tables

ACKNOWLEdGMENTS

Most of the material in Chapter 3 is reproduced from Savic-Jovcic and Stevens (2007) (copyright by the American Meteorological Society, AMS) and is used in this dissertation by permission of the publisher. The authors are thankful to Axel Seifert for access to his original microphysical code, as well as his council regarding its use. Andrew Ackerman and Margreet van Zanten are thanked for their careful work in preparing such an interesting case for further study. Two anonymous reviewers and Robert Wood are thanked for their insightful and constructive suggestions on an earlier draft of this work. Computational resources were made available by NCAR and San Diego Supercomputer Center (SDSC). Financial support has been provided by NSF Grants ATM-0342625, 0336849, 9985413.

Some of the material in Appendix A is reproduced from Lenschow et al. (2007) (copyright by the American Meteorological Society, AMS) and is used in this dissertation by permission of the publisher. The authors are grateful to John Kalogiros, Marie Lothon, and the two anonymous reviewers for their helpful comments. The NCAR Research Aviation Facility supported this work by providing improved data sets and assisting in elucidating errors and limitations in the current C-130 air motion sensing system. This work has been supported by NCAR, NSF Grants ATM-0336849 and ATM-0097053, and NASA grant NAG512559.

Among numerous reasons for being grateful to my advisor, Bjorn Stevens, I would like to especially thank him for opening a door into the world of research. His willingness to take me under his wing allowed me to experience the life of a researcher in its fullness: from the excitement of flying throughout the night while measuring the properties of surrounding turbulent air, to the delight of running simulations on supercomputers and the satisfaction of publishing as a leading author. I deeply respect his openness for new ideas while at the same time assuring consistency in the thought process. His broad interests have exposed me to an enormous range of research topics and tools, for which I am exceptionally appreciative. I am also thankful for his modeling work, which is a foundation to my work, and all his attempts to make me a better writer and communicator.

I also wish to thank to my committee members, Jim McWilliams, Rob Fovell and Steve Margoulis, for their comments and suggestions on this dissertation. I would like to thank Donald Lenschow, Chin-Hoh Moeng and Jim McWilliams for sharing their enormous experience and knowledge about turbulence and our ability to observe and characterize it, as well as for their guidance on choosing a research path. Numerous conversations with Margreet van Zanten have been particularly instructive, as they always helped me improve the understanding of a problem, or overcoming of one. The GCSS boundary layer working group is thanked for formulating and providing a case study on which my dissertation was built. Work on this dissertation would not have been possible had it not been supported by Pauley Fellowship from UCLA, NSF (contract numbers ATM-9985413, ATM-0342625 and ATM-0097053) and supercomputing centers at NCAR and UCSD.

Special thanks are reserved for my colleagues and friends at UCLA, whose support and friendship have shaped not only my experience of graduate school, but me as a person for the rest of my life. Chris Holloway, Brian Medeiros, Mimi Hughes, Brian Kahn and Louise Nuijens, through endless hours of discussions of our work have enlightened many dark alleys of unknown and made it actually fun exploring far corners.

My bridges to this new world have been Raffaella D'Auria and Simona Bordoni, who, by recognizing connections between my new and old experiences, always revealed the beauty of the unfamiliar to me and offered a safe place for return. Simona in particular has been my cohort throughout all the milestones of graduate school and I could not be more grateful for having her to be the one. Margreet van Zanten and Eftyhia Zesta showed me that a successful researcher can be a great mom too, for which I am particularly thankful as it gives me guidance and hope that I could do the same.

I would like to thank my family and friends in what used to be Yugoslavia while I was growing up. Without my numerous cousins, aunts and uncles I would have never been so loved, used to teasing and prepared for accepting a criticism as a learning tool. Having my friends there helped me discover my potentials for understanding and explaining complicated concepts in more widely comprehensible terms, which encouraged me to explore a life outside of safe and known. I wish to thank my sister and our parents for letting me go on this challenging journey and for following me regardless of where it took me. It requires a great courage to let the youngest one go so far and I am grateful to all three of them for having it. I am especially appreciative of my father, whose ability to scrutinize the events that surround us and pose the questions in a constructive manner have framed my thinking and cultivated a scientist in me. I still grieve after his sudden sickness and death four years ago and wish he was here to enjoy the fruit of his garden. This dissertation is my present to him and my mom who makes a home for me wherever I bring her.

I am especially thankful to my husband, Slobodan Jovcic, for his trust in me and my ability to overcome any challenge that comes into a way. Sometimes, in the swirl of life, it is easy to forget how far one can reach and Jovča in his own way always makes me aware of how far we have gotten. I am also extremely thankful to Jovča for a genuine happiness in all of my successes. His enthusiasm for all good that happens to me is an indispensable part of my life and the work you are about to read.

Verica Savic-Jovcic

Los Angeles, California

December, 2007

VITA

June 1, 1973	Born, Belgrade, Yugoslavia
1999	Diploma in Meteorology Faculty of Physics, University of Belgrade, Yugoslavia
2000/2003	Pauley Fellowship University of California, Los Angeles
2001-2002	Teaching Assistant Department of Atmospheric and Oceanic Sciences University of California, Los Angeles
2003	M.S. in Atmospheric Sciences Department of Atmospheric and Oceanic Sciences University of California, Los Angeles
2000-2007	Research Assistant Department of Atmospheric and Oceanic Sciences University of California, Los Angeles
2008	Ph.D. in Atmospheric Sciences Department of Atmospheric and Oceanic Sciences University of California, Los Angeles

PUBLICATIONS AND PRESENTATIONS

Verica Savic-Jovcic, B. Stevens, D. H. Lenschow, 2002: Estimating divergence and vorticity from aircraft data in the stratocumulus topped boundary layer. 15th Symposium on Boundary Layers and Turbulence, Wageningen, The Netherlands, Amer. Meteor. Soc., 112-113

B. Stevens, Donald H. Lenschow, Gabor Vali, Hermann Gerber, A. Bandy, B. Blomquist, J. L. Brenguier, C. S. Bretherton, F. Burnet, T. Campos, S. Chai, I. Faloona, D. Friesen, S. Haimov, K. Laursen, D. K. Lilly, S. M. Loehrer, Szymon P. Malinowski, B. Morely, M. D. Petters, D. C. Rogers, L. Russell, V. Savic-Jovcic, J. R. Snider, D. Straub, Marcin J. Szumowski, H. Takagi, D.C. Thorton, M. Tschudi, C. Twohy, M. Wetzel, and M. C. vanZanten, 2003: Dynamics and Chemistry of Marine Stratocumulus. Bull. Amer. Meteorol. Soc. 84, 579-593

Bjorn Stevens, Anton Beljaars, Simona Bordoni, Christopher Holloway, Martin Koehler, Steven Krueger, Verica Savic-Jovcic and Yunyan Zhang, 2007: On the structure of the lower troposphere in the summertime stratocumulus regime of the northeast Pacific, Mon. Weath. Rev., 135, 985-1005

Lenschow, Donald H., Verica Savic-Jovcic and Bjorn Stevens, 2007: Divergence and Vorticity from Aircraft Air Motion Measurements. J. Atmos. and Ocean. Tech., 24, 2062-2072

Verica Savic-Jovcic and Bjorn Stevens, 2007: The structure and mesoscale organization of precipitating stratocumulus. J. Atmos. Sci., in press (August 2007)

A. S. Ackerman, M. van Zanten, B. Stevens, V. Savic-Jovcic, C. S. Bretherton, A. Chlond, J.-C. Golaz, H. Jiang, M. Khairoutdinov, S. K. Krueger, D. C. Lewellen, A. Lock, C.-H. Moeng, K. Nakamura, M. Ovtchinnikov, M. D. Petters, J. R. Snider, S. Weinbrecht, and M. Zulauf, 2007: Large-eddy simulations of a drizzling, stratocumulus-topped marine boundary layer. in preparation for Mon. Wea. Rev.

ABSTRACT OF THE DISSERTATION

On the Mesoscale Structure and Dynamics of Precipitating Stratocumulus

by

Verica Savic-Jovcic

Doctor of Philosophy in Atmospheric Sciences

University of California, Los Angeles, 2008

Professor Bjorn B. Stevens, Chair

Drizzle is commonly observed in the stratocumulus-topped boundary layers. Yet, the clear interpretation of how it interacts with the boundary-layer turbulence is lacking. In attempt to bridge the existing gap, this dissertation investigates the role of drizzle in the mesoscale structure and dynamics of the flow in the drizzling stratocumulus-topped boundary layer. Large-eddy simulations on a heretofore unimaginably large domains are utilized. To study the structure, a bulk microphysical parameterization is introduced, while for the analysis of dynamics, a horizontally uniform forcing is imposed.

Precipitating stratocumulus are shown to be realistically represented in the simulations. In particular, tendency of the boundary layer to transition to more cumulus-coupled circulation, with locally elevated cloud tops and patches of anomalous sub-cloud equivalent potential temperature in the vicinity of precipitating clouds are captured. The observed tendency for precipitation to be associated with the emergence of a more marked mesoscale circulation and a general reduction in cloudiness is also captured. Moreover, it is shown that the evaporation of precipitation is critical to the observed flow transition, and that the sub-cloud circulations (cold pools) that originate in such a process appear to play a vital role in shaping the structure of both the sub-cloud layer and regions of new convection. Furthermore, localized interactions of drizzle and boundary-layer flow are shown to lead to the development of the mesoscale flow and cloud organization, where the cloud organization follows the flow organization. It is also confirmed that the energetics and reorganization of the flow toward the larger scales in the drizzling STBL are driven by the budget of liquid-water potential temperature.

Chapter 1

Introduction

1.1. Motivation

Stratocumulus clouds (Sc) are a significant component of the Earth's climate system, which is mostly recognized through their radiative properties. By increasing the reflection of incoming Solar radiation (*i.e.*, albedo) and negligibly affecting the outgoing long-wave radiation, Sc cool the underlying surface. Additionally, because Sc cover large areas (about a third of the Earth's oceans, Ackerman et al. 1993) this cooling effect has global implications. Moreover, the impact on the climate is emphasized with an abundance of Sc over subtropical oceans, where the Earth annually receives large amounts of incoming solar radiation. Modeling studies suggest that the global cooling resulting from a modest increase in the Sc global coverage could offset the expected warming from doubling the concentration of carbon dioxide in the atmosphere Slingo (1990). This climatological importance of Sc encourages a fundamental understanding of the processes, both on the large and the small scales, involved in the formation, sustainability and dissipation of these clouds.

My personal motivation for analyzing Sc comes from my interest in turbulent processes dominating planetary boundary layers where these clouds reside. These are convective boundary layers, with buoyancy fluxes being the dominant source of turbulence. Stratocumulus, being the manifestation of a phase change of water vapor, have multiple interactions with the buoyancy fluxes, and I am interested in learning about them. Besides, during my participation in DYCOMS-II (the second DYnamics and Chemistry Of the Marine Stratocumulus field study, described in detail in Stevens et al. 2003b) I became fascinated with these clouds and their environment, as I was able to see them from up close, where one gets lost in their cotton-like puffiness, and from far away, where one cannot see the end of the puffy blanket that covers the ocean. I also experienced their radiative effect in the early morning when the sky above them turns its colors from deep blue to lighter shades, then orange and finally to the bright blue, while underneath this puffy deck of stratocumulus the color changes from dark to light gray and has nothing to do with the brightness above them. The most impressive encounter with the Sc for me was during the night, when the only way to be aware of their magnitude is to follow the computer screens and see the measurements of various instruments mounted on an airplane that flies for hours up and down and far away. This fascination temporarily diverted my attention from the modeling study of turbulence to the estimation of the environmental conditions favorable to Sc and resulted in my first graduate research experience, where I attempted to estimate the large-scale divergence from the wind measurements obtained during DYCOMS-II. Results of that work are partially incorporated in the set up for large-eddy simulations (LES) of the drizzling stratocumulus that are a subject of the major part of my dissertation work, where I return to addressing the questions related to the boundary-layer processes, and in particular, the role of precipitation.

The following sections of this chapter review the literature pertinent to the dynamics of precipitating Sc and provide a basis for discussions presented in this dissertation. The introduction is closed with a summary of the scope of the work presented in the body of this dissertation.

1.2. Nocturnal Non-Precipitating Stratocumulus-Topped Boundary Layer

Stratocumulus are low-level clouds with a generally stratiform appearance and underlying cellular structure. They develop at the top of thermodynamically distinct maritime atmospheric boundary layers. Such boundary layers form in conditions where the overlying free troposphere is much warmer than the underlying cold ocean. Being more similar in characteristics to the latter they are often capped by a strong temperature inversion. These conditions are typically met in the eastern regions of subtropical oceans. There, the upwelling in the ocean brings cold water to the surface, while in the atmosphere, subsidence enhances warming of the overlying air, which contributes to the thermal contrast between the ocean and the overlying atmosphere. Klein and Hartmann (1993) used the difference between the potential temperature, θ, at 700 mb and its value at the surface, to quantify the ocean-atmosphere thermal contrast. They called this difference the lower tropospheric stability (LTS), and showed that the Sc prevalence correlates well with the LTS on seasonal and interannual time scales. In addition, Klein et al. (1995) suggested that the local cloud amount is better correlated with the LTS 24 h upwind than with the local LTS, which indicates the importance of cold advection not only for the Sc formation (which was suggested by Paluch and Lenschow 1991) but also for their sustainability.

Large-scale atmospheric conditions in the regions of subtropic marine stratocumulus are dominated by the climatologically stationary high pressure systems, *i.e.*, anticyclones. There, the prevailing vertical motion is weak subsidence, whose rate constrains the depth of the boundary layer and, therefore, the height of the stratocumulus cloud tops. This considerable influence on the development of the marine stratocumulus-topped boundary layer (STBL) makes the quantification of the subsidence rates very desirable. At the same time, though, low subsidence rates of typically less than 0.01 m s^{-1} makes its measurement quite challenging (Lenschow et al. 2007). Some of the issues related to these measurements are discussed in the appendix A. In the following subsection, however, we focus on the typical structure and processes within the STBL.

a. *Typical Mean Structure of the Stratocumulus-Topped Boundary Layer*

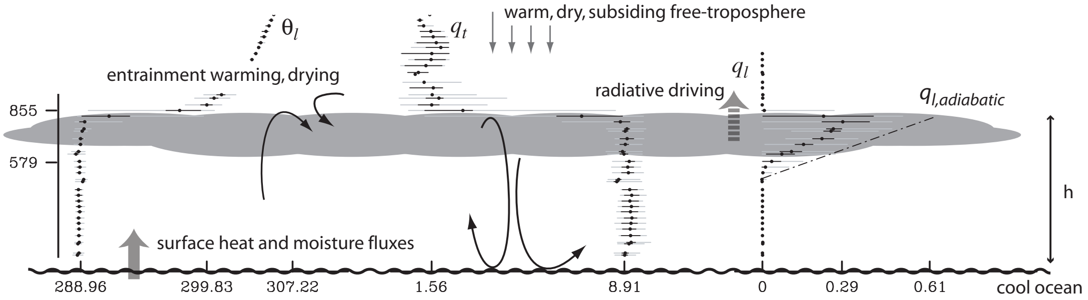

Figure 1.1: Cartoon of well mixed, non-precipitating, stratocumulus topped boundary layer, overlaid with profiles of θ_l, r_t and r_l. The profiles, as well as the heights of cloud base and top, are constructed from data from RF01 of DYCOMS-II. The dash-dot line represents the adiabatic liquid water content. (from Stevens 2004)

Most of the conceptual and theoretical descriptions of the STBL involve a well mixed, radiatively driven and non-precipitating STBL, as depicted in a cartoon in Fig. 1.1. The cartoon illustrates the mean structure, environmental conditions and the most important processes that occur within the STBL. Data presented in the cartoon were collected during the first research flight (RF01) of DYCOMS-II. Displayed are adiabatic invariants (liquid water potential temperature, $\theta_l \sim \theta \exp(\frac{-Lr_l}{c_pT})$, which describes the thermal structure, and total water mixing ratio, r_t, which represents the moisture content within the layer; L, c_p and T are the enthalpy of vaporization, isobaric specific heat and temperature, respectively), as well as the liquid water mixing ratio, r_l, which indicates the presence of the cloud.

As shown in Fig. 1.1, the STBL is relatively shallow, cool and moist, and capped by a warmer, drier and gently subsiding free atmosphere. The transition of θ_l and r_t between their boundary-layer and free-tropospheric values is sharp, with a strong increase in temperature (temperature inversion) and decrease in moisture and liquid water content. The inversion, which is very stable, resists mixing of the STBL with free-tropospheric air and is the largest constituent of the lower tropospheric stability defined by Klein and Hartmann (1993) and discussed above.

Profiles of θ_l and r_t in Fig. 1.1 show that the STBL is vertically well mixed, which results from convective turbulence within the STBL. The main source of turbulence in the STBLs is the infrared radiative cooling at the top of the cloud, unlike in the dry convective boundary layers (DCBLs), where the dominant source of turbulence is the surface heat flux. This essential difference in the sources of the turbulent motion leads to the difference in the peak time for the maximum strength of turbulence between the two regimes. In the STBL, turbulence is at its maximum during the night, when the cooling is the strongest due to the lack of offset by the solar radiation, while for the DCBL it peaks in the daytime, when the land surface is warmest. Many modeling and theoretical studies have taken advantage of the absence of the solar radiation in the nocturnal conditions preferred by the STBL, while most of the observations were performed during the day. This discrepancy between the observations and theory was bridged during DYCOMS-II, whose data are presented in the cartoon and utilized in this study.

Basic processes within the STBL are also illustrated in Fig. 1.1. In addition to mixing of STBL air, turbulent motions within the STBL entrain quiescent free tropospheric air into the STBL by engulfing and subsequently mixing it into the STBL air. From the perspective of the STBL mass budget, the diabatic growth of the STBL by entrainment counteracts the large-scale subsidence. From the heat budget point of view, warming due to entrainment competes with the cloud-top cooling and surface heat fluxes. As for the moisture budget, entrainment acts against the surface moisture fluxes and dries the STBL. Note that both the source (radiative cooling) and the sink (entrainment) of turbulence act at the same interface – cloud top – which makes the study of the STBL challenging in many respects.

Surface heat and moisture fluxes are additional sources of turbulence, but generally less important. As Bretherton and Wyant (1997) showed, when these sources become important, our view of the well mixed STBL becomes questionable.

The well-mixed state of adiabatic invariants within the STBL is actually a foundation for our theoretical understanding of the STBL. Mixed-layer theory, originally developed by Lilly (1968) and with only modest elaborations in the meantime, is still providing advantageous insights in the STBL properties. In that framework, a parameterization of entrainment is necessary to close the system of equations describing the evolution of the STBL bulk properties. This parameterization has been a topic of an ongoing research ever since the first formulation of the Mixed-Layer Model in the late sixties. Most of the attempts to parameterize entrainment are related to the ability of the system to do work, the stability of the capping inversion layer and the effect of non-turbulent processes in deepening the layer (Stevens 2002). To help understanding the entrainment process itself, there have also been numerous observational studies determining the entrainment rate (*e.g.*, Stevens et al. 2003a; Faloona et al. 2005; Gerber et al. 2005). Studies of entrainment have identified the buoyancy reversal as another subject of importance in studying the STBL (Lilly 1968; Stevens 2002). Buoyancy reversal occurs when the mixture of entrained and cloudy air, due to the evaporation of cloud droplets, becomes colder and denser than the surrounding cloudy air and therefore less buoyant. It is argued that this process can lead to the Sc breakup by initiating the runaway feedback between the entrainment, downdrafts and turbulence (Randall 1980; Deardorff 1980; MacVean and Mason 1990). This instability of Sc to the entrainment is called Cloud-Top Entrainment Instability (CTEI) and has been a subject of both theoretical and observational studies. Although the observations show evidence of solid cloud decks even when the criteria for the CTEI is satisfied (Stevens et al. 2003a; Duynkerke et al. 2004), some general circulation models use it for the parameterization of Sc (*e.g.*, Medeiros et al. 2005). This discrepancy between the modeling of larger scales and observed Sc drives further interest in the subject. However, entrainment is not the only question one could ask when describing the STBL. In the following subsection, we note other topics of interest for better understanding of the STBL.

b. *Additional Topics of Active Research*

There are other processes commonly present in the STBL that are not outlined in the cartoon in Fig. 1.1 and discussion in 1.2.a. These include solar radiation and precipitation, all of which are also subjects of active research efforts. Solar radiation acts to reduce the cloud-top radiative cooling and imprints a distinct diurnal cycle on the cloud layer, in which clouds are observed to dissipate during the day and deepen through the night (*e.g.*, Zhang et al. 2005). Attempts to explain the effects of solar radiation only in terms of well mixed STBL have faced some unresolved issues, which led to initial development of the theoretical framework of decoupled boundary layers (Turton and Nicholls 1987). Decoupling of the STBL is argued to occur when the cloud-top radiative cooling is no longer the dominant source of turbulence, and turbulence actually has to do work against the buoyancy at the top of the subcloud layer to maintain a well mixed STBL. In particular, Turton and Nicholls (1987) suggest that because the cloud top radiative cooling gets offset by the short-wave cloud warming and therefore the main source of turbulence gets reduced, the circulation within the STBL weakens and eventually separates into two sublayers where it is driven by different sources, by surface fluxes in the subcloud layer and by the weak radiative cooling in the cloud layer. The theoretical framework of decoupling has been further explored by Bretherton and Wyant (1997), who discuss decoupling in terms of increased surface fluxes that drive stronger entrainment that offsets the radiative cooling and therefore warms up the whole layer, setting up conditions for more vigorous cumulus dynamics.

One could argue that precipitation has the most peculiar place in studying the STBL (vanZanten et al. 2005). It has been observed since the early eighties (*e.g.*, Brost et al. 1982a), but its theoretical framework is still in the state of infancy. This dissertation aims to develop our understanding of the structure and processes within the drizzling STBL. Simply speaking, this dissertation reports on research that tries to understand how drizzle changes the cartoon in Fig. 1.1. In the following section we describe in more detail the questions we ask.

1.3. Drizzling Stratocumulus

Drizzle, being a diabatic process, impacts the structure of the STBL by altering the structure of the Sc and the characteristics of the low-level flow. Simple models suggest that drizzle alters the cloud albedo by influencing cloud fraction (Albrecht 1989) and cloud thickness (Pincus and Baker 1994). Through this process, drizzle plays a key role in the second indirect effect of aerosols on the Earth's climate. Drizzle also provides a link between cloud microphysical processes and boundary-layer circulations (Paluch and Lenschow 1991; Stevens et al. 1998) by changing the thermodynamic properties of the STBL. The perception that stratocumulus is sensitive to drizzle motivates our attempts to better understand the precipitating STBL.

From observations, it is well established by now that the STBL has a tendency to precipitate, and at times quite significantly, so that its kinematic flux is comparable to the turbulent fluxes of liquid water (Brost et al. 1982a,b; Nicholls 1984) and its energetic flux can be comparable to the radiative flux at the cloud top (vanZanten et al. 2005). Recent field campaigns, DYCOMS-II and EPIC (Stevens et al. 2003b; Bretherton et al. 2004, respectively), provide the clearest picture yet that drizzle is prevalent, long-lasting and locally intense (vanZanten et al. 2005; Comstock et al. 2005). In addition, they also isolate the drizzle-related atmospheric phenomena that further encourages our attempts to understand its effects on the STBL.

a. *Structure of the drizzling STBL*

In addition to the above characteristics of drizzle itself, observational data also suggest that drizzle is associated with changes in the STBL structure. For instance, Paluch and Lenschow (1991) show that temperature and moisture are correlated on scales commensurate with the PBL depth, but anticorrelated on a mesoscale in the presence of drizzle. Similarly, Comstock et al. (2005) report higher horizontal variability in thermodynamic properties during drizzling events. A representation of this change in terms of equivalent potential temperature, $\theta_e \sim \theta \exp(\frac{Lr_v}{c_pT})$, is observed by vanZanten et al. (2005) who diagnose pools of elevated θ_e within the sub-cloud layer in those regions associated with drizzle. In respect to the dynamic changes, vanZanten et al. (2005) also report reduced variance of vertical velocity, but locally higher cloud tops in the presence of drizzle. They actually conceptualize the observed change in circulation in a cartoon in Fig. 1.2.

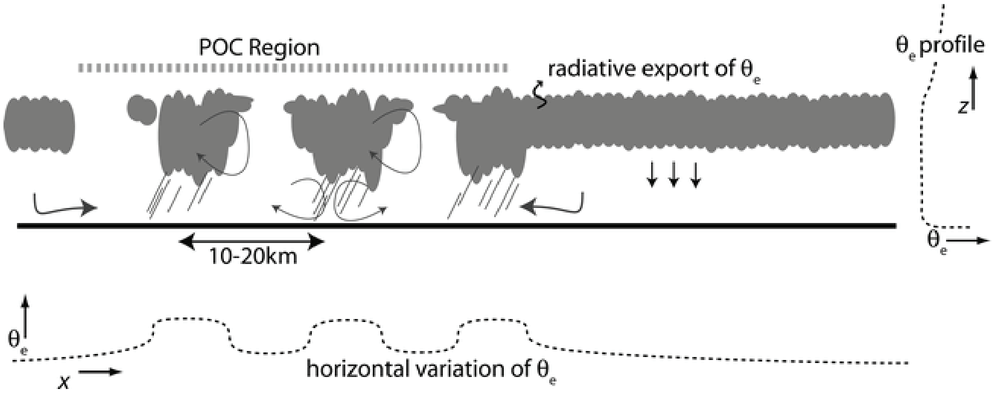

Figure 1.2: Conceptual diagram of drizzling and neighboring non-drizzling region with a schematic of the horizontal and vertical variations in θ_e and inferred mesoscale circulations. From vanZanten et al. (2005).

The cartoon also incorporates the impact of drizzle on the cloud organization, which is observed in the cloud planform. In particular, through the emergence of areas of relatively cloud-free air in regions associated with the development of precipitation (*e.g.*, Stevens et al. 2005b; Sharon et al. 2006). As the satellite image in Fig. 1.3 depicts, these 'clearings' (sharply bounded darker regions on the figures) actually represent clouds with a different organizational pattern. While Sc, the high albedo region, can be characterized as organizing in a closed cellular pattern, with brighter (thicker) clouds at the center of the cell and dimmer (thinner) or no cloud at the cell edges, the 'clearings' are more characteristic of an open cellular pattern where clouds define the cell boundaries and the cloud-free regions the cell center. Although these formations have attracted the interest of satellite meteorologists for a long time (see reviews by Agee et al. 1973; Garay et al. 2004), the analysis of *in situ* data collected in their vicinity has only recently been conducted (Stevens et al. 2005b; vanZanten et al. 2005). To emphasize both the compact structure of these features in reference to the surrounding Sc decks and their distinctive convective organization Stevens et al. (2005b) named them 'pockets of open cells (POCs)', a terminology we adopt here. These structures were also described by Sharon et al. (2006), but as elongated patches of broken clouds with cellular structure on the order of 10-20 km, which they call rifts.

In addition to the visible images, POCs can also be detected from nocturnal satellite imagery by locating the small values of the difference between the 11 and 4 μm brightness temperature, which allows for the continuous detection of the evolution of POCs. Stevens et al. (2005b) observed that POCs are coherent, long-lived (longer than 10 h) and advected by the mean boundary layer wind, while Comstock et al. (2005) report that the distinct drizzle cells within the POCs last for about 2 h. Radar reflec-

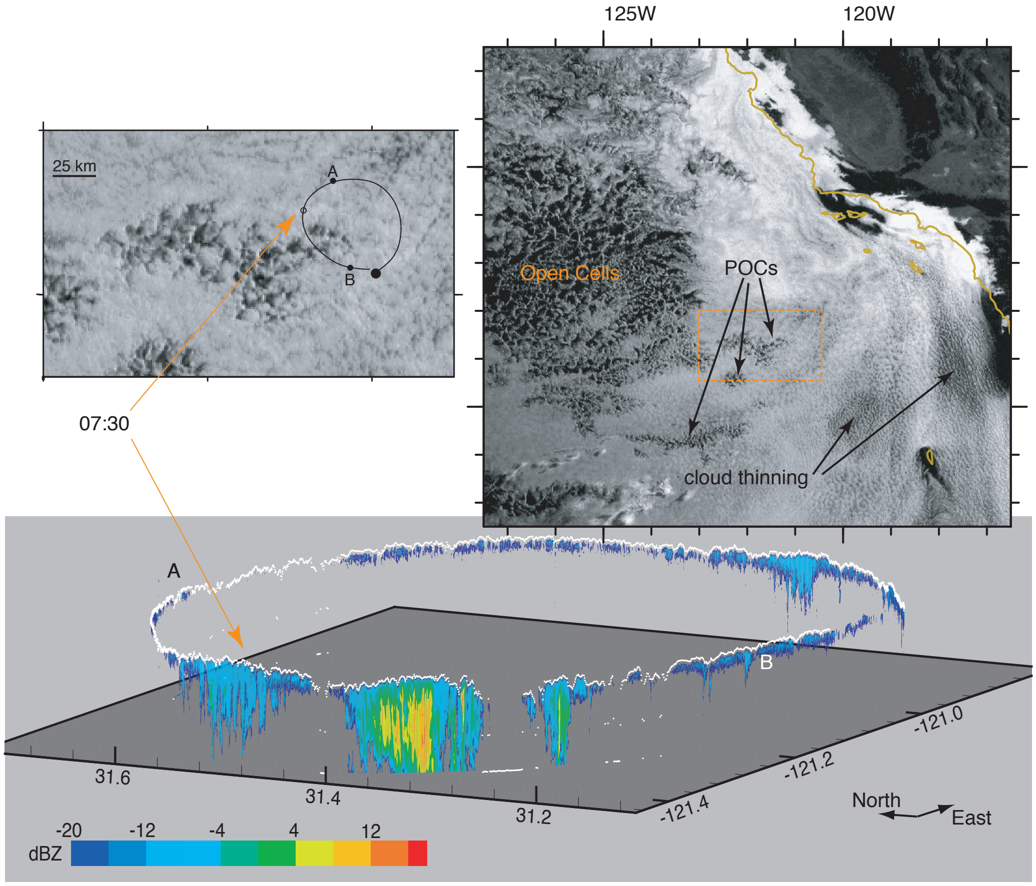

Figure 1.3: More detailed view of the cellular structure of POCs. A region of open cellular convection has dark cell interiors, with bright cell walls, whereas the closed cellular convection of Sc has bright cells with darker cell walls. From Stevens et al. (2005b)

tivities (Fig. 1.3) and *in situ* data imply that the precipitation in the sampled STBL is localized in the walls (high albedo region) of the open cellular convection and that the drizzle rate at the surface exceeds more than twice the surface evaporation, while the drizzle rate at the cloud base is twice to three times larger than the surface values. Because precipitation at such rates can completely dry out the cloud in about 10 min, if not replenished, Stevens et al. (2005b) concluded that POCs represent stable flow configurations that organize to maintain the moisture supply to the precipitating cell boundaries.

Theoretical work, recognizing drizzle as an additional diabatic forcing, strives to understand the mechanisms by which it reorganizes the PBL circulations. Large-eddy simulations (LES) by Stevens et al. (1998) suggest that drizzle promotes cumulus-type circulations by increasing the buoyancy of downdrafts and therefore stabilizing the STBL, thus promoting decoupling and less deepening of the STBL. Subsequent studies arrive at similar conclusions, although they debate the details of how precipitation interacts with and stabilizes the circulation (e.g. Ackerman et al. 2004). However, the small domain and coarse vertical grid used in most existing numerical studies raise questions about the reliability of their results. Because the simulations with relatively small computational domains essentially sample a single cumulus element in the decoupled regime, they are subject to concerns that the statistics of the flow are insufficiently sampled to draw reliable conclusions, and that the small domain inappropriately filters mesoscale circulations thought to be associated with drizzle. Also, the coarse vertical grid raises questions about the fidelity of the simulations.

Given the limitations of observations and previous modeling work, as well as the emergence of new datasets (*i.e.*, DYCOMS-II and EPIC), it becomes interesting to revisit the question of how drizzle affects the evolution of the SBTL. Questions that emerge in this context include: What is the structure of the drizzling STBL in terms of cloud and circulation organization? To what degree does LES capture the observed characteristics of the drizzling STBL? What makes the circulation in the drizzling STBL so long-lived and self-sustaining? And, what generates the pools of elevated θ_e in the drizzling STBL? In Chapter 3, we attempt to answer these questions.

To do so requires capturing the scales developing in the drizzling STBL (mesogamma, Orlanski 1975), which demands LES with a much larger, yet finer in the vertical, computational mesh than previously used. The simulation domain of 25.5 × 25.5 × 1.5 km proves to be large enough to resolve numerous precipitating clouds that organize into loose networks reminiscent of open and closed cells, yet small enough to be computationally manageable. To achieve such a wide range of scales requires us to use a bulk parameterization of microphysical processes, as it is computationally much less demanding than an explicit representation of microphysical processes. Bulk microphysical schemes are also advantageous because they allow one to more readily isolate physical processes, such as the evaporation of rain drops. The initial conditions and forcings for the simulations are based on the second research flight (RF02) of DYCOMS-II (vanZanten and Stevens 2005). This configuration has recently been used as a case study for an LES intercomparison by the GCSS (GEWEX [Global Energy and Water Cycle EXperiment] Cloud System Study) boundary layer working group (Ackerman et al. 2007). Chapter 2 discusses the model characteristics and the settings in more details.

b. *Dynamics of the drizzling STBL*

Understanding how the drizzling STBL differs from a non-precipitating involves understanding the processes involved in the interaction of drizzle with the STBL dynamics. As mentioned above, drizzle is a diabatic process that alters the evolution of the SBTL thermodynamic properties. In doing so, it has the potential to change the structure of the cloud layer, and hence the radiative forcing. Both of these interactions affect the evolution of the STBL turbulent structure. The questions of how these effects relate and how drizzle interacts with other processes acting in the STBL are still open.

A conceptual model of the drizzle-induced cloud transformation developed by Paluch and Lenschow (1991) implies that drizzle interacts with the STBL turbulence mainly by stabilizing the subcloud layer through moistening and cooling, and that further development of trade cumulus results from the surface heating. Their study is based on *in situ* measurements, and thus would benefit from further studies using experiments with controlled conditions, in which the role of individual processes can be isolated.

The drizzle-induced decrease in cloud depth is argued by Pincus and Baker (1994) to be due to the decrease of the cloud-top height. As they argue, by affecting the energy budget drizzle reduces the entrainment rate and the STBL height. In their study Pincus and Baker (1994) used a mixed-layer model, which provides considerable insights, but also has some limitations. For instance the entrainment parameterization is still a topic of an ongoing research, and MLM results are sensitive to the choice of the entrainment parameterization (Stevens 2002). Pincus and Baker (1994) used one of the 'flux limiting' schemes, and therefore prevented the model from developing the decoupled state, which Stevens et al. (1998) show to happen at least locally. Nevertheless, their result that the cloud albedo susceptibility is affected by the propensity of cloud to drizzle is in agreement with observations, which leaves this problem open for further study, preferably including the full 3D STBL dynamics.

Indeed, many of these same questions motivated the work Stevens et al. (1998), in which they argued that the drizzle-caused transition from Sc to cumulus results from the consumption of the evaporative contribution to cloud base buoyancy fluxes through the removal of liquid water by precipitation. In their LES study Stevens et al.

(1998) showed that, in addition to the cooling and moistening of the subcloud layer, drizzle significantly increases the buoyancy of the downdrafts within the cloud layer. Because this stabilizing effect on downdrafts is apparent only if the level of saturation of the parcels within the downdrafts is above the cloud base, they named it 'potential buoyancy'. Their result can also be interpreted as a form of decoupling, insofar as the increase of the downdraft buoyancy suggests the decrease of the buoyancy flux below the mean cloud base. However, the question of the relative contribution of processes within the cloud versus subcloud layer remains open, as does the question of whether decoupling arguments along the lines proposed by Turton and Nicholls (1987); Bretherton and Wyant (1997, among the others) can be used to explain the results of the simulation. A question of decoupling is revisited in Chapter 4 by analyzing the simulations from Chapter 3 in a framework of the Mixed-layer Model. In particular, we investigate whether a mixed layer can be energetically consistent if it drizzles as much as the drizzling STBL described in Chapter 3, but otherwise evolves identically to the non-drizzlign STBL from Chapter 3.

Ackerman et al. (2004) clarify that the effect of drizzle on the liquid-water path (LWP), a proxy for Sc depth, is not vertically uniform. The response of LWP to the increase in drizzle intensity depends on the profile of the precipitation flux. Stronger drizzle at the surface decreases the LWP by simply removing the water from the cloud and the STBL in general. On the other hand, stronger drizzle at the cloud top may increase the LWP by reducing the entrainment of the overlaying drier air, which generally dilutes the cloud. This clarification further motivates exploration of possible spatial structures in the effect of drizzle on the dynamics of the STBL.

By focusing on different effects, each of these studies offers different mechanisms through which drizzle acts upon the STBL. One could imagine a somewhat more systematic view on these effects, for instance by attributing the effect of drizzle to effects felt throughout the depth of the STBL versus those that act differentially on the cloud and subcloud layers, or by trying to separate the relative importance of the moisture and heat budgets in explaining drizzle-induced changes to the circulation. Such a view is adopted in Chapter 4, where we artificially modify processes in the model so as to understand what aspects are essential in eliciting the responses we simulate.

In light of recent observations that emphasize the mesoscale organization of the drizzling STBL (Comstock et al. 2005; Stevens et al. 2005b), one could ask what effect the spatial distribution of drizzle has on these interactions. The questions raised here therefore need to be addressed with the large-domain simulations. However, to isolate specific aspects of drizzle effect, instead of expensive microphysics one can impose drizzle-mimicking, horizontally uniform forcing by prescribing heating and moistening profiles with the shape corresponding to the drizzle flux profile. The detailed description of these profiles is described in Chapter 2.

1.4. Summary

To summarize, this dissertation explores the environment, structure and dynamics of the drizzling STBL. In particular, the mesoscale structure and dynamics of the drizzling STBL are analyzed using a large-domain LES, which is described in Chapter 2. The structure, in terms of the development of distinctive mesoscale organizations is addressed in Chapter 3, where the cloud planform, the morphology of dynamic and thermodynamic fields and the pools of elevated θ_e in the drizzling STBL are investigated. Chapter 4 diagnoses the energetics of the drizzling STBL and studies those aspects of drizzle that are responsible for the structural changes occurring in its presence. Spatial structure of drizzle, as well as impact of drizzle on the θ_l and r_t budgets are explicitly examined to discern the particular manner in which drizzle interacts with the STBL dynamics. Concluding remarks are offered in Chapter 5.

In addition to the analysis of the drizzling STBL, in appendix A some issues related to the estimates of divergence from the aircraft wind measurements are examined. This study is not constrained to only the drizzling STBL, in part because there are no indications of the differences in the large scale environment between precipitating and non-precipitating STBL, and in part because the challenge of the measurements precludes such distinctions. Among many reasons, this study is included in this dissertation because defining divergence is one of the environmental forcings required for the numerical studies discussed in the main chapters.

Chapter 2

Methodology

In this chapter we describe the methods used to investigate the mesoscale structure and dynamics of the drizzling STBL. In particular, the UCLA LES is utilized, which we outline it in Section 2.1. To explore the structure of the drizzling STBL, the UCLA LES was modified by incorporating a bulk microphysical parameterization, described in Section 2.2. For the study of dynamics, though, a horizontally uniform forcing discussed in Section 2.3 is imposed. We also describe the set up of numerical experiments in Section 2.4 and a methodology of conditional sampling in Section 2.5.

2.1. UCLA LES

The base UCLA LES code is described by Stevens et al. (2005a). It solves the Ogura and Phillips (1962) anelastic equations around a reference state chosen to be in hydrostatic and geostrophic balance and to satisfy the ideal gas law for a dry atmosphere. The radiative forcing is parameterized with a simple model of the net longwave radiative flux developed by Stevens et al. (2005a). It captures the effects of cloud-top cooling, cloud-base warming, and cooling in the free troposphere just above the cloud top, as well as allowing for the spatio-temporal variability in radiation due to the cloud structure. Sub-filter fluxes are modeled using the Smagorinsky model. For scalars, however, the diffusivities are forced to decay exponentially with height. This forces all the dissipation to be carried by the advection schemes at distances more than a few hundred meters above the surface. Stevens et al. (2005a) showed that for the UCLA LES, this choice of representation of sub-filter fluxes, while ad hoc, gives the most appropriate representation of entrainment and hence better simulations of stratocumulus as compared to observations. Detailed expressions for the model equations are presented in Appendix B.1.

2.2. Microphysics

To study the mesoscale structure of the drizzling STBL, and with a mind toward computational efficiency, we introduce a simple model of microphysical processes that follows Seifert and Beheng (2001, 2006). Because our interest is in the impact of precipitation on the surrounding flow, but not in the details of its formation, we introduce a simplification to the Seifert and Beheng approach by maintaining cloud water in equilibrium with a specified number concentration. Thus, only two additional prognostic equations must be solved – one for drizzle mass mixing ratio r_p and another for number mixing ratio of drizzle n_p – these being:

$$\begin{aligned}\frac{\partial r_p}{\partial t} &= C_{cc}(r_c, r_p; m^*, n_c) + C_{pc}(r_c, r_p) + E(r_p, r_v, r_s, n_p) + \\ &+ \frac{\partial}{\partial x_3} v_r(r_p, n_p) r_p - v_i \frac{\partial r_p}{\partial x_i} + \frac{\partial}{\partial x_i}\left(K_h \frac{\partial r_p}{\partial x_i}\right)\end{aligned} \tag{2.1}$$

$$\begin{aligned}\frac{\partial n_p}{\partial t} &= \frac{1}{m^*} C_{cc}(r_c, r_p; m^*, n_c) + C_{pp}(r_p, n_p) + \frac{1}{m_p} E(r_p, r_v, r_s, n_p) + \\ &+ \frac{\partial}{\partial x_3} v_n(r_p, n_p) n_p - v_i \frac{\partial n_p}{\partial x_i} + \frac{\partial}{\partial x_i}\left(K_h \frac{\partial n_p}{\partial x_i}\right).\end{aligned} \tag{2.2}$$

Here, microphysical processes are represented in terms of intra- and interspecies interactions of the cloud droplets and drizzle drops, neglecting breakup. For instance, C_{cc} and C_{pp} denote intraspecies interactions of cloud droplets and drizzle drops (i.e. auto-conversion and self-collection) respectively, while C_{pc} denotes interspecies interactions of drizzle drops and cloud droplets (i.e. accretion). E symbolizes evaporation, which in our representation excludes ventilation effects. Sedimentation utilizes mass and number weighted mean fall velocities, denoted respectively by v_r and v_n. In the above, r_c and n_c are mass and number mixing ratios for the cloud droplets respectively, r_c is constrained by the equilibrium assumption (assuming uniformity of thermodynamic quantities within a grid cell) and n_c is specified. The parameter m_p is mean mass of drizzle drops, r_s is saturation mixing ratio, r_v is water vapor mixing ratio, v_i is a resolved-scales velocity vector in a tensor form, and K_h is eddy diffusivity. Detailed expressions for C_{cc}, C_{pc}, C_{pp}, E, v_r and v_n, as well as specific parameter values used by the scheme, are presented in appendix B.2.

To fully account for effects of precipitation on the STBL (Ackerman et al. 2004) we allow cloud droplets to sediment in all of our simulations following prescription from the Ninth GCSS comparison (Ackerman et al. 2007), as discussed in appendix B.2. However, the geometric standard deviation of droplet sizes, which enter into the calculation of the sedimentation flux, is set at 1.2, rather than the GCSS value of 1.5, because the former agreed better with the measurements.

Being a diabatic process, drizzle affects the dynamics of the STBL through its impact on the thermodynamic fields: total-water mixing ratio r_t and liquid-water potential temperature θ_l. If drizzle reaches the surface, it dries and warms the whole PBL. Likewise, locally, the drizzle flux $(v_r(r_p, n_p)r_p)$ divergence and the divergence of cloud-droplet sedimentation flux $(F_c(r_c, n_c))$ contribute to the change in θ_l and r_t, and thus introduce a source term in the equations for θ_l and r_t as discussed in Abstract B.1, where $F_d = v_r(r_p, n_p)r_p + F_c(r_c, n_c)$.

2.3. Imposed Horizontally Uniform Forcing

To study the effect of the localized nature of drizzle on the dynamics of the STBL, we perform simulations in which the locally-defined sum of drizzle and cloud-droplet sedimentation fluxes F_d is replaced by the horizontally uniform forcing that corresponds to the domain-mean precipitation. In particular, formulation of the horizontally uniform forcing is based on the domain-mean profile of the precipitation flux in the simulation of the drizzling STBL described in Chapter 3. Following the shape of that precipitation flux profile, we define a profile of the forcing flux as:

$$F_{d_{if}} = P_0 - P_{cb} \exp((z_i - z)/\lambda_1) + (P_{cb} - P_0) \exp(((z_i - \Delta) - z)/\lambda_2), \tag{2.3}$$

where P_0 is the surface value of flux, P_{cb} is the cloud-base flux value, z_i is the inversion height, and Δ is an averaged cloud depth, while λ_1 and λ_2 are tuning parameters. Values for P_0, P_{cb} and Δ are determined from the above-mentioned drizzling simulation to be 68 W m^{-2}, 25 W m^{-2}, and 240 m, respectively. Values for z_i are locally determined during the simulation, and tuning parameters are set to λ_1 = 0.04 and λ_2 = 0.005 to follow the curvature of the precipitation profile at the top of the cloud and in the subcloud. Finally, to provide consistency in units, $F_{d_{if}}$ is scaled with L_v to satisfy the Eqs. (B.7) and (B.8).

2.4. Setup for the Numerical Experiments

Our analysis of the mesoscale structure of the drizzling STBL is centered around a comparison of three simulations: the Non-drizzling Simulation (hereafter NS), in which precipitation development is restricted by prescribing a large cloud-droplet number concentration (200 cm^{-3}), the Drizzling Simulation (hereafter DS), where drizzle readily develops because the number concentration of cloud droplets is kept artificially low (25 cm^{-3}), and the Drizzling Without Evaporation Simulation (hereafter DWES), where evaporation of drizzle is inhibited ($E(r_p, r_v, r_s, n_p) = 0$).

The study of the dynamics of the drizzling STBL relies on the comparison of the NS and DS with three additional simulations: Mean-Forcing Simulation (hereafter MFS), where the horizontally uniform forcing, which resembles mean forcing due to drizzle, is imposed on the non-precipitating STBL, the Mean-Heating Simulation (hereafter MHS), in which the horizontally-uniform forcing affects only the θ_l budget, and the Mean-Moistening Simulation (hereafter MMS), where the horizontally-uniform forcing impacts only the r_t budget.

The mesh of the UCLA LES is regular in the horizontal and stretched in the vertical, with the grid spacing adjusted to match the specifications for the Ninth GCSS LES comparison (Ackerman et al. 2007) — the horizontal mesh is 50 m, and the vertical mesh is 5 m at the surface and in the 125-m deep layer near inversion, with $\sin^2$ stretching in the PBL interior and increasing above the PBL to reach 80 m at the top of the domain. Four simulations (NS, DS, DWES and MFS) are performed both on a 512 × 512 × 97 point mesh (large-domain simulations) and on a 128 × 128 × 97 point mesh (a GCSS-prescribed domain size), while MHS and MMS are performed only on the GCSS-prescribed domain size. All simulations last for 6 h of simulation time, with a time step of 0.5 s. The runs are a bit longer than in some previous work, both to follow the GCSS prescription (Ackerman et al. 2007) and to allow time for any possible larger scale circulations to develop in the large-domain simulations.

The large-scale forcings and initial and boundary conditions for these simulations also follow the configuration for the experiments in the Ninth GCSS comparison (Ackerman et al. 2007). In particular, the Coriolis parameter f is determined at 31.5°N and the large-scale divergence is set to 3.75$\cdot 10^{-6}$ s^{-1}. The initial vertical profile for momentum is linear with a surface value of 3 m s^{-1} for the zonal and 9 m s^{-1} for the meridional component, increasing with height at a rate of 4.3 m s^{-1} km^{-1} and 5.6 m s^{-1} km^{-1}, respectively. Initial profiles of θ_l and r_t are well mixed within the STBL with values of 288.3 K and 9.45 g kg^{-1}. At the inversion, there is a sharp jump to values of 295 K and 5 g kg^{-1}, and above the inversion there is a slight increase of θ_l and decrease of r_t, according to $(z - z_i)^{1/3}$ and $3(1 - \exp((z_i - z)/500))$ for θ_l and r_t, respectively, where z is height in units of m and $z_i = 795$ m is the initial inversion height.

Boundary conditions include surface pressure set to 1017.8 hPa, sensible and latent heat fluxes prescribed to 16 and 93 W m^{-2}, respectively, and surface stress fixed at $u_* = 0.25$ m s^{-1} and distributed into upward momentum fluxes with the bulk formulae, where the wind components and the magnitude of the horizontal wind are defined locally. By specifying surface fluxes we attempt to mimic the case of a Lagrangian evolution of the layer as it advects over progressively warmer waters. Such a strategy is also in accord with the sampling strategy employed during DYCOMS-II. For computational expediency the upper 250 m of the domain consists of a sponge layer with a damping coefficient that increases linearly with height to a value of 10^{-2} s^{-1}. Lateral boundary conditions are periodic and the domain is subjected to a Galilean transform of 5 and -5.5 m s^{-1} in the x and y directions, respectively.

2.5. Conditional Sampling

Analysis of the pools of elevated θ_e in Section 3.2 is founded on the conditional composites of thermodynamic and momentum fields, where the conditions are defined in terms of θ_e and drizzle intensity. We name these composites the "θ_e cells" and the "drizzling cells" and formulate them following Schmidt and Schumann (1989), who define the conditional composites of the updraft cells to analyze the coherent features in the convective boundary layer.

Here, we present the steps taken in the construction of the cells. First, at a chosen height level, we locate the centers of the cells by identifying the local maxima of precipitation and θ_e that are stronger than prescribed threshold values, which we refer to as events. Then, we isolate the strongest events by excluding the nearby weaker ones. To keep statistics comparable between the different simulations and the two types of cells, we choose only the 40 strongest maxima at the three selected independent times toward the end of simulations (5, 5.5 and 6 hour). For precipitation we choose a threshold of 2 mm day^{-1}, and for θ_e, 316 K. Both cells are defined here based on the fields at 200 m height, and the exclusion distance we present here is 1600 m, which corresponds to about two boundary-layer heights in the DS. After isolating the events, we define the area encompassed by each cell as a cylinder with the given radius and height through the whole domain, such that there is no overlaying between the surrounding cells. We do so by mapping each point in the domain to its closest cell center and excluding all the points that are more than 5 km away from the closest cell center. The conditional composites of w, θ_e, precipitation and r_l presented in section 3.2 are finally constructed by first binning the fields by the horizontal distance from the centers of the cells and then averaging the values in each bin.

Chapter 3

Structure and Mesoscale Organization of the Drizzling STBL

As unveiled in the introduction, an onset of drizzle is recognized to introduce the modifications in the STBL structure and organization. In this Chapter, we discuss these changes. In particular, evolution and structure of drizzling STBL is presented in section 3.1. We proceed with the analysis of the pools of elevated θ_e, a feature of drizzling STBL observed during DYCOMS-II, in section 3.2. This is followed by the discussion of scales of variance and transition in the cloud field in section 3.3. The Chapter is closed with the summary in 3.4. The material presented in this Chapter is adopted from Savic-Jovcic and Stevens (2007).

3.1. Structure and evolution of the flow

The development of drizzle in stratocumulus leads to profound changes in both the cloud amount and organization. Although our simulations are for nocturnal stratocumulus, thereby circumventing any possible interactions with solar-radiative processes, we visualize these changes in terms of the cloud albedo, A, which we calculate following the simple prescription (*e.g.*, Zhang et al. 2005)

$$A = \frac{\tau}{6.8 + \tau}, \tag{3.1}$$

where $\tau = 0.19\mathcal{L}^{5/6}N_c^{1/3}$ is the optical depth, N_c is the cloud-droplet number concentration, and $\mathcal{L} = \int_0^\infty r_l \rho_0 dz$ is the liquid-water path. Snapshots of A at the end of each simulation are shown in Fig. 3.1. Each can be argued to provide a compelling, but markedly different realization of the stratocumulus-topped boundary layer.

In the absence of drizzle (Fig. 3.1, NS), the cloud adopts a closed-cell planform (e.g. Comstock et al. 2005; Agee 1984), where the cell centers are characterized by high reflectivity and cell walls are loci of low reflectivity, and in places may even be cloud free. Overall, the albedo for NS is relatively uniform with a domain-averaged value near 75%. In contrast, the development of significant drizzle (surface rain rates in the DS and DWES average near 1 mm day^{-1}, roughly corresponding to 30 W m^{-2}) leads to a much less reflective and spatially more variable cloud layer (Fig. 3.1, DS). The domain-averaged albedo in DS falls to less than 35%, which is less than half its value in the absence of drizzle. About one-third of the reduction in the albedo can be attributed to the Twomey effect (reduced scattering in the presence of fewer drops); if the albedo in NS is recalculated with $N = 25$ cm^{-3} (commensurate with droplet concentrations in DS), it falls to just under 60%. Thus, the bulk of the changes in the albedo are due to changes in the amount and distribution of the cloud water.

Indeed, the DS is topologically distinct from the NS (Fig. 3.1). By this we mean that the shape of the probability distribution function of liquid water path (LWP), and hence albedo, differ qualitatively. This is evident both in the probability distribution function shown in Fig. 3.2, and in spatial distribution of albedo. In the former we note that while the overall distribution in the DS has shifted to the left, the emergence of a

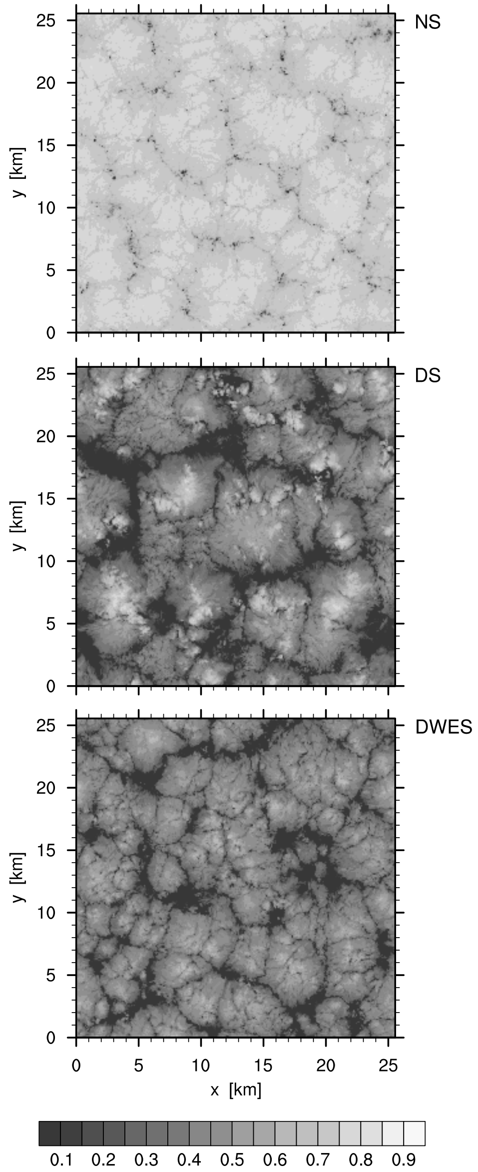

Figure 3.1: Albedo, as per Eq. (3.1), at the end of the 6^{th} h of simulations. From Savic-Jovcic and Stevens (2007).

long tail differentiates it from the other distributions. This is somewhat less evident in the albedo plots because the regions of highest LWP in the DS also have fewer drops than the NS. The shift of the distribution to the left in the DS and DWES reflects the

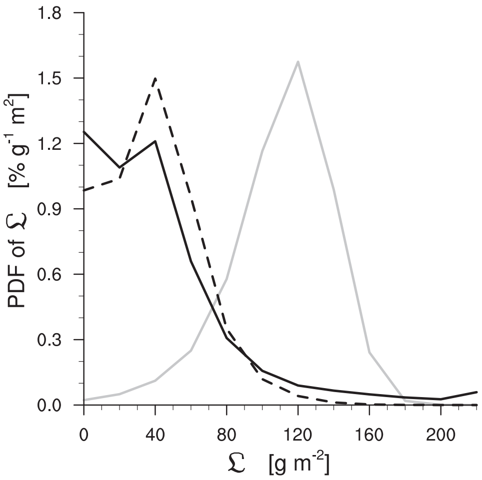

Figure 3.2: Distribution of liquid-water path in simulations: NS (solid gray line), DS (solid black line) and DWES (dashed black line). From Savic-Jovcic and Stevens (2007).

emergence of cloud-free regions in the precipitating simulations. And while all the simulations evince aspects of what is referred to as a closed-cellular structure, the high LWP cell centers in the DS are beginning to organize in loose networks that hint at an emergent open-cellular (bright walls, dim centers) pattern. These types of changes are consistent with behavior hinted at by previous simulations in relatively small domains (*e.g.,* Stevens et al. 1998) as well as observations contrasting precipitating versus non-precipitating layers of stratocumulus (*e.g.,* vanZanten et al. 2005; Comstock et al. 2005).

By preventing evaporation of precipitation-size drops in the DWES we both enhance the efficiency with which water is removed from the boundary layer, and inhibit the tendency of drizzle to stabilize the sub-cloud layer with respect to the cloud layer. So doing leads to a simulation whose reflectivities are reduced to values only marginally larger than for the DS, but which lack the underlying topological changes. Although the cloud field is more broken, there is little evidence of networks of high-reflectivity, such as might be associated with underlying cumuliform convection. This suggests that, at least for this case, the evaporation of precipitation plays an important role in reorganizing the circulation; and that, at least in the short term, this reorganization (embodied by compact regions of high reflectivity in the DS) has more to do with determining the overall albedo of the layer than does the tendency of drizzle to remove water from the cloud layer.

Our basis for associating drizzle with topological changes in the underlying flow is more readily evident in horizontal cross sections of θ_l', r_t' and w', both in the subcloud layer (Fig. 3.3) and in the cloud layer (Fig. 3.4). Here primes denote deviations from layer mean quantities. In the drizzling simulations (DS and DWES), these cross sections are overlaid with contours of spatially smoothed precipitation. Comparing the DS with the NS (Fig. 3.3) suggests that with the development of precipitation the open-cellular network of surface-bound r_t anomalies both intensifies and becomes more positively skewed. Regions of positive anomalies appear to be loci of strong upward motion, precipitation, and cooler air (hence significantly lowered condensation levels). In the absence of drizzle the flow shows a more familiar picture of radiatively driven stratocumulus, wherein w' is more finely grained (Figs. 3.3 and 3.4), with upward and downward motions of more commensurate strength (note the paucity of strong downdrafts in the precipitating simulations). And although even in the NS, the subcloud r_t' field evinces the underlying support for a more open-cellular structure, the imprint of such structure is less evident in the albedo.

A comparison of cross sections from the DS with those from the DWES (Figs. 3.3 and 3.4) suggests that the evaporation of drizzle is critical to these topological changes. In the absence of evaporation of precipitation-size drops, the open-cellular-

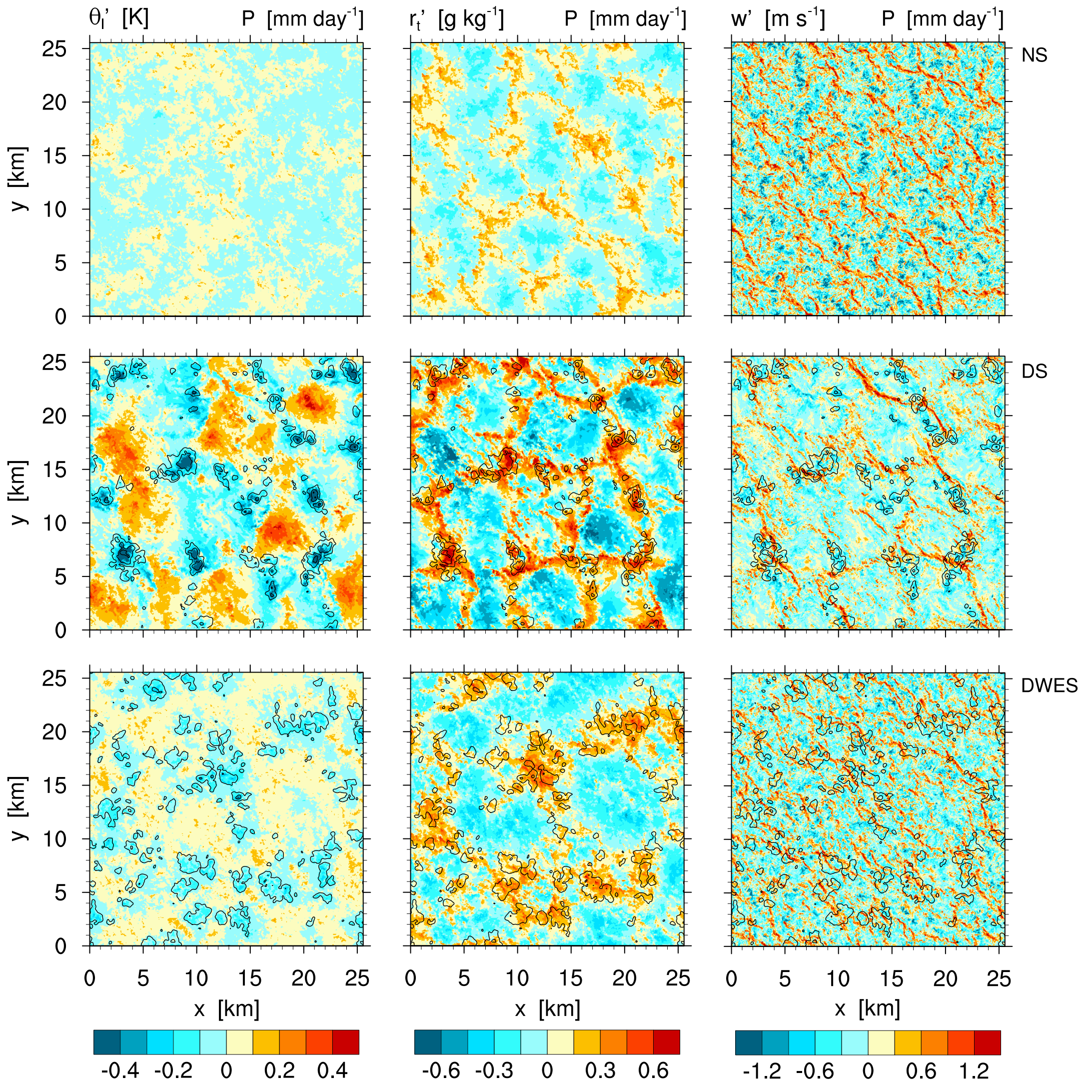

Figure 3.3: Planar view of instantaneous perturbations from the horizontal mean values of θ_l, r_t and w fields at 200-m level at the end of the 6^{th} h of three simulations. Precipitation contours that overlay the plots for DS and DWES are spatially-smoothed for clarity, and have values of 2, 10 and 30 mm day^{-1}. From Savic-Jovcic and Stevens (2007).

like network is much less evident. Regions of precipitation, which are more regularly patterned, concentrated, and associated with strong fluctuations in the sub-cloud thermodynamic structure in the DS, are more widespread, less intense, and less apparently

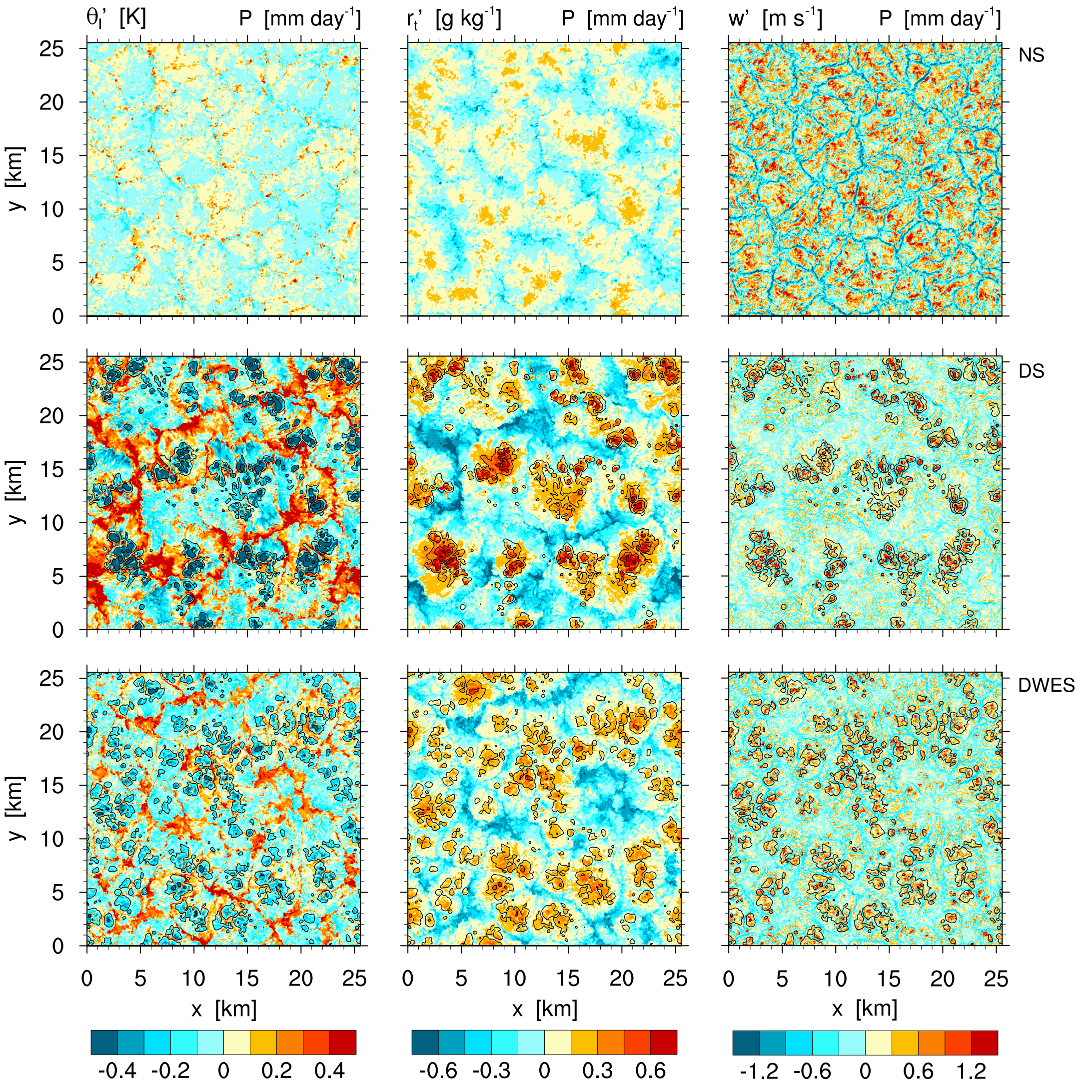

Figure 3.4: As in Fig. 3.3, but for 700-m level. From Savic-Jovcic and Stevens (2007).

organized in the DWES. Although the sub-cloud moisture field (middle column in Fig. 3.3) shows mesoscale structure in both simulations, the low-level moisture maxima along which convection appears to organize, are more diffuse in the DWES and more reminiscent of the patterns in the NS. As we shall see, this form of organization is more typical of well mixed stratocumulus layers, with relatively little differentiation between cloud base in up- and down-draft regions of the flow. In the precipitating simulations however, cloud base lowers in regions of precipitation, and raises away from the precipitating leading to a marked differentiation in cloud base. Such behavior is consistent with the visual record from the recent DOCIMS (Drizzle and Open Cells in Marine Stratocumulus) field study which used the new NCAR/NSF Gulfstream V to target precipitating open cells as well as the photographic evidence from EPIC.

Many of the above discussed aspects of the simulations are also evident in Fig. 3.5, which shows vertical cross sections (or slices) of w' and the equivalent potential temperature, θ_e, in each of the three simulations, with cloud-water and rain contours overlaid. Here the tendency of the DS to develop a circulation consisting of cumulus under stratocumulus is especially evident, with the precipitation strongly localized in the vicinity of updrafts rich in θ_e and a locally lower cloud base, *i.e.*, cumulus clouds. These cumulus clouds are noticeably associated with locally elevated cloud tops, a conspicuous feature of observations of precipitating boundary layers (*cf.*, Paluch and Lenschow 1991; Vali et al. 1998; Stevens et al. 2005b; Petters et al. 2006) that was not well reproduced in the relatively coarse vertical resolution simulations of Stevens et al. (1998). These vertical cross sections highlight the important role downdrafts play in the NS, as compared to updrafts which are more dominant in the circulation of the DS.

Some of the changes associated with precipitation can be efficiently summarized by mean vertical profiles of selected quantities. Figure 3.6 shows how precipitation leads to a substantially shallower boundary layer and a significant reduction in liquid water and cloud fraction. Peak values of layer-averaged liquid water are reduced by more than half. The development of a tail in the cloud fraction extending down to 400 m

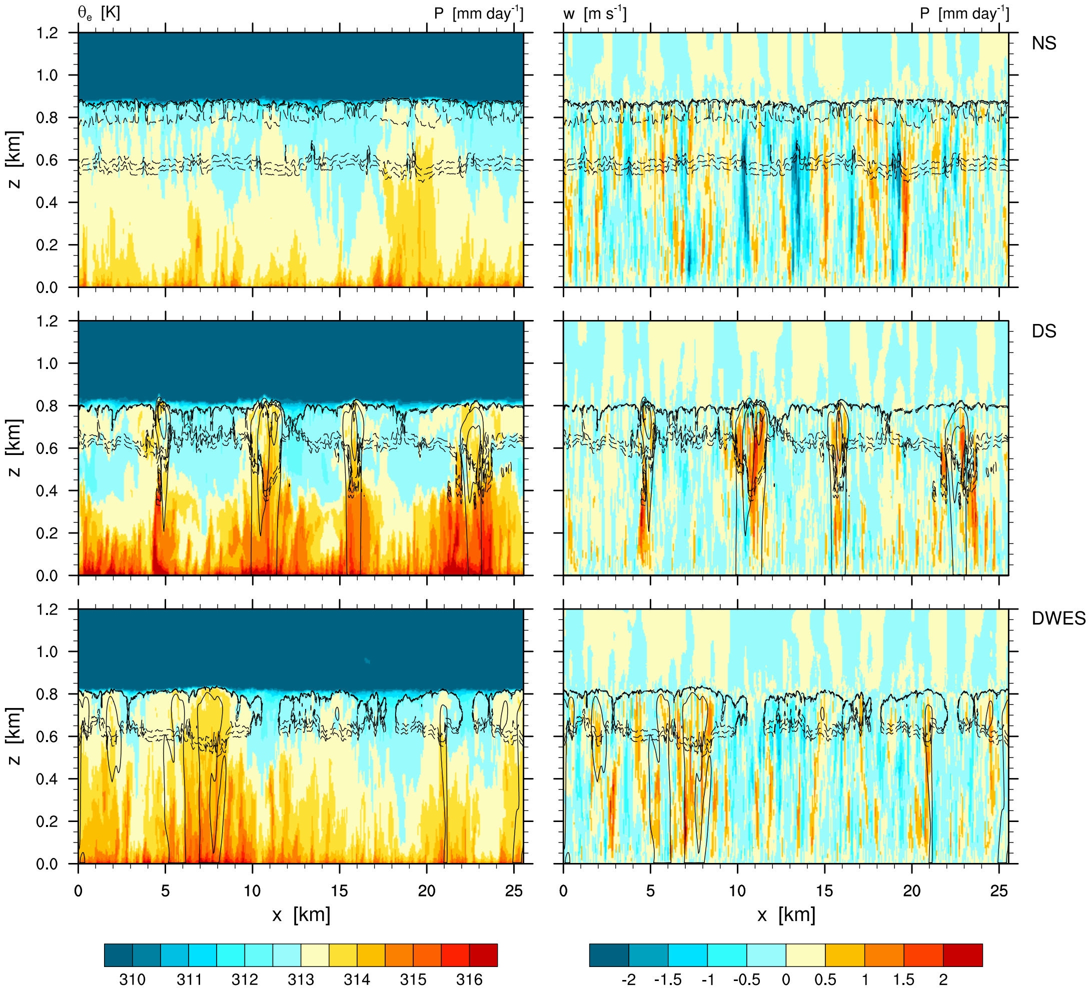

Figure 3.5: Vertical cross sections of instantaneous θ_e and w fields at $y = 45$ m at the end of the 6^{th} h of simulations, overlaid with dashed contours of r_c with values of 0.01, 0.05, 0.1 and 0.5 g kg^{-1}. Plots for DS and DWES are additionally overlaid with solid contours of precipitation with values of 2, 10 and 30 mm day^{-1}. From Savic-Jovcic and Stevens (2007).

and more pronounced gradients in thermodynamic quantities near this level, especially moisture (Siebesma et al. 2003), is often taken as a signature of more cumulus-coupled circulations. Because to a first approximation $\theta_e \approx \theta_l + (L/c_p)r_t$, the effects of the negative moisture gradients overwhelm the slight positive θ_l gradients, so that the θ_e profiles follow more closely those of r_t, consistent with the cross sections in Fig. 3.5.

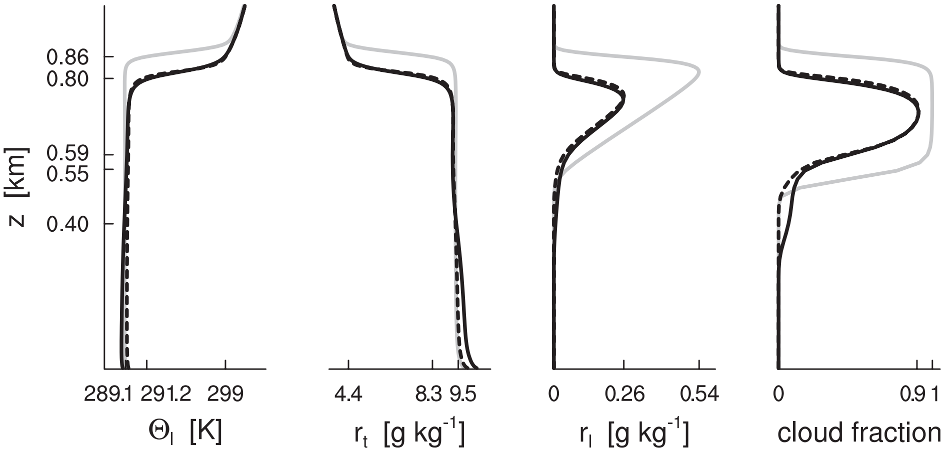

Figure 3.6: Mean profiles of θ_l, r_t, r_l and cloud fraction, panels from left to right respectively, averaged over the last two hours of the simulation. Lines as in Fig. 3.2. Top four values on y axis represent the corresponding two-hour average of time series of cloud-top and cloud-base heights for NS and DS. Bottom value on y axis represents the lowest height where the profile of r_l is greater than 0.01 g kg^{-1}. Values on the x axes are BL-averages and top-of-transition-layer values of θ_l and r_t for TDS, and maximum of r_l and cloud fraction within the boundary layer for NS and DS. From Savic-Jovcic and Stevens (2007).

The degree of differentiation between the cloud and sub-cloud layer thermodynamic quantities are, however, not nearly as large as in the simulations by Stevens et al. (1998). Whether or not they are in conflict with the observations of vanZanten et al. (2005), who do not find significant vertical differentiation between the cloud and sub-cloud layers thermodynamic properties, is more difficult to ascertain because of the sampling strategy employed in their observational strategy. These features are absent from the DWES.

The tendency of precipitation to suppress the growth of the boundary layer is consistent with the weaker circulations. Figure 3.7 shows that the peak values of $\overline{w'w'}$ are reduced by nearly a factor of three and have a more bimodal structure (with a local minimum near cloud base) in the presence of drizzle. Such a profile of the vertical

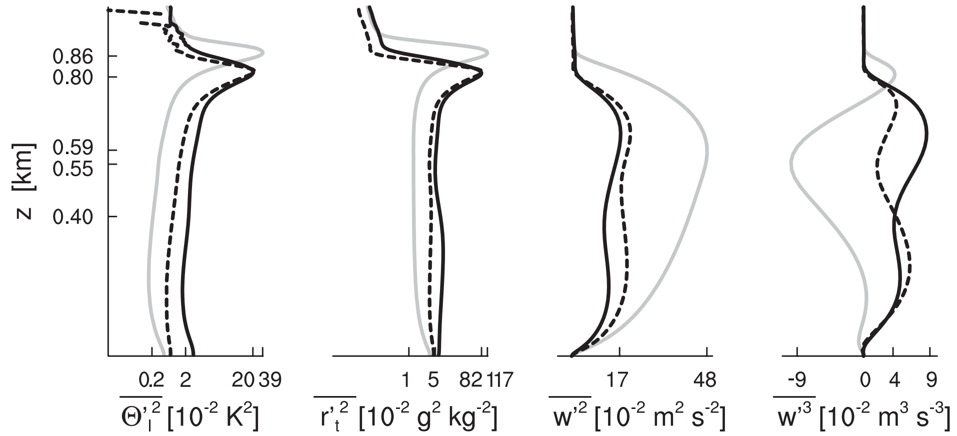

Figure 3.7: Mean profiles of variances of θ_l and r_t with logarithmic horizontal axis, and variance and third moment of w, panels from left to right, respectively, averaged over the last two hours of the simulation. Choice of lines and values on y axis are as in Fig. 3.6. Values on x axes are as follows: minimum of variance in the boundary layer and maximum of variance at the interface layer for NS and DS for θ_l and r_t; maximum of w variance in NS and DS and maximum of $\overline{w'w'w'}$ in NS and DS and minimum of $\overline{w'w'w'}$ in NS. The exception is the 0.08 value on the plot of $\overline{r_t'^2}$, which is a maximum of variance in the boundary layer of DS. From Savic-Jovcic and Stevens (2007).

velocity variance is often associated with decoupling (Stevens 2000), although only in the case when precipitation is allowed to evaporate in the sub-cloud layer is such decoupling associated with the statistical trace of cumulus clouds. The third moment of w' is positive throughout the layer in both the DS and DWES, indicative of a more surface-forced circulation irrespective of whether or not precipitation is allowed to evaporate. However, the locally increased value of $\overline{w'w'w'}$ in the cloud layer is also consistent with more cumulus-like circulations in the DS.

Variances in thermodynamic quantities are also shown in Fig. 3.7, but on a logarithmic scale. While the general trend toward more scalar variance to accompany reductions in $\overline{w'w'}$ is apparent, and larger mean-field gradients, the logarithmic scale de-emphasizes the degree to which the DS exhibits greater scalar variance, even though values of $\overline{w'w'}$ in the DS are commensurate with those in the DWES. This is yet another indicator of topological changes in the flow which emerge only when precipitation is allowed to evaporate.

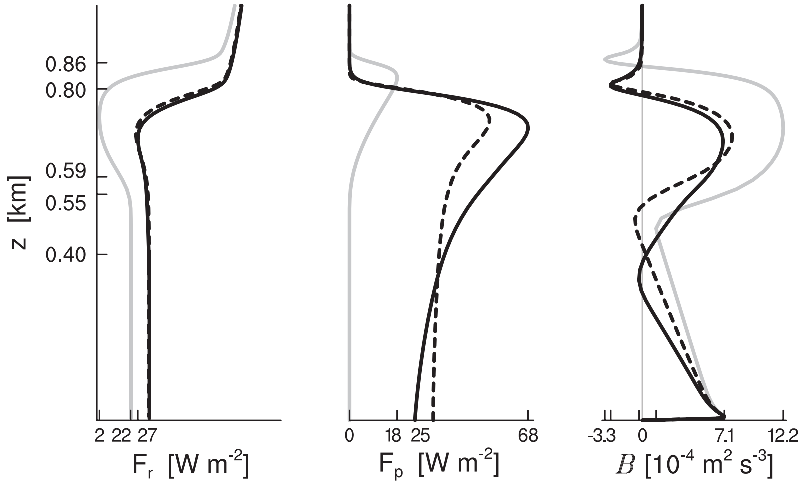

Figure 3.8: Mean profiles of radiation (left) downward precipitation (middle) and buoyancy flux (right) averaged over the last two hours of the simulation. Choice of lines and values on y axis are as in Fig. 3.6. Values on x axes are as follows: for radiation flux, minimum and surface values for NS and minimum for DS (left); for precipitation flux, maximum and surface values in NS and DS; and for buoyancy flux, maximum for NS and DS (right), zero reference line and cloud-top minimum for NS. From Savic-Jovcic and Stevens (2007).

Much of the reduction in the intensity of the circulations in the presence of drizzle can be associated with reduced buoyancy fluxes, stemming in part from less radiative driving. These changes are evident in the profiles of the radiative, precipitation and buoyancy fluxes in Fig. 3.8, where we note that the precipitation flux associated with NS is purely from the sedimentation of cloud droplets. Because the long-wave radiative flux saturates for relatively small liquid water paths, the change in the radiative forcing among the simulations is not especially strong. So it is not surprising that non-precipitating simulations with the radiative forcing reduced to match that of the DS (not shown) show this effect to be insufficient to explain the differences among the simulations. Indeed the radiative flux divergence as a whole is less than the precipitation flux divergence at cloud top, let alone the differences in the radiative flux divergences between the precipitating and non-precipitating simulations. For the most part, however, the effect of the precipitation flux does not project immediately on to the buoyancy field. Instead this forcing is manifest in raising the condensation level of the cloud top air, which acts to stabilizes downdrafts through the mechanism discussed by Stevens et al. (1998). Indeed, strong downdrafts, whether they be driven by radiation or evaporation, are not particularly evident in either the DS or the DWES at either 200 or 700 m (see *e.g.,* Figs. 3.3 and 3.4).

The evaporation of precipitation in the DS (Fig. 3.8) is significant, but relatively less than reported by vanZanten et al. (2005). In DS about 37% of the precipitation makes it to the surface compared to just under 30 % in the measurements. The evaporation of precipitation that we do see acts to stabilize the cloud layer with respect to the sub-cloud layer, and sub-cloud buoyancy fluxes are reduced. However because the evaporation of precipitation lowers the condensation level of subsequent updrafts, the buoyancy flux in the cloud layer increases. Although in our simulations these differences appear crucial, the transition to a decoupled flow can be a sharp (*e.g.,* Stevens 2000), hence it remains unclear to what extent the evaporation effect of drizzle is generally important, or just gives the simulations the extra kick necessary for them to decouple in this particular instance.

Finally, we note with the aid of Fig. 3.9 that the changes in the flow, which we have documented above, are not simply transient features, but persist over time scales that are large compared to a typical eddy turnover time of 10-20 minutes. Subsequent to the spin-up of the simulations, global features such as the net surface precipitation, the

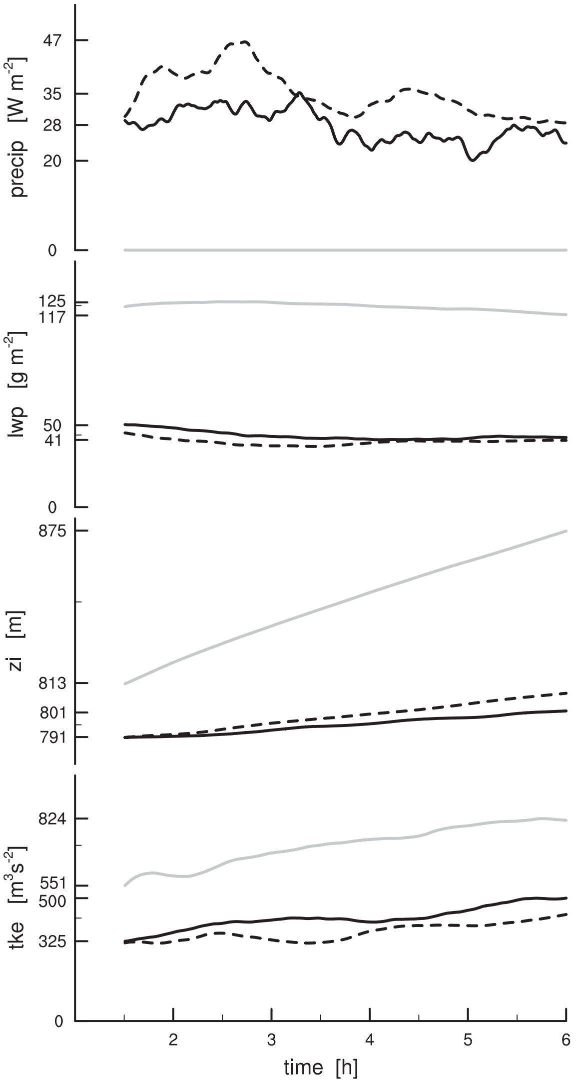

Figure 3.9: Time series of domain-averaged surface precipitation, LWP, inversion height and vertically integrated turbulence kinetic energy, panels from top to bottom respectively. Line description as in Fig. 3.2. Values on y axes are as follows: minimum and maximum of time series of precipitation in all three simulations (top panel); and minimum and maximum of corresponding time series for NS and DS (lower three panels). Unlabeled tick marks on lower three panels represent the mean values of the corresponding time series for NS and DS. From Savic-Jovcic and Stevens (2007).

cloud liquid water path, and the growth rate of the layer and of the domain-averaged turbulence kinetic energy (TKE) are remarkably constant. Clearly precipitation, while depleting the cloud layer of liquid water, does not lead to a collapse or more rapid demise of the cloud layer. The ability of the circulations to sustain a long-lived, persistently precipitating layer is consistent with observations by vanZanten et al. (2005) and Comstock et al. (2005), although it had been called into question by some earlier studies, and a somewhat lazy terminology that too often associates precipitation duration with cloud lifetimes. The time series of PBL depth (third panel in Fig. 3.9) also shows that the tendency of the precipitating layers to deepen less rapidly, as was evident in earlier work of Stevens et al. (1998), represents a systematic influence of weaker entrainment rates, rather than a sudden adjustment to the development of precipitation. Interestingly, there is a slight tendency of the DS to deepen less rapidly than the DWES, despite slightly increased values of TKE. We speculate that this is due to a greater fraction of the TKE being carried by the variances in the horizontal wind in the DS, as the values of $\overline{w'w'}$ are smaller in the DS than in the DWES, which is consistent with slightly weaker entrainment rates.

3.2. Pools of elevated equivalent potential temperature

VanZanten et al. (2005) noted that pools of elevated θ_e were associated with precipitating regions in their analysis of *in situ* observations of precipitating stratocumulus. Similar features are prominent in the DS. For instance, as illustrated by Fig. 3.10, areas of precipitation tend to be collocated with the areas of elevated θ_e, most strikingly in the sub-cloud layer, where they are observed, but also through the depth of the PBL. Figure 3.11 attempts to quantify this association by plotting θ_e averaged over those points whose precipitation rate exceeds some threshold, versus this threshold. Averaged over all precipitating regions, θ_e is up to 0.1 K warmer than the domain-average, with the degree of the mean θ_e anomaly increasing with precipitation amount. Averaging just over regions of showers (*i.e.*, where precipitation rates exceed 1 cm day^{-1}), θ_e anomalies approach 0.5 K. However, because to a first approximation θ_e is conserved under precipitation, it seems natural to ask (as did vanZanten et al. 2005) what leads to the elevated regions of θ_e.

This question is even more puzzling as the virtual potential temperature, θ_v, a perturbation of which is a proxy of buoyancy, behaves as expected – in the presence of precipitation it has lower values, because the evaporation of drizzle acts as a sink of buoyancy. As illustrated by Fig. 3.11, composites for θ_v indeed exhibit negative anomalies (cold pools) in the precipitating areas. Similar behavior was also observed by Paluch and Lenschow (1991), who in the presence of drizzle estimated negative correlation between temperature and moisture on the mesoscales.

The simulations help us address the question of the source of the elevated θ_e in the precipitating regions. Because precipitation tends to stabilize the flow and hence reduce the vertical mixing and subsequent homogenization of the STBL, there is a general tendency of the precipitating simulations to have larger vertical gradients in thermodynamic quantities (particularly for moisture, *e.g.,* Fig. 3.6). In Fig. 3.5, this tendency is manifest in the concentration of large values of θ_e near the surface. This suggests that regions of anomalously high θ_e might be a tracer of mesoscale circulations that channel near-surface air, which is rich in θ_e, into the interior of the flow. Figure 3.5 supports this line of thought as the precipitating regions, which collocate with regions of elevated θ_e, are also the regions where updrafts concentrate, presumably in the form of cumulus clouds.

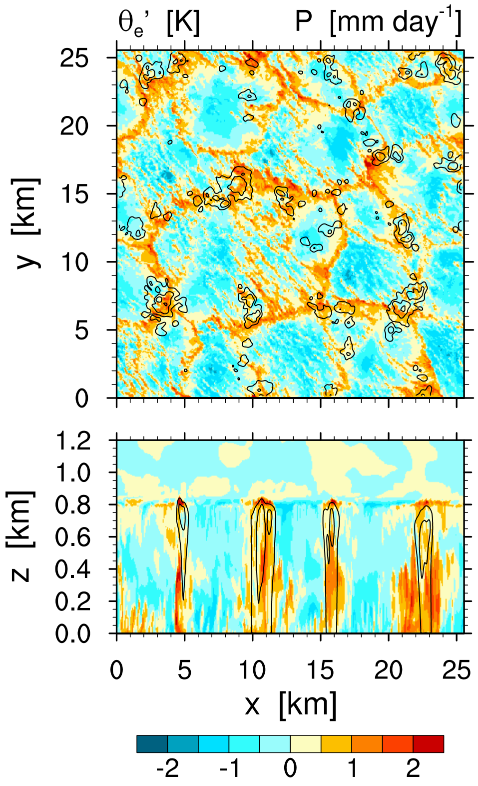

Figure 3.10: Top panel: Instantaneous fields of perturbation of θ_e from horizontal mean and smoothed precipitation at 90 m height level at the end of the 6^{th} h of DS simulation. Bottom panel: Vertical cross section at $y = 45$ m of the instantaneous θ_e perturbations from the horizontal averages, and horizontally smoothed precipitation at the end of the 6^{th} h of the DS simulation. Precipitation contours have values of 2, 10 and 30 mm day^{-1}. From Savic-Jovcic and Stevens (2007).

a. *Conditional Sampling*

To explore these ideas further, we form conditional averages of θ_e and w over the strongest θ_e events in the NS and the DS, which we refer to as θ_e cells. The conditional averaging follows the approach outlined by Schmidt and Schumann (1989), with details provided in Section 2.5. The flow, conditionally averaged in this way (Fig. 3.12), provides support for these ideas. Not only does it show anomalous stratification of θ_e

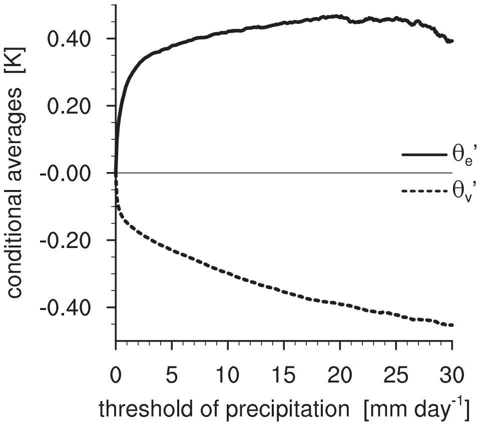

Figure 3.11: Conditional average of θ'_e and θ'_v based on the strength of precipitation at 90 m height level at the end of the 6^{th} h of DS simulation. From Savic-Jovcic and Stevens (2007).

in the DS simulations, but also an association of θ_e cells with both precipitation and updrafts. The latter are key in transporting air rich in θ_e away from the surface.

For the precipitating simulations, these questions are also usefully explored by examining the structure of the flow conditionally averaged on drizzle (Fig. 3.13), or what we call drizzling cells. Conditionally sampling in this way confirms the previous association of drizzling areas in the DS with the pools of elevated θ_e. It also reveals subtle differences between θ_e and drizzling cells. Peak values of θ_e tend to be just off the center of the drizzling cell, which suggests that the precipitation maximizes on the edge of θ_e cells. This agrees well with the tilted position of the updrafts in the drizzling cells of the DS, also evident in Fig. 3.13 – one interpretation of this is that new cumulus cells form on the outflow boundaries of evaporating precipitation (*i.e.*, the θ_e-rich cold pools), and that they are accompanied by mid-level inflow (*e.g.,* Comstock et al. 2007).

Figure 3.13 also helps illustrate the effect of evaporation of drizzle on the flow.

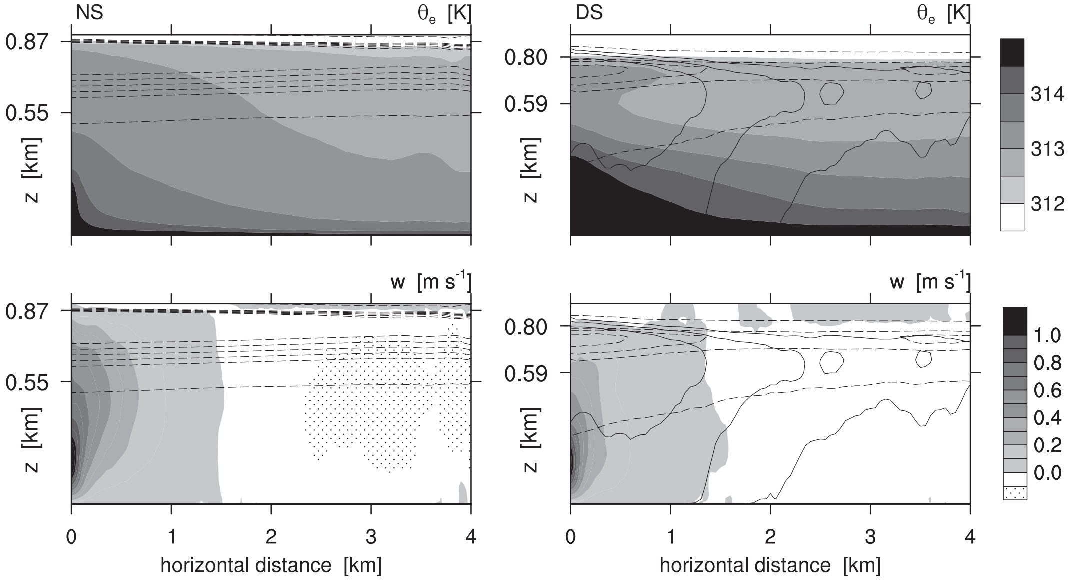

Figure 3.12: Conditional composites of θ_e, w, r_l and precipitation over the 40 strongest θ_e cells averaged over 3 independent times. Dashed contours represent r_l and have values of 0.01, 0.2, 0.25, 0.3, 0.35 and 0.4 g kg^{-1}. Solid contours represent precipitation intensities of 0.5, 1, 2, 5 and 10 W m^{-2}. Values on y axes are as in Fig. 3.6. Left column is NS and right column is DS. From Savic-Jovcic and Stevens (2007).

Whereas evaporation leads to the development of a pronounced downdraft at the base of the drizzling cell (the evaporating rain-shaft), such a feature is absent in the DWES. As a result, the updraft, and the associated region of precipitation, tends to be more spatially diffuse in the DWES, perhaps reflecting the lack of outflow boundaries in the absence of evaporation of precipitation. The suggestion that the coupling between the cloud and sub-cloud layer is more spatially compact in the DS simulations is consistent with the emergence of a mushroom- (or anvil-) like character of the cloud layer θ_e field in the DS drizzling cells, and the lack of such a feature in the drizzling cells of the DWES. It is also consistent with simulations of trade-wind cumulus (Xue et al. 2007) and some previous observational analyses of shallow convection (Jensen et al. 2000),

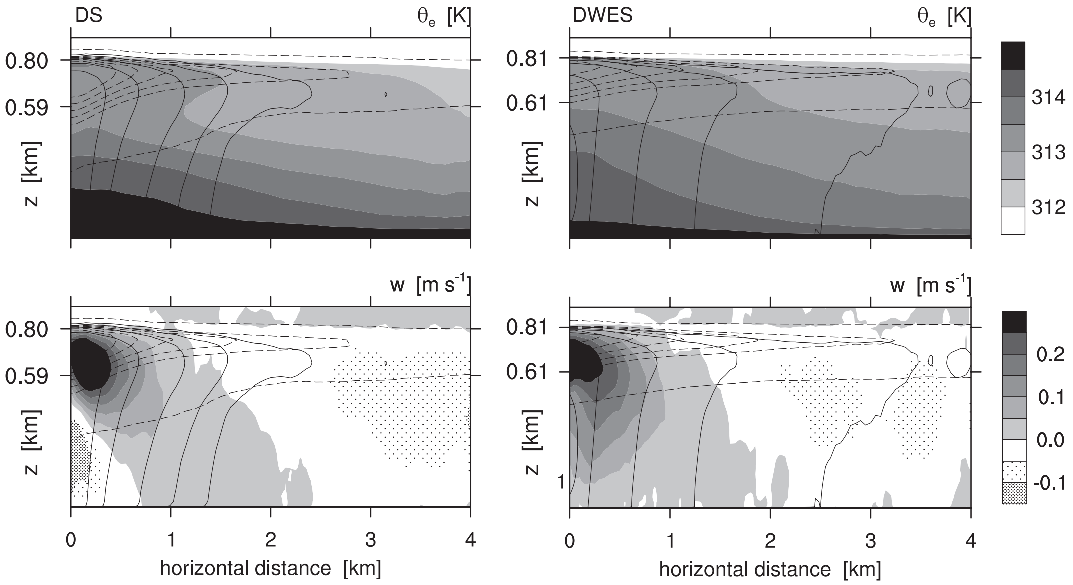

Figure 3.13: As in Fig. 3.12, but for the drizzling cells. Left column is DS and right column is DWES. From Savic-Jovcic and Stevens (2007).

which show that precipitation helps control the organization of new cloud formation, largely confining it to boundaries marking the edge of outflow from the precipitating downdrafts.

b. *Conceptual diagram*

In Fig. 3.14, we summarize some of the insights of the previous analysis in the form of a conceptual diagram, or a cartoon. In particular, we illustrate the tendency of strong drizzle (in our simulations about 1 mm day^{-1}) to drive a transition from a well-mixed stratocumulus-topped boundary layer driven by radiation and downdrafts to a more cumulus-coupled, or cumulus-under-stratocumulus-topped layer. Our ability to quantify how different processes contribute to such a transition are the subject of an ongoing study. Here, the drizzling regime is described, as well as how it differs from the non-drizzling one.

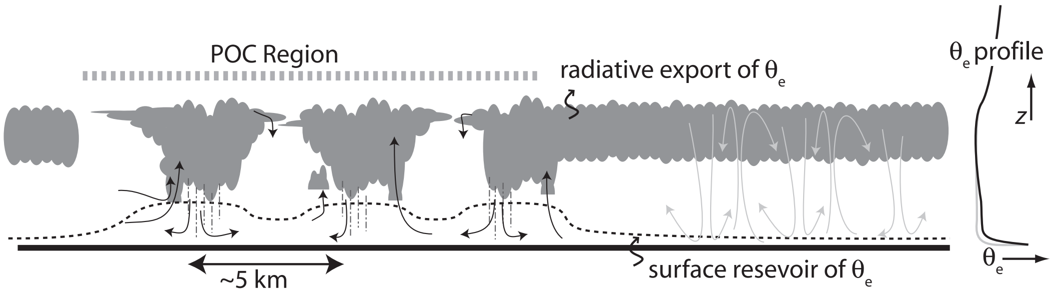

Figure 3.14: Generalization of cartoon from vanZanten et al. (2005) conceptualizing the circulation and its effects on cloud and θ_e. Here the behavior in non-precipitating stratocumulus (including mean profiles of θ_e) is shown in gray alongside precipitating regions (darkened). From Savic-Jovcic and Stevens (2007).

The cartoon depicts that, in agreement with the observations (vanZanten et al. 2005; Comstock et al. 2005), precipitation tends to be located in patches, where the cloud base is lower and motions are carried by more cumulus-like circulations. In these regions, θ_e is higher and updrafts are more vigorous. Away from these regions, the circulations are weaker and may even be cloud free in places. There is also less evidence of downdrafts that mix through the depth of the layer, such as are characteristic of the non-precipitating STBL.

The changes in the turbulent structure of the flow that accompany drizzle allow for greater differentiation in conserved tracers. Specifically, reduced mixing throughout the boundary layer allows θ_e to accumulate near the source of θ_e at the surface. This vertical differentiation can lead to horizontal differentiation in the presence of coherent updrafts. For instance, the updrafts in the drizzling regime draw on a richer reservoir of θ_e as compared to the updrafts in the non-drizzling one. The tendency of updrafts to be more localized (cumulus like) in the presence of precipitation amplifies the contrast in θ_e between updraft regions and the environment above the surface layer. Finally, because updrafts tend to be concentrated in, or at the boundary of the precipitation shafts, regions of elevated θ_e appear collocated (or near so) with regions of precipitation. This may provide an explanation of why the pools of elevated θ_e became detectable by aircraft measurements in the drizzling parts of RF02 of DYCOMS-II (vanZanten et al. 2005).

To the extent our simulations are correct, the highest values of θ_e will not be found directly in the precipitation shafts; rather, on the sides where air is being most actively drawn out of the surface layer. It is still unclear if these θ_e-rich updrafts are the source of new cells, or if they simply reflect a circulation that supports already existing drizzling cells with the necessary θ_e. Both of these might explain the long-lasting steady precipitation over the domain as a whole, and are a subject of our further investigation.

3.3. Discussion

a. *Scales of Variance*

To what extent does precipitation engender, or promote, the development of meso-γ scale variance in the simulations? From Fig. 3.1 it is clear that variance develops at larger scales in all the simulations, irrespective of the development of drizzle. This tendency toward the development of larger-scales in all quantities other than w is evident in the steady increase in boundary layer integrated turbulence kinetic energy (lower panel of Fig. 3.9). The increase in TKE is due to increases in the horizontal velocity variances, and spectra show these to be increasing with time at the largest scales. Visualizations of the evolution of albedo show a similar trend, and are reminiscent of the results of de Roode et al. (2004), which suggests that the underlying conditions for the emergence of large-scales is the same as that reported by Jonker et al. (1999), and not dependent on the development of precipitation. Such a result would also be consistent with the observations of Wood and Hartmann (2006) who find no systematic difference between the aspect ratios of open and closed cells.

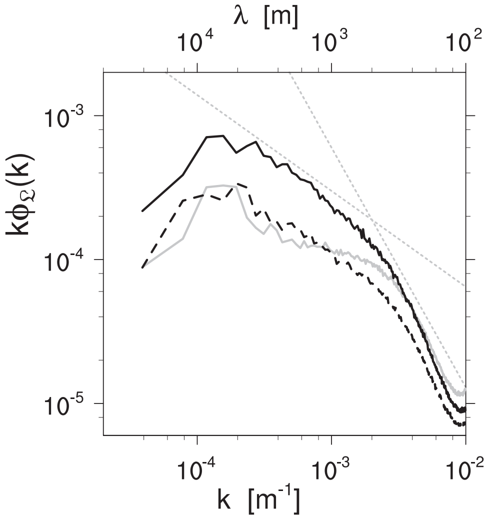

Figure 3.15: Power spectra of the liquid-water path in the simulations. Choice of lines follows Fig. 3.2. Dotted lines shows a -2/3 and -5/3 spectra respectively. From Savic-Jovcic and Stevens (2007).

Precipitation, does however seem to enhance the accumulation of large-scale variance in our simulations. This is evident in Fig. 3.15 which shows the power spectrum of liquid-water path from the simulations. Although the variance at the small scales is probably too damped, for reasons discussed above, these spectra show that all the simulations develop significant variance at large scales, but that this accumulation is most pronounced for the DS. This increase in variance at large-scales is also evident in the spectra of θ_l and r_t, particularly near the top of the boundary layer, and may reflect a less active cascade of variance to small scales in association with a weaker boundary

Simulation	NS		DS	
Size	6.4 km	25.6 km	6.4 km	25.6 km
A [%]	69.9	73.0	28.1	34.5
$\mathcal{L}$ [gm^{-2}]	103.9	122.1	38.3	50.4
$\mathcal{C}$ [%]	99.9	100.0	88.7	95.4

Table 3.1: Domain averaged albedo, liquid water path and cloud fraction for both small and large domain simulations over the last two hours of the simulation. From Savic-Jovcic and Stevens (2007).

layer circulations, or simply the effect of precipitation which acts as a source of θ_l and r_t and may thereby amplify any preexisting tendency toward the development of larger scales.

How important is the emergence of larger-scale variance to the mean properties of the simulations? Here we rejoin the question raised in the introduction, regarding the reliability of simulations of these phenomena on much smaller domains. To address this question Table 3.1 presents statistics from both large and small domain simulations. Overall the small domain simulations seem to be biased toward lower amounts of cloud, cloud liquid water and smaller albedo. The effects are more pronounced in the presence of precipitation, hence the simulations on the small domain exaggerate the effects of precipitation. One interpretation is that the compensating subsidence associated with the emergence of more cumulus like cells is confined to too small a scale. Another possibility is that the growth of variance at larger scales favors the development of cloud. Notwithstanding these limitations, the small domain simulations do capture the main features of the simulations at larger scales, and the biases one can attribute to under-representing the range of scales are probably no greater than those associated with uncertainties in the representation of microphysical processes.

b. *Consummating the transition*

The simulations show that precipitation can lead to a marked transition in the planform structure of the cloud, and that this transition evinces elements of a more open cell, or POC-like structure. That said, even by forcing drizzle with rather dramatic reductions in droplet concentrations it is fair to say that the open-cell regime we see in satellite images of pockets of open cells are not fully realized by the simulations. Are we missing something? One possibility is that the microphysical representation, either by producing too large of precipitation particles or through our neglect of ventilation effects or other processes, leads to insufficient evaporation in the sub-cloud layer. Or that our use of a more active microphysical scheme (*i.e.,* Seifert and Beheng 2001, as compared to Khairoutdinov and Kogan 2000), and perhaps unrealistically low droplet concentrations still underestimates the drizzle rate. Locally, vanZanten et al. (2005) find evidence for more intense precipitation than we measure, and more active evaporation. But because their data only partially sampled the region of open cells, it proves difficult to make such comparisons more quantitative. Even so, as a preliminary exploration of these ideas, we conducted a series of simulations in which we enhanced the evaporative effects of precipitation, but these did not produce a more marked open-cellular structure (left panel in Fig. 3.16).

Another possibility is that other processes play an important role. For instance the diurnal cycle. During the daytime hours the additional desiccation of the thin layer of clouds, due to solar radiative effects compensating the long-wave cooling, may provide an additional forcing that helps consummate the transition to an open cellular structure. We do indeed find that if the DS is extended for an additional three hours without any radiative forcing (as a first approximation to the cancellation of long-wave

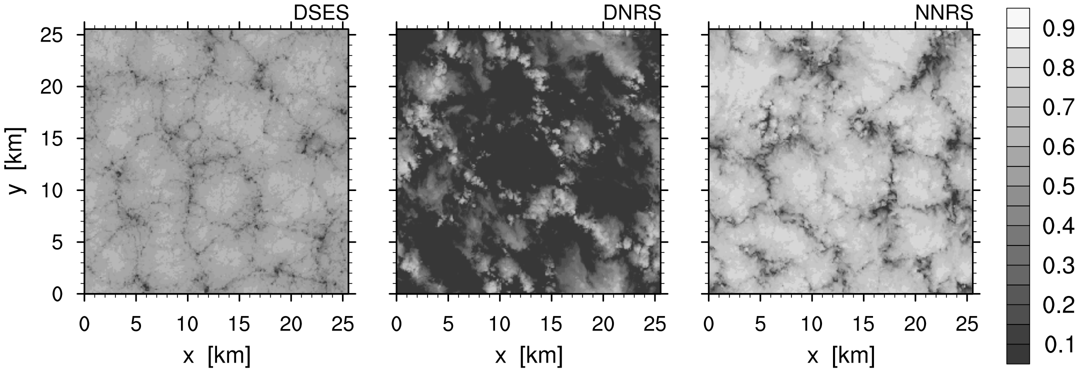

Figure 3.16: Albedo, as per Eq. (3.1), at the end of the following simulations: DDES - drizzling simulation with doubled intensity of drizzle evaporation in the subcloud layer, DNRS - three additional hours of simulation for the case of DS, but with the radiative forcing turned off, and NNRS - as DNRS, but for the NS case. Following Savic-Jovcic and Stevens (2007).

cooling by shortwave heating), the transition to a more completely open-cell structure is unambiguous (DNRS, middle panel in Fig. 3.16). Similar transitions however do not occur in simulations of this type performed using the NS as initial conditions (right panel in Fig. 3.16). Here note that the cloud field in the DNRS is relatively steady, and that apart from the changes in the cloud field, and the emergence of even larger scales, the principal difference with the DS is that in the absence of long-wave cooling the cloud-layer warms substantially. One objection to this line of argument could be that pockets of open cells are also evident in the night-time imagery (Petters et al. 2006), but perhaps this simply reflects the inability of the closed-cell pattern to re-establish itself after daytime desiccation. While these ideas are speculative, they can be tested; for instance, by looking to see whether the satellite record shows POCs more likely to form during the day or night, or by simulations which more realistically and systematically treat the effects of the diurnal cycle.

3.4. Summary and conclusions

In this Chapter we analyze the large-eddy simulations of precipitating stratocumulus in large domains (25.6 km by 25.6 km), that involve a simple, bulk, two-moment representation of microphysics. The use of such a simple scheme allows us to explore the interaction of microphysical, turbulent cloud dynamical, and radiative processes over large spatial scales using fine spatial discretization. These simulations are shown to realistically represent many aspects of observed precipitating stratocumulus, which include the tendency of the layer to transition to more cumulus-coupled circulations, with locally elevated cloud tops and patches of anomalous sub-cloud equivalent potential temperature, θ_e, in the vicinity of precipitating clouds.

The simulations also capture the observed tendency for precipitation to be associated with the emergence of a more marked mesoscale circulation and a general reduction in cloudiness. Comparisons between precipitating and non-precipitating simulations show a reduction in cloud albedo from near 75% in the absence of precipitation to values less than 35% in the presence of domain-averaged precipitation rates of around 1 mm day^{-1}. Most of this albedo reduction can be attributed to changes in the character of the circulation, as the reduction due to the Twomey effect can only account for about a third of the simulated albedo change. Although domain-averaged liquid water paths are reduced by half in the presence of drizzle, our simulations are able to maintain a nearly stationary evolution of the cloud in the presence of significant precipitation, in part because the stabilizing effect of precipitation reduces cloud top entrainment, and hence entrainment drying. The stabilizing effect of precipitation is also evident in a reduction in vertical mixing, greater differentiation between the cloud and sub-cloud layer, and a marked increase in the variance of thermodynamic variables. The results provide support for inferences made from coarser resolution simulations with horizontal domains too small to represent mesoscale flow features. Analyses of the simulations suggest that the observed tendency of precipitation from shallow convection to collocate with patches of elevated values of sub-cloud equivalent potential temperature reflects the tendency of θ_e to accumulate near the surface in more stabilized, precipitating flows, in concert with mesoscale circulations which concentrate precipitation within envelopes of upward motion.

A sensitivity study, in which the evaporation of precipitation-size drops is suppressed, shows that for this case, the evaporation of precipitation is critical to the observed flow transition. While precipitation rates and liquid water paths are commensurate between precipitating simulations with, and without, evaporation, the transition of the flow to a cumulus-coupled state is only evident in the case when precipitation-size drops are allowed to evaporate below cloud base. Moreover, the sub-cloud circulations (cold pools and ensuing regions of lower cloud base) that ensue from such a process appear to play a vital role in shaping the structure of both the sub-cloud layer and regions of new convection.

Chapter 4

Dynamics of the Drizzling STBL

It is demonstrated in Chapter 3 that drizzle can lead to changes in the structure and flow of the STBL, and consequently in the topology of Sc. Because of the importance of Sc for the Earth's climate system, it is of interest to understand how these changes occur and how they affect our traditional view of the STBL. To systematize these issues, this Chapter is devoted to analysis of the contributions of drizzle to the dynamics of the STBL by investigating the effect of drizzle on the energetics of the flow, as well as by exploring the impact of drizzle on the θ_l and r_t budgets. In particular, in section 4.1, we revisit the Mixed-layer model (MLM) and utilize it to discuss the energetics of the drizzling flow. In section 4.2, we show that the mean drizzle-induced forcing can account for the changes in the strength of circulation but but not for the topological changes. We follow this analysis with an isolation of the effects on the temperature and moisture budgets in section 4.3 and with a summary in section 4.4.

4.1. Drizzle in the Mixed-layer Framework

A prominent feature of drizzle that is observed (*e.g.*, vanZanten and Stevens 2005; Comstock et al. 2004) and captured in the LES (Chapter 3) is drizzle's localized nature. However, the theoretical framework for understanding the non-precipitating STBL (the Mixed-layer Model, MLM, framework) and the STBL parameterizations in GCMs (General Circulation Models) neglect any internal variability within the STBL. This discrepancy raises the question of whether there is a place for interpretation of drizzle in this canonical view of the STBL. Furthermore, LESs of drizzling STBL show slight differentiation between the cloud and subcloud layers (*e.g.*, Stevens et al. 1998, and the previous Chapter). How can this differentiation be reconciled with the basic assumption of the MLM that the STL is vertically well-mixed? A recent review of bulk representation of tropical and subtropical maritime atmospheric boundary layers by Stevens (2006) offers a more general view on the equations that describe the MLM and does not rely on the vertically well-mixed state of the boundary layer. This interpretation prompts us to ask to what extent can drizzle effect be included in the traditional MLM framework. Seeking an answer, we analyze the simulations discussed in the previous Chapter in terms of the MLM. In particular, in section 4.1.a we review the MLM with its bulk generalization, then, in section 4.1.b we review the energetics in the MLM framework. In section 4.1.c, we discuss the direct effect of domain-mean representation of drizzle onto the energetics of the STBL, neglecting all other interactions.

a. *Mixed-layer Model*

In mathematical terms, the mixed-layer model (Lilly 1968) describes the state of the well-mixed, non-precipitating, nocturnal STBL simply through the equations for budgets of mass, heat and moisture (represented by the height of the layer (h) and the boundary-layer values of θ_l and r_t, which we denote by a hat), or the evolution equations:

$$\frac{dh}{dt} = W + E \tag{4.1}$$

$$\frac{d\hat{\theta}_l}{dt} = \frac{1}{h}[V(\theta_{l,0} - \hat{\theta}_l) + E(\theta_{l,+} - \hat{\theta}_l) - \Delta F_{\theta_l}] \tag{4.2}$$

$$\frac{d\hat{r}_t}{dt} = \frac{1}{h}[V(r_{t,0} - \hat{r}_t) + E(r_{t,+} - \hat{r}_t) - \Delta F_{r_t}]. \tag{4.3}$$

Here: $W = -Dh$ is the large-scale subsidence at the top of the layer, where D is the large-scale divergence, which is assumed to be independent of height within the boundary layer; E is the entrainment rate, which is used to parameterize the entrainment fluxes; V is the surface exchange velocity, which parameterizes the surface fluxes; the subscripts $+$ and 0 denote the values just above the inversion layer and surface values; ΔF_{θ_l} and ΔF_{r_t} are the total diabatic flux divergences across the layer depth and are related to the radiation and drizzle. In these equations, all the parameters, except perhaps E, can be expressed with confidence in terms of the "hat" quantities. For instance, ΔF_{θ_l} and ΔF_{r_t} can be related to the cloud depth through the liquid water path, which is straightforward to determine in the MLM because the cloud top coincides with the top of the STBL and the cloud base is at the height where $r_t = r_s$ and $r_l = 0$, with r_s being the saturation water vapor mixing ratio that depends on the temperature and pressure. This simplicity in forcings definition is one of the main advantages of the MLM, making it a simple tool for studying the evolution of the STBL under various conditions.

Stevens (2006) derives the same set of equations, but with a different meaning of the “hat” variables. In Stevens (2006) interpretation, these are bulk values, or vertical averages of the ensemble-averages, which does not require the previously assumed well-mixed state of the layer. This approach, moreover, is not limited to the horizontally uniform state, but allows for the analysis to be in terms of mean states that are implicitly affected by the internal variability. Along with the different meanings of the “hat” variables, some of the terms in Eqs. (4.1)-(4.3) have different interpretations too. For instance, height h is the height just above the boundary layer top, so that there are no turbulent fluxes at that height, which then allows for the entrainment flux to be defined as it is in Eqs. (4.2) and (4.3). Similarly, because the state variables are not required to be well mixed, it is their profiles that define the cloud amount and therefore the diabatic fluxes. Stevens (2006) also recognized that the common assumption of $W \approx Dh$ does not require horizontal wind divergence to be independent of height through the layer, but that it stems from the wind jumps across the top of the boundary layer being small. In addition to all the generalizations, there are a few assumptions in the derivations of Stevens (2006) – turbulent fluxes of the thermodynamic variables are horizontally homogeneous and baroclinic circulations within the boundary layer have negligible contributions to the evolution of the bulk properties. With these generalizations and assumptions in mind, Eqs. (4.1)-(4.3) could provide a useful diagnostic tool for the flow simulated with the LES regardless of the vertical structure and horizontal uniformity within the domain, which we utilize in our analysis of the drizzling STBL.

Because the bulk approach of Stevens (2006) could be applied in the diagnosis of the drizzling STBL, we utilize it in the analysis of our simulations from the previous

Chapter. In particular, we investigate the consistency of the energetics of a mixed layer that drizzles as much as the drizzling simulation (DS) from the previous Chapter, but otherwise evolves identically to the non-drizzling simulation (NS). In the analysis, we first diagnose the state of the NS using Eqs. (4.1)-(4.3) and then impose drizzle from the DS on it to study the dynamical response of such a system. Specifically, we diagnose entrainment and the cloud-base height for the NS and apply them when calculating buoyancy fluxes discussed in the following sections.

A unique value for entrainment in the NS in our analysis is estimated as an average of the values determined from the three budgets in Eqs. (4.1)-(4.3). To calculate the individual values, we first determine all the other terms in the budgets equations. In particular, starting from the domain-mean profiles recorded every 15 min, we determine the time series of heights of the boundary layer (h) as the heights where the turbulent fluxes of thermodynamic variables are negligible (about 1%) compared to their boundary-layer values. This time series of heights allows us to define the time series of the bulk θ_l and r_t, by integrating their vertical profiles:

$$\hat{\theta}_l(t) = \frac{1}{h(t)} \int_0^{h(t)} \bar{\theta}_l(t, z) dz \tag{4.4}$$

for $\hat{\theta}_l$ and similarly for $\hat{r}_t$. Having all three time series, we determine the evolution of each variable by finding a slope of the best fitting line. Differences of the state variables just above the top of the boundary layer and their bulk values are also easy to determine from these time series. Divergence of radiative flux across the boundary layer is determined as a difference between the values at a height just above the boundary-layer top and the surface value. In addition, from the set up for the LES experiments, we know surface fluxes of sensible and latent heat, as well as divergence (16 W m^{-2}, 96 W m^{-2} and 3.75$\times$10^{-6} s^{-1}, respectively), which are the additional

	mass budget	heat budget	moisture budget	mean
entrainment [10^{-3} m s^{-1}]	7.0	6.9	6.8	6.9

Table 4.1: Entrainment estimates from the three budgets in the NS, and their mean.

variables necessary to determine entrainment from each of the budgets separately. Table 4.1 summarizes these values, as well as the mean entrainment, which we apply when calculating the buoyancy fluxes discussed in the following section.

b. *Energetics*

Because the main source of turbulence in the convective boundary layers is the buoyancy flux, understanding the behavior of the buoyancy fluxes in the STBL could provide a basis for exploring the effect of drizzle on the STBL energetics. Furthermore, because the buoyancy is determined by the state variables ($b \approx \theta_v' \,/\, \theta_0 \approx \alpha\, \theta_l' \,/\, \theta_0 + \beta\, r_t$), turbulent fluxes of the state variables yield to the turbulent buoyancy flux, $\mathcal{B}$. This more or less straightforward relationship is, however, affected by the saturation state of the boundary-layer air. In the moist unsaturated air, the thermal effect on buoyancy is more important than the moisture effect, whereas in the saturated air, moisture becomes more important due to the release of latent heat by the phase change. In the expression for $\mathcal{B}$:

$$\mathcal{B} = \overline{w'b'} = g \begin{cases} \alpha_u(\overline{w'\theta_l'}/\theta_0) + \beta_u\overline{w'r_t'} & r_t < r_s, \\ \alpha_s(\overline{w'\theta_l'}/\theta_0) + \beta_s\overline{w'r_t'} & r_t \geq r_s, \end{cases} \tag{4.5}$$

these effects are isolated in the partial derivatives α_u, α_s, β_u, and β_s (where g is the gravitational acceleration, θ_0 is the reference potential temperature, $\alpha = \frac{\partial\theta_v}{\partial\theta_l}$ and $\beta = \frac{1}{\theta_0}\frac{\partial\theta_v}{\partial r_t}$). These derivatives are functions of state and can be determined analytically. Moreover, for shallow flows, they can be approximated to be constant (Stevens 2004), and for the conditions of the simulations from the previous Chapter, namely $\theta_l = 289$ K and $r_t = 9$ g kg^{-1}, they have the following values: $\alpha_u = 1.005$, $\alpha_s = 0.52$, $\beta_u = 0.607$ and $\beta_s = 3.48$. As the values of partial derivatives show, the thermal effect on buoyancy in the cloud is reduced to almost half of its subcloud value, whereas the moisture effect is increased by almost an order of magnitude. However, because of this dependency of the buoyancy fluxes on the saturation state of the flow, one has to be careful when interpreting the results, as the Eq. (4.5) assumes horizontal uniformity of saturation.

In further analysis, we exploit the STBL characteristic of being in a *quasi-steady* state, which describes a time invariability of profiles of conserved variables (*e.g.*, for case of θ_l: $\partial_t \partial_z \overline{\theta_l} = 0$). The quasi-steady state of the STBL stems from the persistence of the well-mixed state of the STBL when the time scale of the forcings' variability is long compared to the turnover time scale within the STBL, not from the well-mixed state itself. For a horizontally homogeneous flow ($\partial_t \overline{\theta_l} = \partial_z (\overline{w'\theta_l'} + F_{\theta_l})$), the quasi-steady state implies a linear profile of the sum of diabatic and turbulent fluxes of conserved quantities ($\partial_z \partial_z (\overline{w'\theta_l'} + F_{\theta_l}) = 0$). Therefore, in the MLM, given a knowledge of the diabatic forcings, F, and turbulent fluxes at the flow boundaries, quasi-stationarity determines the profiles of the total fluxes of θ_l and r_t ($\mathcal{F}_{\theta_l} = \overline{w'\theta_l'} + F_{\theta_l}$ and $\mathcal{F}_{r_t} = \overline{w'r_t'} + F_{r_t}$) as straight lines, with the slopes corresponding to the rates of warming/moistening. Moreover, one can determine turbulent fluxes of θ_l and r_t as the residuals from the total and diabatic fluxes. These turbulent fluxes can then be subjected to Eq. (4.5) to provide the buoyancy flux profile. In our analysis of the drizzle effect on the energetics of the STBL, we follow this approach to calculating the buoyancy fluxes.

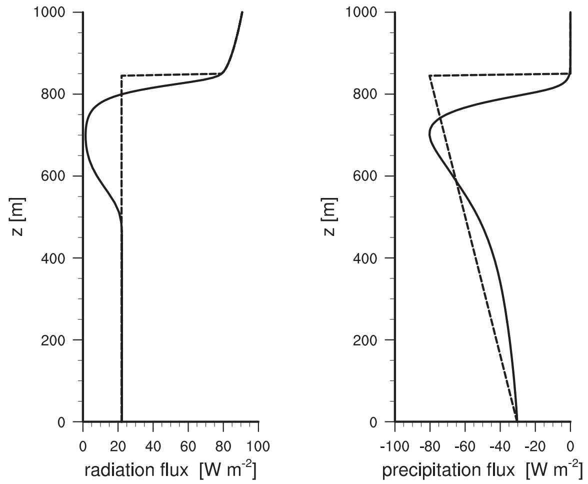

Figure 4.1: Fluxes of radiation from the NS (left) and precipitation from the DS (right). Lines: solid - from the simulation, dashed - projected onto the boundaries.

To summarize our analysis of the energetics, we estimate the entrainment in the NS to be consistent between the three budgets (Eqs. (4.1)-(4.3)) and use that value to determine the rates of heating and moistening, which we further apply to diagnose the turbulent fluxes and energetic consistency of the NS. Initially, instead of using the realistic profiles of forcings, we project them onto the boundaries (the boundary-layer top and surface), which is a common approach due to its simplicity. Figure 4.1 illustrates the radiative flux from the NS and its projection described here, as well as the precipitation flux that will be addressed in section 4.1.c

Figure 4.2 illustrates the turbulent fluxes of θ_l and r_t (in buoyancy flux units), as well as the resulting buoyancy flux for the bulk layer that evolves identically to the NS and has its radiative flux forcing projected to the top boundary. As expected for the non-drizzling, nocturnal, radiatively-driven STBL, most of the buoyancy flux profile is positive. The slight negative values atop the subcloud layer can be interpreted as a

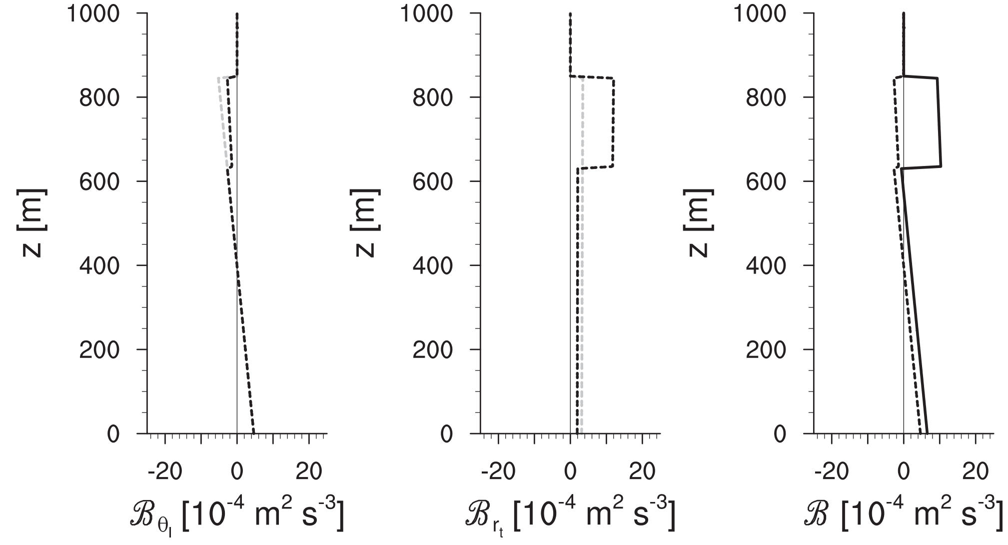

Figure 4.2: Turbulent buoyancy fluxes for the NS with radiative forcing projected to the boundaries. Colors: gray - turbulent fluxes of θ_l and r_t, black - buoyancy fluxes. Lines: solid - buoyancy flux, dashed - portion of buoyancy flux due to turbulent fluxes of either θ_l, or r_t.

consequence of strong entrainment when compared to the radiative forcing. They are also indicative of the need for turbulence to do work to mix the air from the cloud layer downwards and the air from the subcloud layer upwards into the cloud. As discussed by Turton and Nicholls (1987) and Bretherton and Wyant (1997), this could eventually lead to decoupling. However, these negative values are small and span a shallow layer so that their effect can overall be considered insignificant. To be more quantitative, we calculate a buoyancy integral ratio defined by Bretherton and Wyant (1997) as the negative ratio of the integral of negative buoyancy fluxes over the integral of positive buoyancy fluxes:

$$BIR = -\frac{\int_0^{z_i} \mathcal{B}_-}{\int_0^{z_i} \mathcal{B}_+},$$

where $\mathcal{B}_-$ are all the negative values and $\mathcal{B}_+$ are all positive values of buoyancy flux. Stevens (2000), who analyzed the amount of work that turbulence can do to sustain a well-mixed state (*i.e.*, upper limit of BIR that would allow for the MLM application), suggests that if the BIR exceeds 10%, the boundary layer is decoupled and the MLM would be ill defined. For the NS with projected radiative forcing, the BIR has a value of only 0.4%, which is small enough so that this condition for decoupling is not satisfied. This buoyancy profile is in agreement with our analysis of the NS in Chapter 3, where we presented a well-mixed boundary layer. In addition to that agreement, this buoyancy profile shows that the NS is near the threshold between a well-mixed and decoupled STBL. Slight nudges to the system could move it toward the decoupled state. Is drizzle from the DS a strong enough nudge?

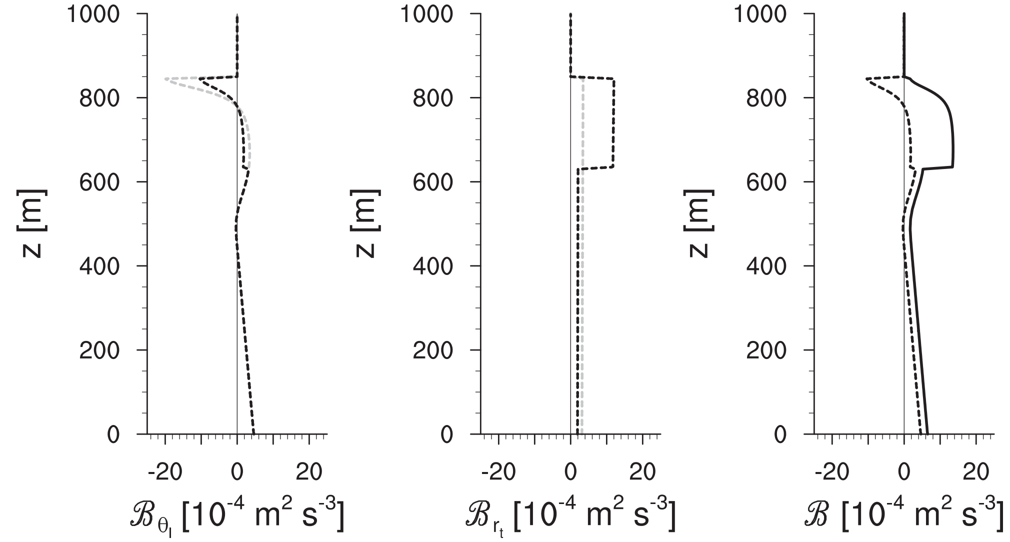

Figure 4.3: Turbulent buoyancy fluxes for the NS with more realistic radiation fluxes. Colors and lines as in Fig. 4.2.

Before addressing the question of drizzle, though, let us first examine the effect of the simplification of the forcings by repeating this analysis with more realistic radiative fluxes, namely those from the NS. Turbulent fluxes of θ_l, r_t and $\mathcal{B}$ in such conditions are illustrated in Fig. 4.3. With this interpretation of radiation, the buoyancy fluxes are positive through the depth of the STBL, which indicates that our simplification of the forcings produces larger estimates of the BIR and that our subsequent analysis of the energetics in the presence of drizzle might be of the same character. However, one should not find this caveat limiting, as this overestimate of decoupling reduces the chances of inaccurately applying the MLM to unsuitable systems.

c. *Impact of Drizzle on the STBL Energetics*

Having laid out all the basic theory, we return to the question of drizzle impact on the STBL in the MLM framework. Considering that the total effect of drizzle on the STBL is warming and drying, one could ask what would be the most suitable representation of drizzle in the MLM framework. Diagnosing the state of the DS by following the same analysis we did above for the NS would include all the interactions that the system would develop in the presence of drizzle, while imposing the drizzle fluxes only on the buoyancy fluxes already calculated for the NS would isolate only the direct effect on the energetics. In this stage of the analysis, we are interested only in the latter, namely the direct effect of drizzle on the energetics. However, even this limit, it is a matter of interpretation whether drizzle effects should be projected onto the boundaries. As we have seen in the previous section, this simplification of the radiative forcing overestimates decoupling, and we first evaluate whether it has the same effect for the drizzle forcing.

As noted above, Fig. 4.1 illustrates a drizzle profile from the DS that is stretched to match the depth of the NS boundary layer, along with its simplification to the projection to the boundaries. In this representation, the drizzle profile is simplified to a linear shape, with the surface value unchanged and the top value adopting the strongest pre-

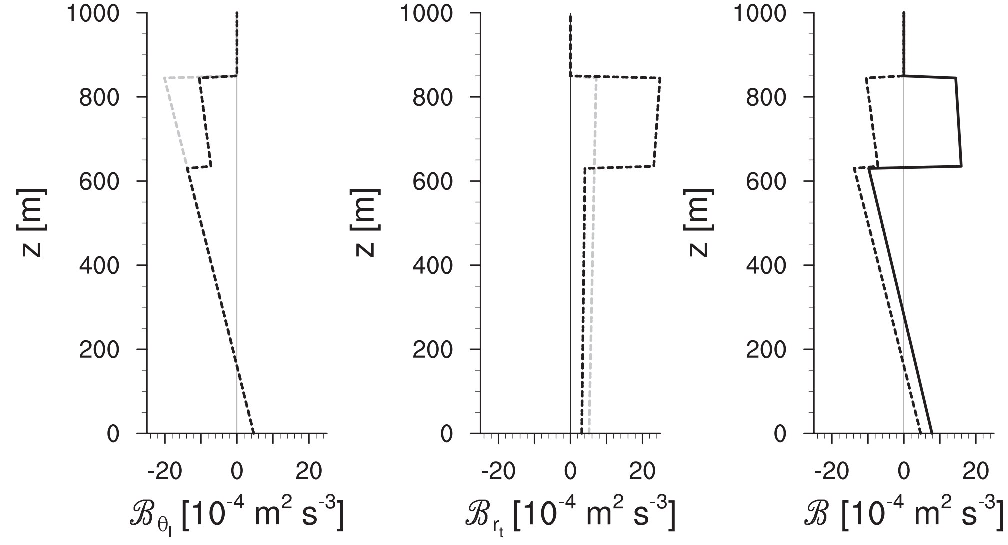

Figure 4.4: Turbulent buoyancy fluxes for the bulk layer evolving as in the NS, but drizzling as in the DS. Diabatic forcings are projected onto the boundaries. Colors and lines as in Fig. 4.2.

cipitation value. The fluxes resulting from this type of forcing are illustrated in Fig. 4.4, which in the limit of the projected forcings essentially depicts the buoyancy fluxes of a bulk layer that would drizzle as much as the DS but otherwise evolve as the NS. As expected from the similarity between the overall effects of drizzle and entrainment, a layer of negative buoyancy fluxes atop the subcloud layer becomes significantly deep, while the negative values of buoyancy fluxes strengthen in these conditions. This means that in the presence of drizzle turbulence has to do a considerable amount of work to mix the air through the depth of the boundary layer. As mentioned before, the significance of this need for turbulence to do extra work is discussed in previous studies in terms of diurnal and deepening-warming decoupling by Turton and Nicholls (1987) and Bretherton and Wyant (1997), but there is no study of drizzle-induced decoupling. The BIR for this simplified representation of the bulk layer is 39%, which according to the condition for decoupling defined by Stevens (2000) suggests that the

MLM framework would provide a misrepresentation of drizzle, because this bulk layer would not be energetically consistent.

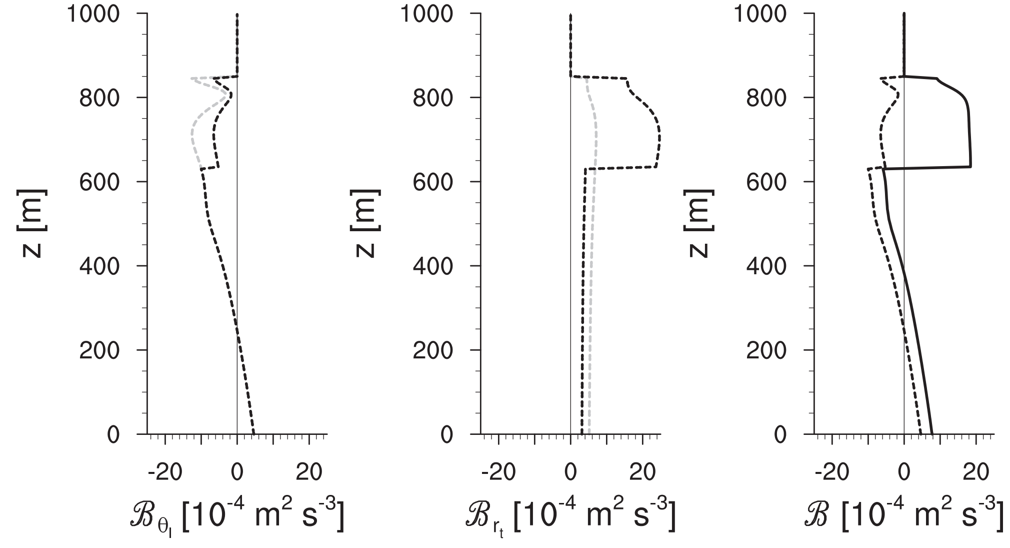

Figure 4.5: As Fig. 4.4, but with the forcings introduced through the depth of the boundary layer. Colors and lines as in Fig. 4.2.

Since the above representation of drizzle is likely too simplistic, because the real effect of drizzle is mostly in the layer interior, near the cloud base and away from the boundaries (Fig. 4.1), we repeat the above analysis but with a more realistic treatment of forcings. Due to the discrepancy in the depth between the drizzling and the non-drizzling STBL in our simulations, to match the depth of the NS boundary layer, the drizzle profile from the DS is stretched (as in Fig. 4.1). Likewise, to assure the consistency of the bulk representation, we also employ more realistic radiation fluxes instead of the ones projected onto the boundaries. Figure 4.5 illustrates the resulting fluxes and evinces the reduction of the BIR compared to the above simple representation: 17% versus 39%, respectively. This again confirms that in the presence of drizzle a substantial amount of turbulence produced by the radiative cooling and surface fluxes would need to be consumed to mix the air vertically, which is an unrealistic expectation from the system and suggests decoupling. To the extent that the drizzle does not interact with the entrainment and radiative processes, which would eventually affect the heights of the STBL and LCL, this analysis also indicates that the MLM framework would not be suitable for predicting the evolution of this particular drizzling STBL. In spite of the lack of interactions, this analysis of the energetics is also in agreement with our analysis in Chapter 3, where we have seen the development of the slight vertical gradients in the state variables, especially in r_t.

A thought experiment could help us gain a perspective on the question of the lack of the interactions in our analysis that actually exist in the realistic drizzling STBL. For instance, precipitating Sc tend to have smaller liquid-water paths than the non-precipitating (Fig. 3.9). With less cloud water, one would expect thinner clouds than the ones in the NS that we applied our analysis to. If the boundary-layer depth was not affected, that would lead only to higher cloud base and therefore even more negative buoyancy fluxes, which would increase confidence in our conclusion. Furthermore, the thinner the clouds, the smaller the integral of positive buoyancy flux, which increases the ratio of the integral of negative over the integral of positive buoyancy fluxes, or BIR. However, this representation would be unrealistic too, as the drizzling STBL grows less than the non-drizzling (Fig. 3.9). Adjusting for the height of the STBL would reduce the negative part, but would have no effect on the in-cloud, positive buoyancy flux. Regardless of the value of the ratio of negative and positive buoyancy fluxes, or BIR, one could argue that the radiative driving would be reduced too, which we do not address here directly, although we discuss the slower growth of the drizzling STBL, which is partially a reflection of reduced radiative forcing. This reduction in the radiative forcing would additionally affect the energetics by augmenting the negative part of the buoyancy fluxes. Following this thought experiment, one could question whether any interaction of drizzle with other processes in the STBL would significantly reduce the negative integral of buoyancy fluxes. From the simulations in the previous Chapter, we find a significant reduction in entrainment in the presence of drizzle, which could lead toward the reduction of the BIR and encourages the evaluation of the range of precipitation and entrainment intensities in which the energetics of the STBL would consistently allow the utilization of the MLM.

To quantify the decoupling in the precipitation-entrainment space, we return to the forcing projected onto the boundaries. We keep this simple representation of forcings because it allows us to easily expand the analysis to a wider range of precipitation and entrainment values than attained by the DS and NS. Nevertheless, since this representation of forcings overestimates decoupling, we stress that it also provides a more narrow range of drizzle that would provide energetically consistent bulk layer. Figure 4.6 depicts the BIR as a function of intensity of surface precipitation and entrainment with two portrayals of the drizzle rate within the boundary layer, which stem from keeping either a difference (left panel) or a ratio (right panel) of surface and boundary-layer top values equal to the ones estimated from the DS. By keeping the difference constant, we mimic the drizzle-induced heating and moistening rates from the DS, while by keeping the ratio constant, we adjust the drizzle-induced heating and moistening rates to what could be expected to be more realistic given the surface values. In particular, the BIR illustrated in these figures is calculated for the bulk layer that evolves as the NS, but with altered entrainment and drizzle rates imposed on it. Although too simplistic and potentially unrealistic, this approach helps isolate important effects without changing the system as a whole. Stippled region in these figures indicates the area where the boundary layer is well mixed, while grey color covers the decoupled area of this parameter space.

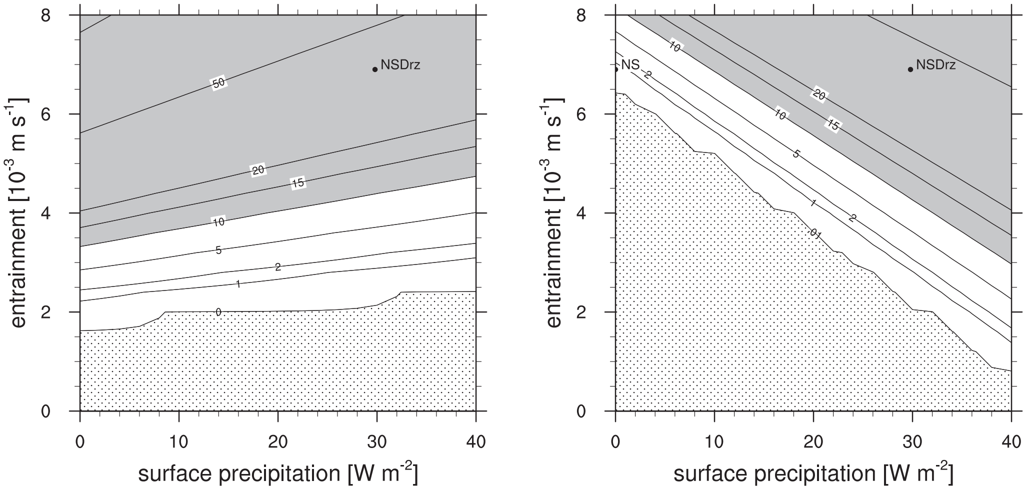

Figure 4.6: BIR in terms of the surface precipitation and entrainment rate, with projected forcing. The precipitation rate imposed to the NS STBL is defined by keeping either a difference (left panel) or a ratio (right panel) of surface and boundary-layer top values equal to the ones estimated from the DS.

The left panel in Fig. 4.6 depicts the ranges of the BIR that develop in the NS STBL if it entrained within the range of 0 to 8 $\times 10^{-3}$ m s^{-1}, and precipitated with surface values ranging from 0 to 40 W m^{-2} while keeping the vertical slope of the precipitation equal to the one of the DS. This figure illustrates that with given constraints, the decoupling is mostly determined by entrainment. More precisely, for entrainment weaker than 3.5 $\times 10^{-3}$ m s^{-1} and stronger than 5 $\times 10^{-3}$ m s^{-1} drizzle intensity does not affect the state of the STBL that is defined by entrainment (mixed for less than 3.5 and decoupled for more than 5 $\times 10^{-3}$ m s^{-1}) , while for entrainment between 3.5 and 5 $\times 10^{-3}$ m s^{-1}, the STBL is in a fragile state in which drizzle strength determines if the boundary layer will be decoupled or not. In these conditions, for the entrainment values estimated from the DS, 4 $\times 10^{-3}$ m s^{-1}, drizzle from the DS would lead to the STBL in which turbulence has to do significant amount of work to vertically mix the air, while the drizzle that wouldn't reach the surface would lead to the decoupling. Nonetheless, this experiment does not lead to the NS in the limit of zero precipitation at the surface, so one should not confuse the BIR values at zero precipitation in this figure with the BIR values for the NS with various strengths of entrainment. In the NS, not only is the surface value of precipitation equal to zero, but also the values through the depth of the STBL. To investigate the effect of changes in the precipitation strength in limit of constant drizzle flux through the depth of the STBL, we calculate the BIR for the same range of entrainment and surface precipitation fluxes as above, but with zero vertical slope for precipitation. These results are quite unrealistic, as even with the surface precipitation of 40 W m^{-2} and entrainment rates of 8 $\times 10^{-3}$ m s^{-1} the STBL stays well mixed, so we do not show the plot. However, they do indicate that the most important aspect of the effect of precipitation is not its surface value, but the rate of evaporation/condensation within the boundary layer, which warrants further analysis.

Keeping the drizzle-induced heating/moistening rate constant for all the strengths of surface precipitation is quite questionable. To have a more realistic drizzle representation, we vary the vertical slope of precipitation along with the surface values by keeping the ratio of values at surface and boundary-layer top equivalent to the ratio estimated from the DS. The right panel in Fig. 4.6 depicts these results and indicates a general trend toward a decoupled state with stronger precipitation and entrainment. It also indicates that through almost the entire range of entrainments shown here, the drizzle strength determines the boundary-layer state. For instance, for a realistic drizzle intensity of 30 W m^{-2}, the STBL stays well mixed for entrainment rates lower than 2 $\times 10^{-3}$ m s^{-1}, while for drizzle weaker than 3 W m^{-2}, the STBL stays approximately well mixed regardless of entrainment. For any value of entrainment, however, there is a window of about 15 W m^{-2} of surface precipitation that distinguishes the well-mixed STBL from the decoupled bulk layer. One could interpret this as a limit of the additional drizzle intensity that a bulk layer could sustain and remain well-mixed. The above analysis shows that these simplifications of the forcings overestimate the decoupling, and so these numbers are not an absolute criteria, but rather a guidance toward more cautious application of the MLM to the evolution of the drizzling STBL. However, if the overestimate of the BIR is independent of the strength of forcings, one could keep in mind the limit of 15 W m^{-2} (0.5 mm day^{-1}) that separates the two distinct states of the bulk layer. This value does not change when the analysis is repeated with radiative forcing reduced to the value in the DS. To the extent that the projected forcings and described limitation of the rates of precipitation are valid, we find that the only effect of such a reduction in the radiative forcing to be a slight restriction of the domain for which the STBL is coupled and a slight expansion of the domain of the decoupled STBL, so we do not plot those results but rather note their support of the above-described thought experiment.

To summarize, our analysis indicates that the MLM and the decoupling theory successfully explain the simulations examined in Chapter 3, because the NS cannot sustain the drizzle intensity from the DS without undergoing some transition (one we see in the DS). Moreover, it also suggests that one should be careful when relating drizzle to the decoupling. We find no direct association of drizzle with the decoupling, but that instead a given STBL could actually support a range of drizzle intensities before even developing any positive value of the BIR. In addition, if one thinks of the drizzle intensity that leads to an infinitesimally small value of the BIR as a "fragility threshold", and its intensity for which the STBL becomes decoupled as a "decoupling threshold", we find that the difference in the precipitation between the two thresholds is about 15 W m^{-2} (0.5 mm day^{-1}) for the bulk layer that evolves as in the NS. This indicates that the heating and moistening rates of the NS produce turbulence that can sustain 15 W m^{-2} of additional surface precipitation after reaching the point that it has to do any work to mix the air vertically. With this in mind, we find it encouraging to extend the analysis to a wider parameter space that would not only expand the range of interactions within the system, but also explore the variations in the evolution of the bulk layer. Such an analysis could significantly contribute to the understanding of the dynamical basis for cloud transformations.

Independent of decoupling, though, note that the bulk approach neglects the localized nature of drizzle and resulting interactions with the flow on the scales smaller than the domain size of the simulations from Chapter 3. How does this reflect on the flow? Or, what kind of flow would develop if drizzle were treated as a horizontally-uniform forcing? To what extent would it represent the drizzling STBL we introduced in Chapter 3? The following section is devoted to answering these questions.

4.2. Drizzle as a Mean Forcing

In our analysis of the drizzle effect in the MLM framework, we chose to treat drizzle in a horizontally uniform sense and to neglect all the possible interactions with other aspects of the flow, which is the simplest representation of drizzle we could start building upon. Even in such a representation, the drizzling STBL seems to develop into a flow that cannot stay vertically well mixed. Before introducing the possible interactions in the MLM framework, it would be instructive to diagnose the extent to which the drizzle effect is captured if drizzle-related diabatic forcing is present only in the mean-state, horizontally-uniform sense in a large-domain LES.

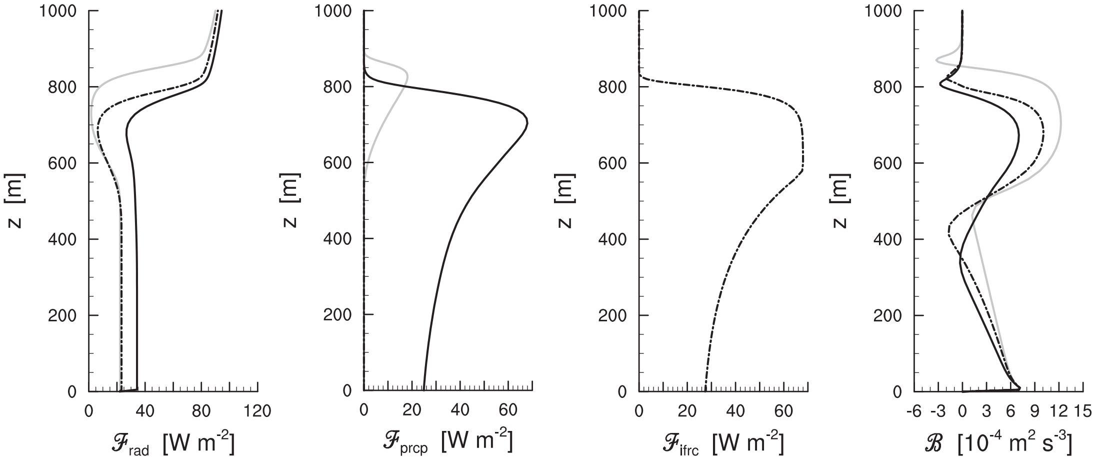

Figure 4.7: Mean profiles of radiation (far left), precipitation (left), imposed forcing (right) and buoyancy (far right) fluxes for the NS (solid gray), DS (solid black) and MFS (dash-dotted black).

An investigation of the evolution of the STBL in which drizzle-mimicking forcing is treated only in a mean sense is conducted by analyzing a large-domain LES performed with the initial and environmental conditions of the NS, but with the imposed horizontally uniform forcing that corresponds to the domain-mean drizzle in the DS. We refer to this simulation as to MFS (Mean-Forcing Simulation). Figure 4.7 illustrates the mean profiles of precipitation in the NS and the DS and the profile of imposed forcing, which follows the shape of profile that precipitation has in the isolated drizzling cell (Stevens et al. 1998). Although precipitation in the DS and imposed forcing in the MFS are not identical, the main properties of the forcing from the precipitation, such as the surface value and the maximum value in the cloud, are captured in the imposed forcing, giving us confidence in the following comparison.

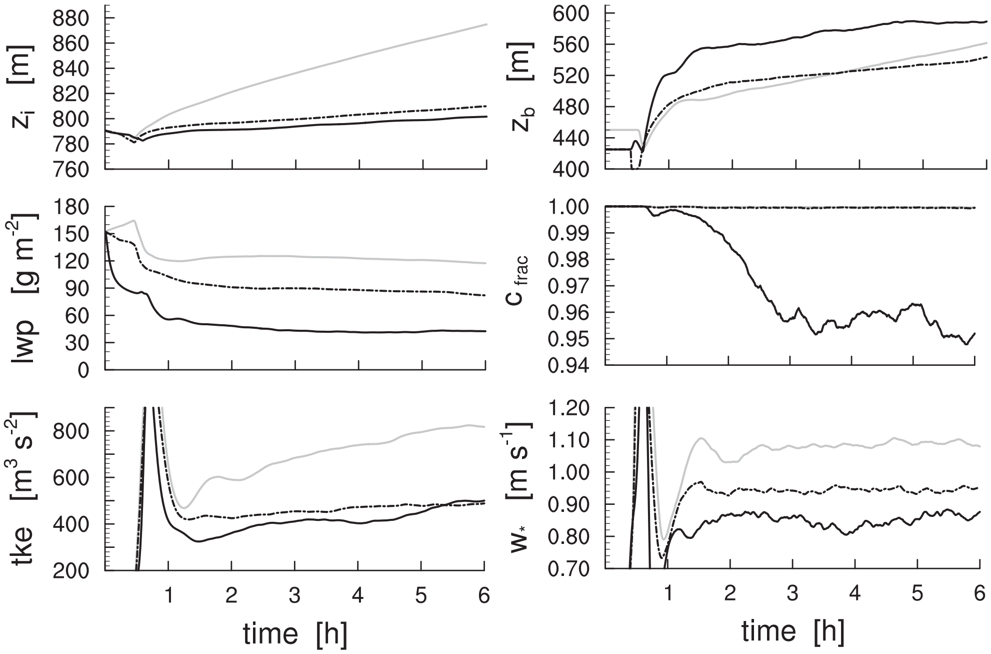

Figure 4.8: Time series of domain-averaged inversion height (top left), liquid-water path (middle left), turbulence kinetic energy (bottom left), cloud-base height (top right), cloud fraction (middle right) and buoyancy velocity scale (bottom right) for NS, DS and MFS. Colors and lines as in Fig. 4.7.

Figure 4.7 also depicts the radiation flux present in the simulations and the resulting buoyancy flux. Reduced radiation flux divergence in the DS relative to the NS is due to the lower cloud coverage in the DS, which is documented in Chapter 3. This feature seems to be missing from the MFS. Likewise, buoyancy fluxes in the MFS and the DS differ, with the MFS having stronger forcing in the cloud layer when compared to the DS, and developing a slightly stable layer atop the subcloud layer.

To further analyze the impact of these discrepancies on the evolution and structure

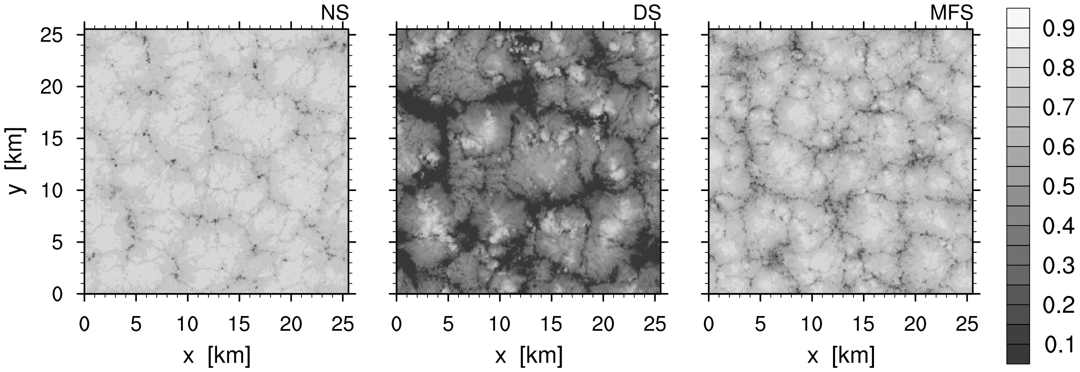

Figure 4.9: Albedo, as per Eq. (3.1), at the end of the 6^{th} h of the NS, DS and MFS.

of the STBL, we compare the statistics of the MFS to the statistics of the DS and the NS. We first analyze the evolution of the domain-mean properties of the STBL (Fig. 4.8) and find that the energetics of the MFS agree quite well with the energetics of the DS. In addition to the agreement of the boundary-layer depth, or inversion height, z_i, there is very good agreement between the vertically integrated turbulence kinetic energy in the MFS and in the DS. The only discrepancy is in the buoyancy velocity scale, w_*. Nevertheless, the values of w_* in MFS are somewhat closer to its values in the DS than in the NS, which further supports our statement that the MFS represents the energetics of the DS to a good degree.

The evolution of the cloud field, on the other hand, shows large contrast between the two simulations that represent (DS) and mimic (MFS) drizzle. In fact, the cloud base and cloud cover of the MFS agree with these cloud properties in the NS, while the liquid-water path is approximately an average value between the NS and the DS, because the cloud-top height follows the DS cloud-top height. Realizing that the major impact of removing the localized nature of the forcing due to drizzle is the inability of the simulation to reproduce the horizontal variability of the cloud field, which was

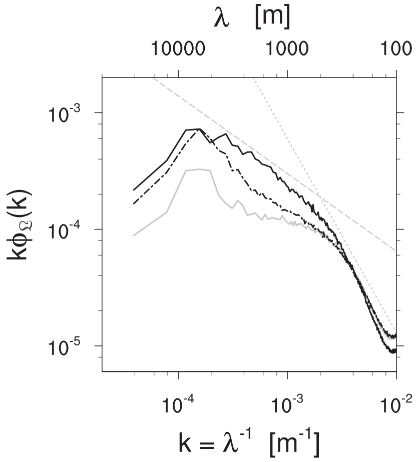

Figure 4.10: Spectral energy density for LWP in the NS, DS and MFS. Colors and lines as in Fig. 4.7.

also hinted at by the radiation profiles, one could ask what can we learn from these differences. Examining the albedo for the three simulations (Fig. 4.9) clarifies that, although the cloud fraction in the MFS is effectively 100%, as in the NS, the cloud field develops wider areas of thin clouds and more localized high albedo values than in the NS: The average albedo in the MFS is 10% lower than in the NS, while the maximum values are comparable between the two simulations. These features seem to be more drastic in the DS, though. Spectral analysis of the liquid-water path (Fig. 4.10) indicates agreement of the MFS with the DS on the larger scales and with the NS on the small scales. However, because there is a whole range of scales where MFS cloud organization disagrees with either DS or NS, one could conclude that the localized forcing affects the cloud topology, but that the intensity of the flow stems from its interaction with the mean drizzle-induced forcing.

How does the MFS forcing affect the mean vertical structure of the boundary layer? Figure 4.11, illustrating the mean profiles of θ_l, r_t and r_l, indicates that the cloud layer

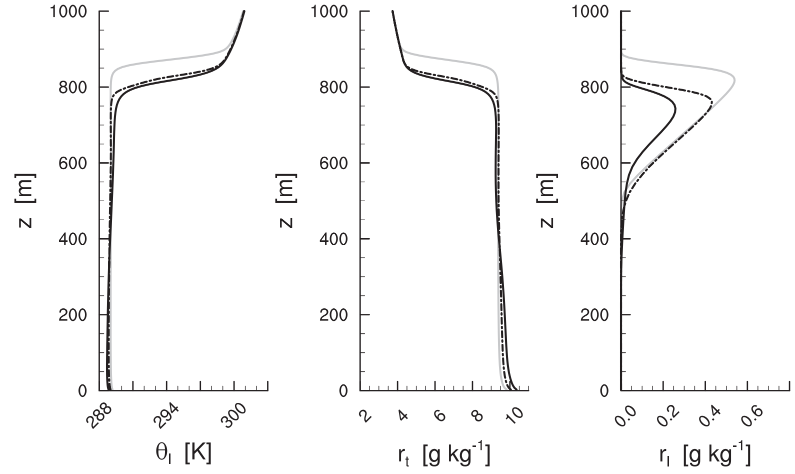

Figure 4.11: Mean profiles of θ_l, r_t and r_l for NS, DS and MFS. Colors and lines as in Fig. 4.7.

thermodynamic state is almost identical between the NS and the MFS, which could be attributed to the lack of the divergence of the imposed-forcing fluxes within the cloud layer of the MFS. However, because our representation of the imposed forcing has similar properties as a profile of precipitation from only one drizzling cell in Stevens et al. (1998), where the more realistic bin parameterization of drizzle was utilized, we conclude that this effect is not artificial. Furthermore, Fig. 4.11 illustrates that the subcloud layer of the MFS is colder and moister than for the NS, but not to the extent of the DS. These slightly altered conditions within the subcloud layer affect the cloud base height indicating development of slightly more heterogeneous cloud base than in the NS. From the differences in the mean profiles of the simulations with fully developed interactions and with imposed domain-mean forcing, one could conclude that in the presence of localized interactions of the flow and forcing the cloud layer develops horizontal heterogeneousness that reflects on the mean profiles. In addition, this comparison also indicates that the changes within the subcloud layer occur regardless of the localization of the forcing, but are augmented by the local interactions.

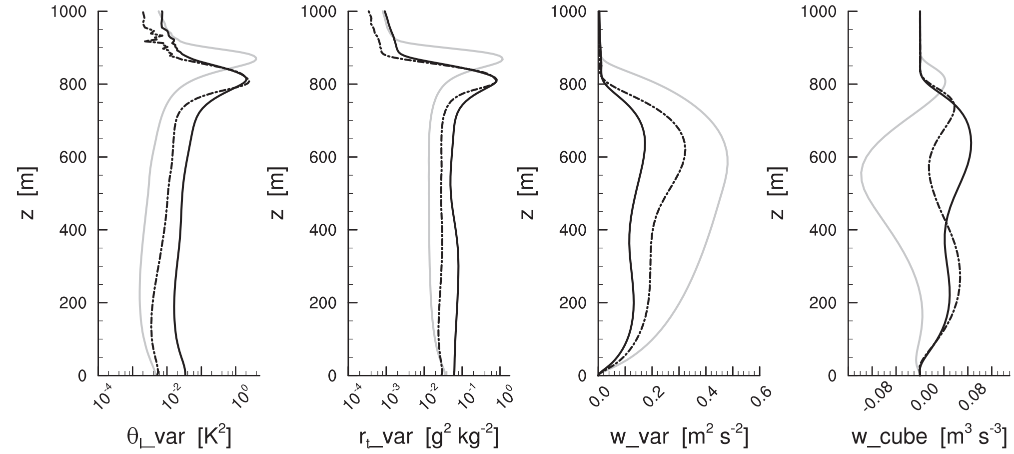

Figure 4.12: Mean profiles of variances of θ_l, r_t and w, and third moment of w for the NS, DS and MFS. Colors and lines as in Fig. 4.7.

As discussed in Chapter 3, increased horizontal variability in the thermodynamic state of the drizzling STBL is one of its most striking properties. The MFS partially captures this important feature, indicating that the localized forcing is not the only source of the increased horizontal variability (note that the logarithmic scale in Fig. 4.12 visually reduces the similarity between the MFS and the DS). The source of the variability in the MFS seems to be a reduced strength of the circulation relative to the NS (TKE in Fig. 4.8). This weaker circulation in the MFS is confirmed by the variance of the vertical velocity (Fig. 4.12), which is not only reduced from the NS, but also starts developing a bimodal distribution, a signal of the differentiation between the cloud and subcloud layer, as seen in the DS. Vertical-velocity variance of the MFS agrees less with the DS in the cloud than in the subcloud layer, which befits the discrepancies in the buoyancy profiles discussed above. This again suggests that the localized drizzle-induced forcing is responsible for the changes in the cloud structure, as mentioned above with respect to the cloud topology. The most striking difference between the MFS and the DS is seen in the third moment of vertical velocity, where in the cloud layer a dominance of the strong-updrafts in the DS is replaced with almost a balance between the updrafts and downdrafts in the MFS ($\overline{w^3}$ is near zero).

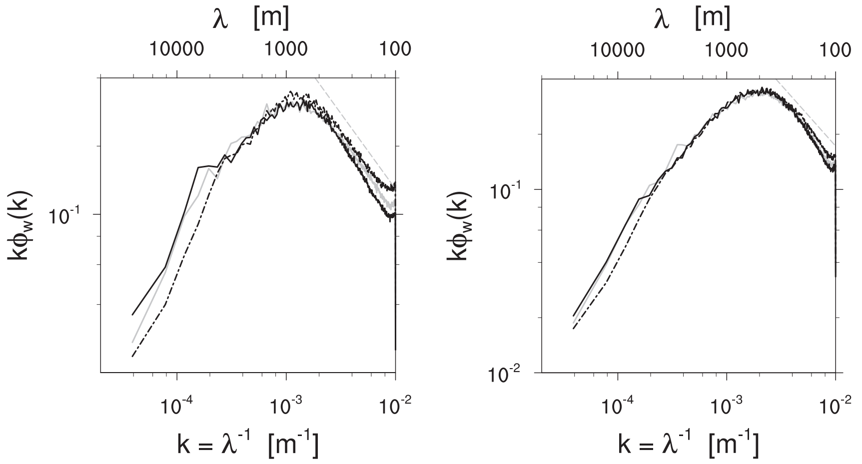

Figure 4.13: Normalized spectral energy density for w for NS, DS and MFS. Colors and lines as in Fig. 4.7 Left: at 200 m height. Right: at 0.9 z_i height.

From the buoyancy profiles in Fig. 4.7, one would expect development of a stronger circulation in the cloud layer of the MFS than in the DS. Because the vertical-velocity variance confirms this expectation, we conclude that in the absence of the collocation of the forcings and the flow (in the MFS), strong updrafts cannot be balanced by the weak downdrafts spreading over the large area (as in the DS), but are instead balanced with the downdrafts of similar intensity and covering almost the same area as updrafts. To rephrase, localized forcing allows for the development of the organization of the larger scales in the flow, as observed by Paluch and Lenschow (1991) and Comstock et al. (2005). The horizontally uniform forcing, on the other hand, constrains the flow to the smaller scales, which is especially noticeable in the development of the cloud field. Spectral analysis of the vertical velocity (Fig. 4.13) confirms the lack of development of the larger scales in the MFS, while revealing that the development of the larger scales in the DS originates in the subcloud layer (left panel). To that end, the MFS potentially provides a good answer for the wrong reason, with the cloud field being an indicator of such a behavior. In addition to the reduced circulation strength, which MFS captures, the drizzling STBL in the DS develops the larger scales in the flow organization that drive the cloud morphology.

To recapitulate, drizzle-mimicking, horizontally-uniform forcing (the MFS) drives the strength of circulation, but lacks the ability to reproduce the cloud field that develops in the drizzling simulations that allow for the localized interactions of drizzle and flow (the DS). More cumulus-like cloud organization present in the DS is replaced with slightly broken stratocumulus in the MFS. This behavior is a consequence of the inability of the MFS to reproduce the flow organization of the DS: In spite of the similar intensity of the circulation between the MFS and the DS, the horizontally-uniform forcing (MFS) reproduces neither development of large-scales in the flow, nor the updraft-dominated circulation in the cloud layer that are present in the DS.

With this discrepancy in the flow and cloud organization between the localized and horizontally-uniform drizzle-related forcings in mind, we proceed with our analysis by relating the circulation strength to the budgets of θ_l and r_t. In particular, since one would expect from the MLM argument that θ_l is the driver of the circulation, we attempt to substantiate this argument and to explore the role of moisture in the following section.

4.3. Drizzle Interaction with Thermodynamic Fields

As discussed in the previous section, treating drizzle in a horizontally uniform sense and neglecting the collocation of the forcing and the flow features gives energetically same result as when allowing the full interaction. Taking a step further in this direction could clarify which aspect of the forcings leads to such a result. In particular, investigating separately the effect of the mean forcing on the θ_l budget and on the r_t budget could help isolate the individual contributions of these fields to changes in the energetics due to drizzle.

Because the drizzle-mimicking, horizontally uniform forcing lacks the development of the larger scales, and in the interest of reducing computational costs, the following study is based on a GCSS-domain size LES. Although we preserve the nomenclature for the NS, DS and MFS used above, in this particular section they refer to simulations with a horizontal domain size of 6.4 x 6.4 km, but with conditions and forcings from the large-domain simulations discussed in previous section. To differentiate the impacts on the θ_l and r_t budgets, two more simulations are performed: a simulation with a horizontally-uniform impact only on the θ_l field, named MHS (Mean-Heating Simulation), and a simulation with the mean forcing only on the r_t field, named MMS (Mean-Moistening Simulation).

Since the driving force of the turbulence in the STBL is the radiative cooling at the top of the cloud, and since in the MLM framework θ_l fluxes drive the development of negative buoyancy fluxes at the top of the subcloud layer, one would expect that the MHS fully represents the energetics of the DS. The evolution (Fig. 4.14) of the mean STBL energetic properties in the described simulations confirms this expecta-

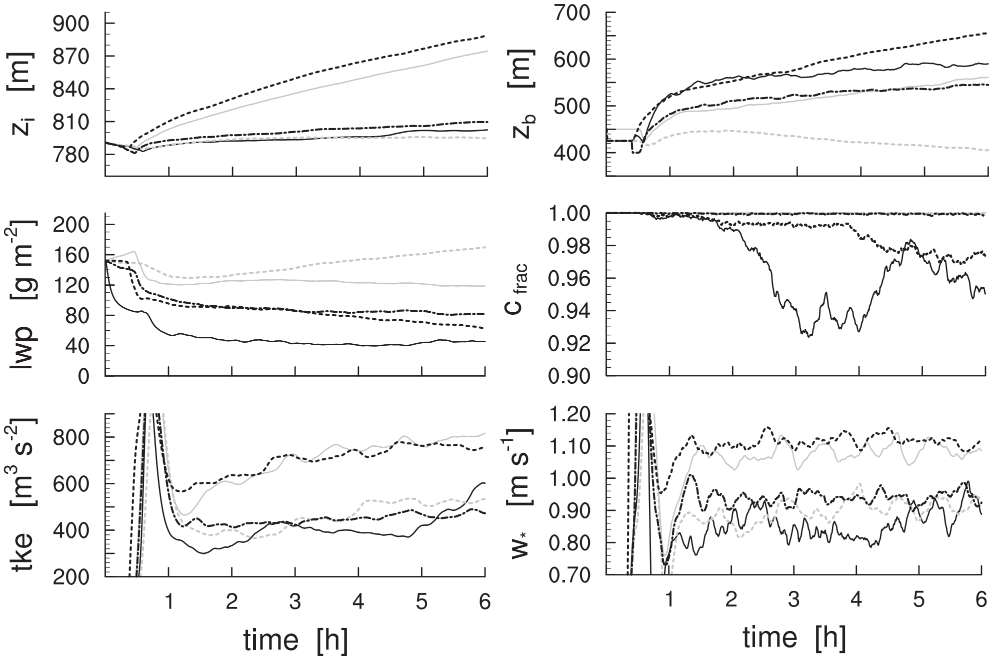

Figure 4.14: Time series of domain-averaged inversion height (top left), liquid-water path (middle left), turbulence kinetic energy (bottom left), cloud-base height (top right), cloud fraction (middle right) and buoyancy velocity scale (bottom right) for NS (solid gray), DS (solid black), MHS (dotted gray), MMS (dotted black) and MFS (dash-dotted black).

tion. In spite of the lack of effect on the moisture budget, the MHS (gray dotted line in Fig. 4.14) just slightly underestimates the growth of the STBL with respect to the DS (solid black line) and the MFS (dash-dotted black line). The MMS (black dotted line), on the other hand, follows the growth of the NS. The MHS and MMS show corresponding differences for the TKE and w_* too, suggesting that the MHS reproduces the DS energetics to a reasonable degree, while the MMS follows the energetics of the NS. This leads to the conclusion that the effect of the forcing on the heat budget seems critical.

The cloud topology of the DS, on the other hand, is not reproduced by any of the simulations with horizontally uniform forcing, sustaining the conclusion that the collocation of the forcing due to drizzle and the flow development is essential for the development of the cloud structure as observed by, *e.g.*, Comstock et al. (2005) and vanZanten and Stevens (2005). However, the MMS cloud fraction reduces to the DS values in the last hour of the simulation, suggesting that the interaction of drizzle with the moisture budget results in a change of cloud organization. Because the rise of cloud-base is highest in the MMS compared to any other simulations, one could argue that the cloud reacts to the overall drying of the STBL due to the drizzle. In addition, the fastest decline of the LWP in the last hour of the MMS, when the cloud fraction reduces to the DS values, could suggest that even in the conditions of horizontally uniform drying of the STBL, the cloud starts reorganizing due to the potential buoyancy described by Stevens et al. (1998). In the MMS, due to the loss of the liquid water from the cloud, downdrafts originating at the cloud tops reach their lifting-condensation levels at heights above the lifting-condensation levels of updrafts, and therefore locally elevate the cloud bases, which eventually could lead to the development of the patches of cloud-free air. This effect, however, seems to be of less importance for the overall drizzle-induced change in the cloud structure than the localized interactions of the forcing and the flow that allow development of the larger scales, because in the MFS, where both moisture and temperature budgets are affected, the cloud field does not seem to experience any change in the organization. Furthermore, this effect could suffer from the domain size of the simulation, and one should follow up this analysis with the large-domain LES to ensure that the statistics are correct and that the flow has enough space to reorganize without feeding only one cell.

Profiles of mean θ_l and r_t (Fig. 4.15) indicate a lack of decoupling in both the MHS and the MMS. In both of these simulations, the boundary layer is well mixed, while the

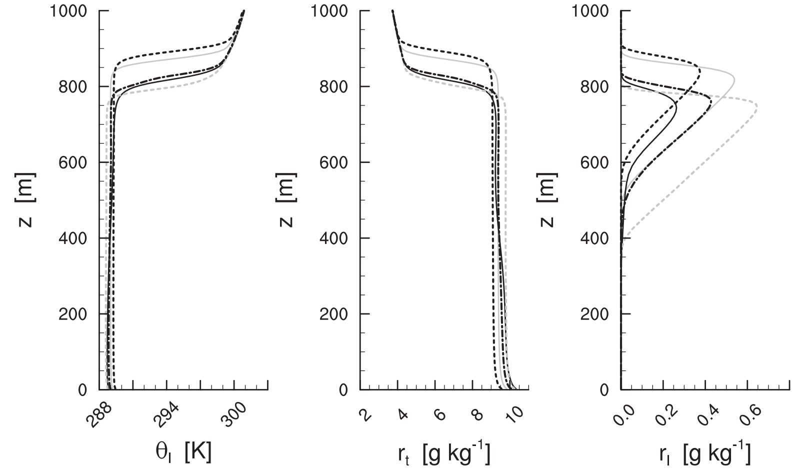

Figure 4.15: Mean profiles of θ_l, r_t and r_l for NS, DS, MHS, MMS and MFS. Colors and lines as in Fig. 4.14.

MFS, as noted in the section 4.2, develops a slight differentiation between the cloud and subcloud layer. In the MFS, a hint of Cu clouds in its r_l profile also forms, indicating that only when both temperature and moisture budgets are affected, can decoupling occur. The puzzling question left, though, is why the cloud fraction in the MFS stays so high. Synthesizing all the simulations, one explanation could be that the decoupling in the sense of the development of two distinct, horizontally-uniform layers actually does not occur in the drizzling STBL. Instead, it seems that in the DS the stabilization of the subcloud layer occurs only locally where the forcing of the θ_l budget takes place (cold pools), while the rest of the flow conforms to that interaction and reorganizes into larger scales that further support the development of drizzle, which then dries the downdrafts and changes the cloud structure (Paluch and Lenschow 1991; Stevens et al. 1998). However, because the MFS is artificially driven at each point in the horizontal direction equally, the development of the localized circulation is prevented, disabling this sequence of processes, and leading to the horizontally more uniform cloud field.

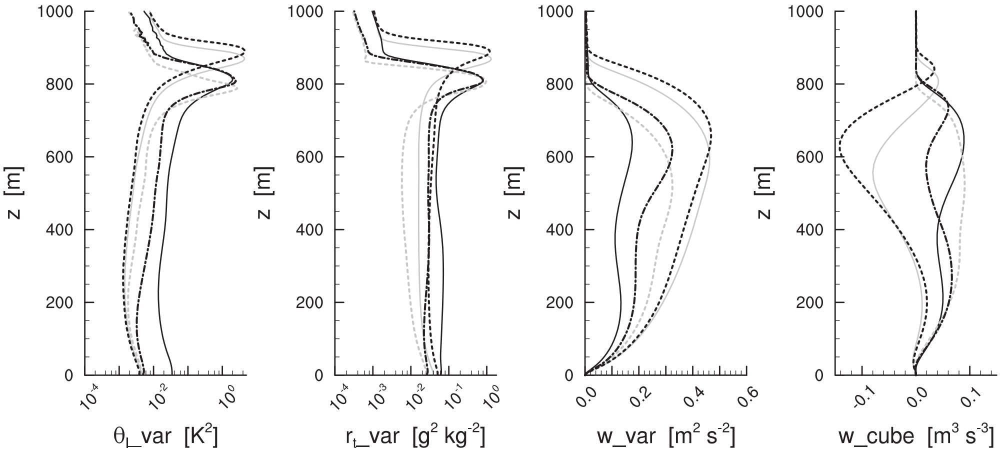

Figure 4.16: Mean profiles of variances of θ_l, r_t and w, and third moment of w for the NS, DS, MHS, MMS and MFS. Colors and lines as in Fig. 4.14.

Mean profiles of the variance and the third moment of vertical velocity also indicate a well mixed STBL if only one budget is affected (Fig. 4.16). However, only when the θ_l budget is altered (MHS and MFS), downdrafts in the cloud layer become weak and allow dominance of the updrafts. Furthermore, the w variance confirms a weaker circulation when only θ_l is affected by the imposed forcing, and about the same strength as in the NS when the r_t is driven. These strong downdrafts in the MMS, in the absence of moisture from the could layer, could be the cause for the cloud breakup. Only by forcing both moisture and temperature budgets simultaneously, as in the MFS, a separation between the cloud and subcloud layers occurs. Finally, subcloud layer seems to react more to the changes in the θ_l budget, while the cloud layer reacts more to the forcing of r_t.

Figure 4.16 also illustrates the variances of θ_l and r_t, which are challenging to interpret. In the MMS, the variance of moisture actually disagrees with the argument that a weaker circulation leads to increased horizontal variability, because this simulation has the strongest circulation and yet the highest variability in the moisture field, especially in the cloud layer. However, in the MMS, the r_t field is forced in such a way to allow the potential buoyancy to overcome the effect of the circulation strength. The MHS, on the other hand, conforms to the reduced circulation argument and provides slightly stronger variability in the temperature field, but fails to do so for the moisture field. One argument, though, for so weak horizontal variability in the moisture field in the MHS could be a signature of the overall abundance of moisture and well mixed state of the STBL in the MHS.

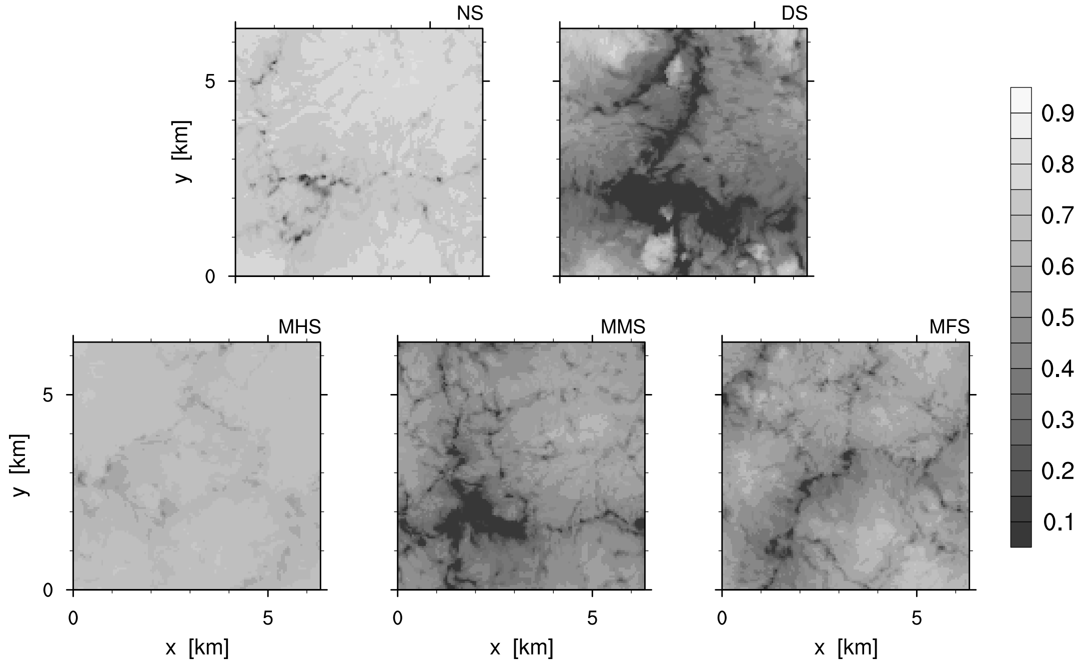

Figure 4.17: Albedo, as per Eq. (3.1), at the end of the 6^{th} h of the NS, DS, MHS, MMS and MFS.

An instantaneous planar view of the cloud fields at the end of each simulation in

Fig. 4.17 visualizes the effects of different budgets on the cloud layer. When only horizontally uniform heating is applied, the clouds hardly experience any changes compared to the NS, while the horizontally uniform drying starts the “cloud erosion”, but not nearly as much as in the DS. When both mean heating and moistening are imposed clouds start having more structure, but they are still rather different from the DS clouds.

To summarize, the drizzle effect on the moisture budget does not change the energetics of the flow and the strength of circulation. It only affects the cloud structure by preconditioning the downdrafts for the elevation of the local cloud base and eventual removal of the cloudy air. This effect of moisture occurs regardless of whether drizzle is treated in a mean or localized manner. The drizzle effect on the temperature field, on the other hand, drives the energetics of the flow by reducing the intensity of the circulation, if drizzle is present in the mean sense, and by development of the larger scales in the flow, on top of the weaker circulation, if localized interactions are allowed. This increase in the scales of the flow seems to be a leading source of the changes in the drizzling STBL, which are brought to the full extent of broken clouds by the moisture removal from the cloud field through the effect on the r_t budget.

4.4. Summary

In this Chapter, we investigate the dynamics of the drizzling STBL by addressing the following questions: To what extent can the drizzling STBL be represented in the MLM framework? Which features of the drizzling STBL are captured in the simulations with horizontally-uniform, drizzle-mimicking forcing? And, what is the role of each thermodynamic budget in the drizzle-induced transformations of the STBL?

Investigating consistency of the energetics of the bulk layer that drizzles as in the DS from Chapter 3, and otherwise evolves identically to the NS, we find that the MLM and the decoupling theory successfully explain the transitions present in the drizzling simulation from the previous Chapter, as such bulk layer cannot sustain a well-mixed state. Moreover, the analysis of the energetics of the flow that evolves as in the NS, but drizzles within a given range of intensities at surface also suggests that one should be careful when relating drizzle to the decoupling. There is no evidence of direct association of drizzle with the decoupling, but instead we find that a given STBL could actually support a range of drizzle intensities before even developing any positive value of the BIR, and that the turbulence within it could even support additional precipitation before fully decoupling. For the heating and moistening rates of the NS we find that this additional surface precipitation seems to be quite robust value of about 15 W m^{-2} (0.5 mm day^{-1}), regardless of the entrainment intensity that would develop in this system and intensity of the radiative forcing.

Comparing the simulation with the drizzle-mimicking, horizontally-uniform forcing (the MFS) with the simulations from Chapter 3 we find that the horizontally-uniform forcing drives the strength of circulation, but lacks the ability to reproduce the cloud field that develops in the full drizzling simulation (the DS). More cumulus-like cloud organization present in the DS is replaced with slightly broken stratocumulus in the MFS. This behavior is a consequence of the inability of the MFS to reproduce the flow organization of the DS: In spite of the similar intensity of the circulation between the MFS and the DS, the horizontally-uniform forcing (MFS) reproduces neither development of large-scales of the flow, nor the updraft-dominated circulation in the cloud layer that are present in the DS.

To the extent that the horizontally-uniform forcing applied to the both thermodynamic budgets reproduced the energetics of the drizzling STBL, the horizontally uniform forcing to the individual thermodynamic budget could be employed to isolate the effect of drizzle on the θ_l budget from its effect on the r_t budget. From this sensitivity study with the LES on a small domain (6.4 km x 6.4 km), we find that the drizzle effect on the moisture budget does not change the energetics of the flow and the strength of circulation. It only affects the cloud structure by preconditioning the downdrafts for the elevation of the local cloud base and eventual removal of the cloudy air. This effect of moisture occurs regardless of whether drizzle is treated in a mean or localized manner. We also find that the drizzle effect on the temperature field, on the other hand, drives the energetics of the flow by reducing the intensity of the circulation, if drizzle is present in the mean sense, and by development of the larger scales in the flow, on top of the weaker circulation, if localized interactions are allowed. This increase in the scales of the flow seems to be a leading source of the changes in the drizzling STBL, which are brought to the full extent of broken clouds by the moisture removal from the cloud field through the effect on the r_t budget.

Given the success of our analysis of the applicability of the MLM to the drizzling STBL, and acknowledging that it addresses very limited range of the heating and moistening rates (only the NS values), we suggest extending it by expanding this parameter space. By exploring the range of the heating and moistening rates, the understanding of the dynamical basis for the cloud transformations would be considerably improved. This could also eventually lead to improved parameterizations of the STBL in the GCMs and could also help constrain the analysis of the impact of aerosols on the cloud structure.

Since one interpretation of the MFS could be a horizontal extension of the MLM forcings, the analysis of this flow indicates what kind of boundary layer develops when the MLM is applied in the conditions where it is not energetically sustainable. Instead of the reorganization of the flow and consequentially cloud field, the boundary layer is forced to only reduce the intensity of circulation but without any feedback on the cloud field and therefore radiative budget. Employing a parameterization that inherently misrepresents the radiative budget has significant implications on our ability to understand the possible feedbacks in the climate system, which furthermore encourages the expansion of the analysis of the parameter space in which the MLM could be utilized in the drizzling conditions. It also suggests that a successful parameterization would be the one that accounts for the internal variability, not only the mean state of the STBL.

Chapter 5

Concluding Remarks

In this dissertation, the mesoscale structure, energetics and dynamics of drizzling stratocumulus are analyzed in terms of the LES representation of the drizzling STBL. To examine the structure, a bulk, two-moment representation of microphysics is introduced into the UCLA LES to facilitate the exploration of the interaction of microphysical, turbulent, cloud dynamical, and radiative processes over large spatial scales using fine spatial discretization. The energetics of the drizzling STBL is explored in terms of the extent to which the canonical view of the STBL (the MLM) could also be applied to the drizzling STBL. To investigate the dynamics, the localized nature of drizzle is removed from the simulations by imposing a horizontally-uniform forcing that corresponds to the domain mean forcing from the simulations with the bulk microphysics, while all other conditions and forcings are kept the same. Furthermore, a contribution of the mean forcing to the individual budgets of moisture and heat is examined, but on smaller spatial scales.

To show that the simulations produce reasonable results, it is first shown that the simulations of precipitating stratocumulus in exceptionally large domains (25.5 km by 25.5 km) with common horizontal (50 m) and fine vertical (5 m near the inversion layer) representation realistically represent many aspects of observed precipitating stratocumulus. These include the tendency of the layer to transition to more cumulus-coupled circulations, with locally elevated cloud tops and patches of anomalous sub-cloud equivalent potential temperature in the vicinity of precipitating clouds. Likewise, it is demonstrated that the simulations also capture the observed tendency for precipitation to be associated with the emergence of a more marked mesoscale circulation and a general reduction in cloudiness.

Having confidence in the representation of the mesoscale structure of drizzling STBL, the underlying dynamics is examined. It is shown that the MLM and decoupling successfully explain the transitions present in the drizzling simulation, as such a boundary layer cannot sustain a well-mixed state. Furthermore, it is demonstrated that the drizzle-mimicking, horizontally-uniform forcing drives the strength of circulation but lacks the ability to reproduce the cloud field that develops in the full drizzling simulation. This change is mostly explained by the drizzle effect on the θ_l budget. The moisture budget seems to be mainly responsible for the preconditioning of the downdrafts for drying the cloudy air.

The cloud field is shown to be strongly influenced by the presence of drizzle. A comparison between non-precipitating and precipitating simulations evinces a strong reduction in cloud albedo from near 75% in the absence of precipitation to values less than 35% in the presence of precipitation (with domain-averaged rates of about 1 mm day^{-1}). As the Twomey effect can account only for about a third of the simulated albedo change, most of this albedo reduction is attributed to changes in the character of the circulation. Furthermore, we find the changes in organization of the flow to be the major source of the albedo reduction, because the simulations with the horizontally uniform forcing reduce the albedo by only 10%, which is only one-fourth of the total reduction.

Although domain-averaged liquid water paths are reduced by half in the presence of drizzle, our simulations are able to maintain a nearly stationary evolution of the cloud in the presence of significant precipitation, in part because the stabilizing effect of precipitation reduces cloud top entrainment and hence entrainment drying. We also find that the change in the flow organization and the change in the intensity of the circulation play equal roles in reducing the liquid water path, because the values for the simulations with horizontally uniform forcing are the average between the non-precipitating and precipitating simulations.

The overall stabilizing effect of precipitation in our simulation is also evident in a slight differentiation between the cloud and sub-cloud layer and a marked increase in the variance of thermodynamic variables. In these simulations, the character of the precipitating layer is best described as cumulus-coupled, or cumulus rising into stratocumulus, in contrast with the more typical, vertically well-mixed, horizontally-uniform stratocumulus circulation that develops in the absence of precipitation. However, our MLM analysis indicates that, for the environmental conditions and forcings of our simulations, a lower intensity of drizzle would not lead to this transition, suggesting caution in the use of specific thresholds for the intensity of drizzle that the STBL can sustain before undergoing through the transition. Furthermore, our simulations suggest that the changes in the cloud organization and the underlying circulation stem mostly from the localized interactions of drizzle and the flow, because the horizontally uniform forcing leads to only slight differentiation between the cloud and subcloud layer and only a minor change in the cloud organization. The analysis of the drizzling simulation also suggests a tendency of the flow to develop mesoscale circulations, which concentrate precipitation within envelopes of upward motion.

A sensitivity study, in which the evaporation of precipitation-size drops is suppressed, shows that the evaporation of precipitation is critical to the observed flow transition. While precipitation rates and liquid water paths are commensurate between precipitating simulations with and without evaporation, the transition of the flow to a cumulus-coupled state is only evident in the case when precipitation-size drops are allowed to evaporate below cloud base. Moreover, the sub-cloud circulations (cold pools) that emerge from such a process appear to play a vital role in shaping the structure of both the sub-cloud layer and regions of new convection.

The analysis of the individual thermodynamic budgets indicates that the energetics and reorganization of the flow toward the larger scales in the drizzling STBL are driven by the θ_l budget. Although the boundary layer stays well mixed when either the moisture budget or the temperature budget are individually impacted, the dynamics of those well mixed boundary layers differs dramatically. In the LES with only the r_t budget altered, the flow is characterized by strong downdrafts, as is the non-precipitating nocturnal STBL. When the θ_l budget is affected, on the other hand, the flow is characterized by updrafts through the whole depth of the STBL and the circulation slows down.

The analysis of the energetics of the flow that evolves as in the NS but drizzles within a given range of intensities at the surface also suggests that one should be careful when relating drizzle to decoupling. There is no evidence of direct association of drizzle with decoupling; instead, we find that a given STBL could actually support a range of drizzle intensities before even developing any positive value of the BIR, and the turbulence within it could even support additional precipitation before fully decoupling. For the heating and moistening rates of the NS we find that this additional surface precipitation seems to be a quite robust value of about 15 W m^{-2} (0.5 mm day^{-1}), regardless of the entrainment intensity that would develop in this system or the intensity of the radiative forcing.

Given the success of our analysis of the applicability of the MLM to the drizzling STBL, and acknowledging that it addresses a very limited range of the heating and moistening rates (only the NS values), we suggest extending it by expanding this parameter space. By exploring the possible range of heating and moistening rates, the understanding of the dynamical basis for the cloud transformations would be considerably improved. This could also eventually lead to improved parameterizations of the STBL in the GCMs and could also help constrain the analysis of the impact of aerosols on the cloud structure.

Since one interpretation of the MFS could be a horizontal extension of the MLM forcings, the analysis of this flow indicates what kind of boundary layer develops when the MLM is applied in the conditions where it is not energetically sustainable. Instead of the reorganization of the flow and consequentially of the cloud field, the boundary layer is forced to only reduce the intensity of circulation but without any feedback on the cloud field and therefore on the radiative budget. Employing a parameterization that inherently misrepresents the radiative budget has significant implications on our ability to understand the possible feedbacks in the climate system, which furthermore encourages the expansion of the analysis of the parameter space in which the MLM could be utilized in drizzling conditions. It also suggests that a successful parameterization would be one that accounts for the internal variability, and not only the mean state, of the STBL.

Appendix A

Divergence and Vorticity Measurement from Aircraft Wind Data

Mean vertical motion plays a vital role in modulating some of the atmospheric processes (*e.g.*, growth of the planetary boundary layer), which has made the mean vertical velocity, $\bar{w}$, a crucial input into most small-scale models, including the LES in this study. Both of these aspects of vertical velocity encouraged observationalists to explore measurement techniques that would acquire its values with the necessary accuracy. Unfortunately, values of $\bar{w}$ in quiescent regions away from deep convection (near the subtropical marine STBL) are generally smaller than 0.01 m s^{-1}, too small to be measured directly by current airborne air-motion sensors. In this appendix, we discuss an alternative approach that is based on the estimates of mean divergence, $\bar{D}$, from the direct airborne measurement of the horizontal wind components. This discussion forms the basis for work published by (Lenschow et al. 2007, hereafter LSS).

A.1. Introduction

For shallow flows, the Boussinesq, or incompressible continuity equation provides a simple relationship between mean vertical velocity and mean divergence:

$$\frac{\partial \bar{w}}{\partial z} = -\frac{\partial \bar{u}}{\partial x} - \frac{\partial \bar{v}}{\partial y} = -\bar{D}, \tag{A.1}$$

where $\bar{u}$ and $\bar{v}$ are the mean eastward and northward wind components, respectively. This relationship sets the foundation for the idea of utilizing horizontal wind measurements to estimate vertical velocity $\bar{w}$. For instance, Brost et al. (1982a), in the study of Sc off the California coast, estimated individual gradients of both wind components from measurements along the 60-km long, crosswind (zonal) linear flight tracks at the south and north sides of the observational area. Gultepe et al. (1990), in the study of cirrus clouds during FIRE, first incorporated circular flight tracks in estimating divergence. Results in both of these studies showed agreement with the expected values for the regions where the measurements took place, but they both lack a discussion and assessment of the possible errors involved in these measurements.

Lenschow et al. (1999, hereafter LKS), in a proposal for utilizing the above relationship for estimating entrainment of free-tropospheric air at the top of the STBL, discussed the feasibility of measuring mesoscale divergence using air motion sensing and applying the divergence theorem onto a circular flight pattern. They indicated that the observations are best carried out in a horizontally homogeneous region well away from complicated terrain, and in regions away from fronts. Furthermore, they argued that the most optimal flight track is a set of circles flown in a Lagrangian frame of reference, with 60 km in diameter. In the analysis, LKS showed the importance of closed-circle flight tracks, and because it is hard to accomplish this when flying in the Lagrangian framework, they suggested a method of data analysis that would account for it. LKS further recognized that both sampling and instrumental errors contribute to the difficulty of estimating divergence, and examined the effects of isolated sources. They discussed how instrumental error, which can originate both in the measurement of airplane velocity and attitude angles (position), and in the measurement of airplane-relative airflow, influences the measurement of the cross-track horizontal velocity component. They suggested that the most limiting factors in the measurement can be a time-dependent drift in the measurement of the true heading and an offset in the sideslip angle. To restrict the time-dependent drift in the true heading, they pointed out that using higher-accuracy GPS (global positioning system) information to provide long-term corrections to the true heading would be essential. For the offset in the sideslip angle, they suggested flight tracks that involve pairs of circles flown in the opposite directions, because they would mostly cancel the effect of the mean offset.

The initial implementation of the LKS technique on wind measurements from NCAR C-130 aircraft during Aerosol Characterization Experiment (ACE-I) were sufficiently encouraging that a flight pattern allowing for the routine measurement of mean divergence and vorticity was incorporated into most flights of the DYCOMS-II field campaign. Data from these flights were analyzed with a newly developed method for calculating mean divergence that is described in A.2.b. The initial divergence results from DYCOMS-II were both encouraging and puzzling. The agreement of the absolute value of the results with the expected value for the region was quite encouraging; however, a negative sign of the results was puzzling and warranted further inspection of the technique. The analysis was guided with two major questions in mind: Given perfect airborne wind measurement, what is the most suitable method for estimating the divergence and vorticity? And, how sensitive are estimates of divergence and vorticity to assumptions in the basic wind measurement techniques?

Searching for the most suitable method, we find that a regression method we developed for calculating divergence and vorticity from the wind data is superior to the line-integral method proposed by LKS. In particular, the new method is not limited to closed-circle flights, and it allows for the time evolution of the flow, which cannot be accounted for by the line-integral method. Analyzing the sensitivities to the assumptions, we diagnose the additional sensitivity of the divergence measurement to the accuracy of the attack angle (a measure of the direction of the incoming airflow, defined in A.3) measurement, which was not recognized in previous work, and which we find does not affect measurements of mean vorticity and mean horizontal wind components. Building on these findings, LSS proposed a correction technique that removes the offset in the attack angle caused by the misalignment of the coordinate systems that measure airplane position and airflow relative to the airplane. LSS also recognized that the line-integral method is more sensitive to the small-scale turbulent motion than the regression method we developed. These combined findings support the possibility of having routine measurement of mean vertical velocity in the future through the measurement of horizontal wind components.

The structure of the manuscript is as follows: Section A.2 reviews the line-integral method and proposes a new method for estimating the mean divergence, $\bar{D}$, and vorticity, $\bar{\zeta}$, that is based on the regression of the measured wind field onto the linear model. In section A.3, an analysis of the sensitivity of divergence and vorticity estimates to airborne wind measurements is presented, which is followed by the summary in section A.4.

A.2. Divergence and Vorticity Estimate Methods

a. *Line-integral Method*

LKS proposed applying the divergence and Stokes' theorems to evaluate $\bar{D}$ and $\bar{\zeta}$ from the airborne measurements of the horizontal wind components as:

$$\bar{D} = \frac{1}{A}\oint v_{\perp} dl \tag{A.2}$$

$$\bar{\zeta} = \frac{1}{A}\oint v_{\|} dl. \tag{A.3}$$

where, $v_{\perp}$ and $v_{\|}$ denote the horizontal wind components locally normal and tangential to the flight track of the element dl, and A is the area circumscribed by the closed flight path. They suggested that the most efficient flight track is a circle because it has the largest enclosed area of any closed curve of a given circumference, and because for the circle completed in a few tens of minutes a turning rate is slow enough that there is no significant reduction in the wind measurement accuracy compared to the straight flight leg.

As LKS noted, the method they proposed assumes that the horizontal velocity field is stationary in the coordinate system of the measurement throughout the measurement period and that the circle is precisely closed. Although flying the closed path in a Lagrangian framework is the closest realization of this assumption, there is a possibility that the mean wind evolves during the time and therefore corrupts the divergence and vorticity estimates. A typical example of actual circular flight paths from DYCOMS-II and the measured horizontal wind components is shown in Fig. A.1. We find that detrending the wind data prior to the application of the line integral method could corrupt the result as well, because the space coordinates are also time dependent. Furthermore,

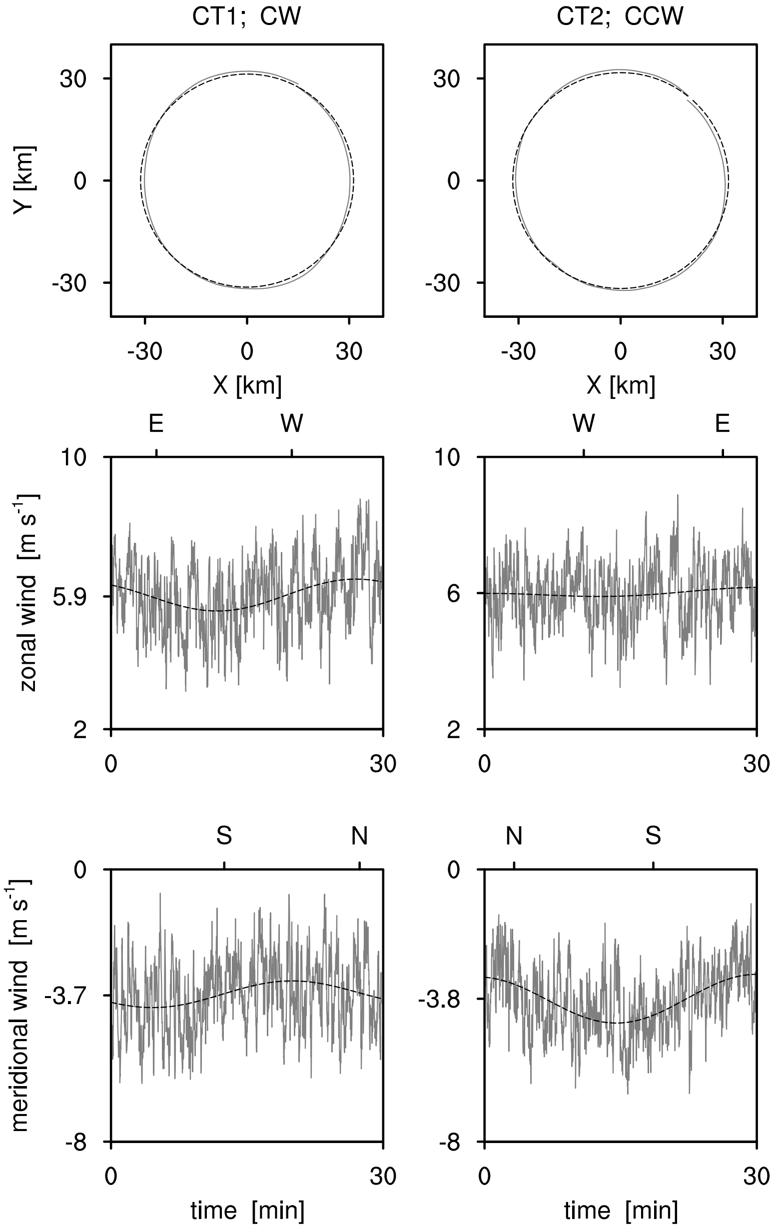

Figure A.1: An example of zonal and meridional winds from two successive circular flight tracks during DYCOMS-II RF07 (July 24, 2001) at about 700 m altitude. Solid lines are measurements and dashed lines are fitted circular flight paths and linear wind fields. From Lenschow et al. (2007).

as LKS note, it would be highly unlikely for the circle to be precisely closed, especially when flying in the Lagrangian framework. Knowing that the integrals in eq. (A.2) and (A.3) do not depend on the shape of the curve, they closed the circle in the calculations by integrating around the circle to the point of minimum distance from the starting point, and therefore minimizing any extraneous contribution to the closed integrals from overlap between the beginning and the end of the circle.

b. *Regression Method*

Recognizing a challenge of the line integral method regarding the path closure and the non-stationarity of the wind field, we propose a method that allows optimal estimates of the wind field derivatives for arbitrary flight tracks and allows for the time dependence of the wind field. This method provides wind derivatives in the Lagrangian framework, given the measured wind field and earth-relative flight track. In particular, winds measured at any point along the flight track can be expanded into a Taylor series with respect to the geographic center of the flight track. Adopting the Lagrangian framework and keeping only the first order terms, a Taylor series expansion of the measured wind is expressed as:

$$\vec{v} = \vec{v}_0 + \frac{\partial \vec{v}}{\partial x}\delta x + \frac{\partial \vec{v}}{\partial y}\delta y + \frac{\partial \vec{v}}{\partial t}\delta t. \tag{A.4}$$

where $\vec{v}_0$ is the mean velocity of the reference point, *i.e.*, the mean wind velocity over the track; δx and δy are the eastward and the northward displacements from the reference point; and δt is the time elapsed from the beginning of the flight leg.

The proposed method does not place restrictions on the shape of the flight track, but both because DYCOMS-II flight tracks were circles advected with the mean wind and for illustration we apply it to the perfect circle of radius R. The displacements δx and δy are simply $\delta x = R \sin \psi_a$ and $\delta y = R \cos \psi_a$, where ψ_a is the airplane azimuth - the angle subtended by the Lagrangian position vector of the airplane and true north. Therefore, expanding eq. (A.4) in scalar form, the zonal, u, and the meridional, v, wind components can be written as:

$$u = u_0 + \frac{\partial u}{\partial x} R \sin \psi_a + \frac{\partial u}{\partial y} R \cos \psi_a + \frac{\partial u}{\partial t} \delta t \tag{A.5}$$

$$v = v_0 + \frac{\partial v}{\partial x} R \sin \psi_a + \frac{\partial v}{\partial y} R \cos \psi_a + \frac{\partial v}{\partial t} \delta t. \tag{A.6}$$

Knowing u, v, R, ψ_a and δt for a particular flight track, one can apply the least square method to these expressions and obtain all the wind derivatives simultaneously, which can then be combined to obtain the mean horizontal divergence and the mean vertical component of vorticity.

Figure A.2 depicts an idealized example conceptualizing the method. The cartoon illustrates a circular flight path of an airplane imposed over zonal wind that has only constant and divergent components ($u = u_0 + \frac{\partial u}{\partial x} \delta x$). For an airplane starting at the north and moving clockwise (CW), the value of measured wind will at first increase to its maximum value achieved at the east, and then decrease to its starting value at the south and minimum value at the west, finally returning to its original value at the north. The measured wind in this idealized case is also depicted in the figure and has the form: $u = u_0 + a \sin \psi_a$. Furthermore, because the x component of the flight track is $\delta x = R \sin \psi_a$, the divergence of the wind is directly related to the amplitude of the sinusoidal signal in the measured wind, a, as $\frac{\partial u}{\partial x} = \frac{a}{R}$, and therefore with known amplitude a and circle radius R one can calculate the divergence of the measured wind field.

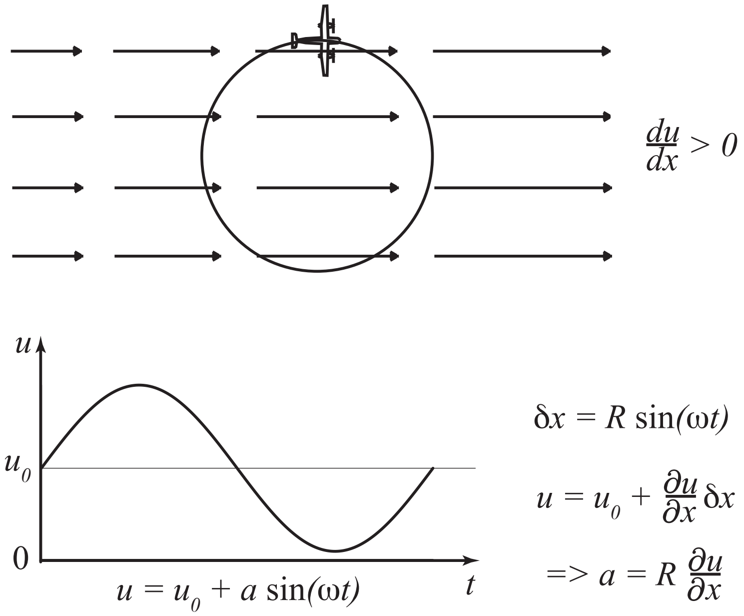

Figure A.2: A schematic illustration of the regression method applied to a circular flight track. Following Lenschow et al. (2007).

In practice, the airplane is flown with approximately constant turn rate, ω. Because this leads to a linear relationship between the airplane azimuth and elapsed time ($\psi_a = \omega \delta t + \psi_{a0}$, where ψ_{a0} is the airplane azimuth at the beginning of the flight leg), the components of the desired divergence and vorticity actually become the coefficients multiplying linearly independent functions of time in Eqs. (A.5) and (A.6). This time dependence of the airplane azimuth is a key reason for applying a method that allows for non-stationarity of the wind field.

Finally, to estimate R, ω and ψ_{a0} for each flight leg, it is necessary to first determine the flight track in the Lagrangian framework. This flight track can then be used to obtain the parameters describing the approximate circular flight track (radius R and the coordinates of the circle center) by applying circular regression to find the best fitting circle for a given track. The circle with these parameters is finally used to obtain the azimuth data that can be used to determine ω and ψ_0 by applying another least square fit, which closes the system by determining the last unknown variables.

Because the non-stationarity of the wind is directly incorporated into the regression method for estimating wind derivatives, and because the least-square approach applied at multiple instances in this method does not depend on the closure of the flight track, it can be shown that the regression method is an improvement to the LKS method. In addition, LSS show that the regression method has the additional advantage over the line-integral method because it reduces sampling error due to the turbulent nature of the airflow. Their analysis is based on the expression for the random error variance of the estimate of the trend (gradient) of a variable given by Bevington (1969) and indicates that the sampling error from the line-integral method is roughly 4–6 times that from the regression method. Regardless of the method, though, the accuracy of the wind measurements puts an important restriction on the divergence estimate, and in the following section we discuss the sources of these sensitivities.

A.3. Sensitivity of Divergence and Vorticity Measurement to Airborne Wind Measurement

Understanding airborne wind measurement is crucial for the analysis of their effects on the sensitivity of divergence and vorticity estimates. As a starting point of the analysis, the technique of wind measurement from air-motion sensing instruments is introduced. In particular, definitions of the measured variables and the equations utilizing these for calculating wind components, known as Lenschow equations (Lenschow 1986), are reviewed. This introduction is followed by analysis of the systematic errors

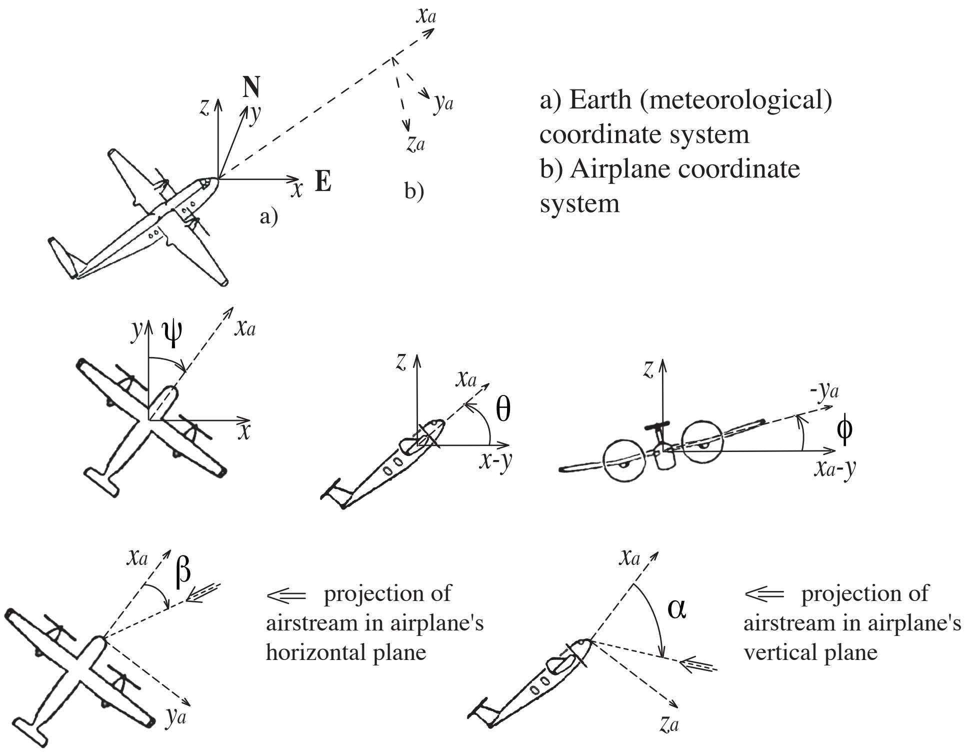

Figure A.3: Schematic showing the attitude angles and axes used to define the airplane coordinate systems. ψ, θ and ϕ are the true heading, pitch and roll attitude angles, respectively, while α and β are the attack and sideslip air flow angles, respectively. Following Lenschow et al. (2007).

in divergence and vorticity caused by the offsets in the measured airflow angles.

To be available for the wind measurements, the NCAR aircraft C-130, which was utilized during DYCOMS-II, is equipped with the IRS (inertial reference system), which measures the position and velocity of the vehicle, GPS that measures airplane position with higher accuracy than the INS, and the RAMS (radome air-motion system) that measures the airflow relative to the vehicle. In particular, IRS measures the aircraft attitude in terms of the three angles: the true heading, ψ, the pitch, θ, and the roll, ϕ, while the velocity is measured in the geographic coordinate system in terms of zonal, u_p, meridional, v_p, and vertical, w_p, airplane velocity. More precisely, IRS measures airplane accelerations in the three directions of rotation. These accelerations are then integrated to obtain the desired quantities. During the integration, GPS-measured aircraft position is incorporated to acquire high accuracy. RAMS, on the other hand, relies on the airplane geometry when measuring the true airspeed (intensity of the airstream velocity), U_a and two airflow angles: the attack, α, and the sideslip, β, which leaves some space for uncertainties.

Figure A.3 illustrates the measured angles, while their definitions are as follows: α, the attack angle, is the angle of the airstream with respect to the aircraft in the aircraft's vertical plane, being positive in the downward direction; β, the sideslip angle, is the angle of the airstream with respect to the aircraft in the aircraft's horizontal plane, with the clockwise (looking from above) positive rotation; ψ, the true heading, measures rotation about the local earth vertical coordinate axis, and is positive in the clockwise direction (looking from above); θ, the pitch angle, measures the rotation about the airplane's latitudinal axis, and is positive when the airplane's nose is lifted; and ϕ, the roll angle, measures the rotation about the airplane's longitudinal axis, and is positive when the airplane's left wing is lifted. ψ is equal to zero when the airplane faces north, while θ and ϕ are equal to zero when the airplane's horizontal axes are parallel to the local earth horizontal plane.

Because the airflow is measured in the aircraft coordinate system, it has to be transfered to the local earth coordinate system before it can be summed with the aircraft ground velocity to provide the required wind measurement. In addition, because the IRS and RAMS are not collocated, but stand along the longitudinal axis of the airplane with a distance L, there is also a need for the correction of the RAMS rotation about the INS. These coordinate transformations, predefined by the design of the INS* and small distance between the IRS and the RAMS, are formalized by Lenschow (1986) into the Lenschow equations:

$$\begin{aligned} u = -U_a D_a^{-1} [& \sin\psi\cos\theta + \tan\beta(\cos\psi\cos\phi + \sin\psi\sin\theta\sin\phi) + \\ & + \tan\alpha(-\cos\psi\sin\phi + \sin\psi\sin\theta\cos\phi)] + \\ & + u_p - L(\dot{\theta}\sin\psi\sin\theta - \dot{\psi}\cos\psi\cos\theta) \end{aligned} \tag{A.7}$$

$$\begin{aligned} v = -U_a D_a^{-1} [& \cos\psi\cos\theta + \tan\beta(-\sin\psi\cos\phi + \cos\psi\sin\theta\sin\phi) + \\ & + \tan\alpha(\sin\psi\sin\phi + \cos\psi\sin\theta\cos\phi)] + \\ & + v_p - L(\dot{\theta}\cos\psi\sin\theta + \dot{\psi}\sin\psi\cos\theta) \end{aligned} \tag{A.8}$$

$$w = -U_a D_a^{-1}[\sin\theta - \tan\beta\cos\theta\sin\phi - \tan\alpha\cos\theta\cos\phi] + w_p + L\dot{\theta}\cos\theta. \tag{A.9}$$

Here, $D_a = \sqrt{1 + \tan^2\alpha + \tan^2\beta}$ is the direction cosine of the airstream relative to the airplane's longitudinal axis.

The Lenschow equations provide a framework suitable for the error propagation analysis, where the offsets in the measured angles can be related to the biases in the wind components. One can actually go a step further and do the error propagation analysis between the biases in the measured angles and the biases in the estimates of $\bar{D}$ and $\bar{\zeta}$. To do so, recall that the wind velocity normal to the flight track can be expressed as:

$$v_\perp = -u\cos\psi + v\sin\psi, \tag{A.10}$$

---

[*] The coordinate transformation from the aircraft to the local earth coordinates is as follows: first, airflow velocity is rotated for ϕ, followed by the rotation for θ and then for ψ, and lastly by the angle π about the zonal earth coordinate when it coincides with the airplane longitudinal axis (airplane faces the east).

and, similarly, the wind velocity tangential to the flight track:

$$v_{\parallel} = u \sin\psi + v \cos\psi. \tag{A.11}$$

Furthermore, taking into account the LKS suggestion to calculate mean divergence by averaging it from two consecutive flight tracks flown at the same height in the opposite direction, one can expand (A.2) and (A.3) to the average of two integrals. To simplify the analysis, let us assume that the airplane starts both flight tracks at the same point, and let that particular point be on the West side of the circle so that the clockwise circle (CW) starts with $\psi_0 = 0$ and the counter-clockwise circle (CCW) starts with $\psi_0 = -\pi$. Then:

$$\bar{D} = \frac{1}{2}\frac{R}{A}\left(\int_0^{2\pi} v_{\perp}(CW)d\psi + \int_{-\pi}^{-3\pi} v_{\perp}(CCW)d\psi\right) \tag{A.12}$$

and

$$\bar{\zeta} = \frac{1}{2}\frac{R}{A}\left(\int_0^{2\pi} v_{\parallel}(CW)d\psi + \int_{-\pi}^{-3\pi} v_{\parallel}(CCW)d\psi\right), \tag{A.13}$$

where $A = R^2\pi$.

Focusing only on the airflow angles, the largest sources of uncertainties in the airborne wind measurements, and keeping in mind that during circular flight tracks (unlike during the straight leveled flight tracks) the airplane has to roll, one can combine Eqs. (A.7), (A.8), (A.10) and (A.11) to isolate the terms of interest:

$$v_{\perp} \propto -U_a D_a^{-1}[-\tan\beta\cos\phi + \tan\alpha\sin\phi] \tag{A.14}$$

and

$$v_{\parallel} \propto -U_a D_a^{-1}[\tan\beta\sin\theta\sin\phi + \tan\alpha\sin\theta\cos\phi]. \tag{A.15}$$

Furthermore, noting that the airplane experiences a positive (negative) roll when flying CW (CCW), assuming that the airplane has the same roll intensity ϕ for both directions, and denoting the negative sign for the CCW circle as $-\phi$, equations (A.12) and

(A.14) can be combined into:

$$\begin{aligned}\bar{D} \propto & \frac{-U_a D_a^{-1} R}{2A}\left\{\int_0^{2\pi}[-\tan\beta\cos\phi + \tan\alpha\sin\phi]d\psi + \right.\\ & \left. + \int_{-\pi}^{-3\pi}[-\tan\beta\cos(-\phi) + \tan\alpha\sin(-\phi)]d\psi\right\} = \\ & = \frac{-2U_a D_a^{-1}}{R}\tan\alpha\sin\phi. \end{aligned} \tag{A.16}$$

Similarly, equations (A.13) and (A.15) lead to the expression for mean vorticity:

$$\begin{aligned}\bar{\zeta} \propto & \frac{-U_a D_a^{-1} R}{2A}\left\{\int_0^{2\pi}[\tan\beta\sin\theta\sin\phi + \tan\alpha\sin\theta\cos\phi]d\psi + \right.\\ & \left. + \int_{-\pi}^{-3\pi}[\tan\beta\sin\theta\sin(-\phi) + \tan\alpha\sin\theta\cos(-\phi)]d\psi\right\} = \\ & = \frac{2U_a D_a^{-1}}{R}\tan\beta\sin\theta\sin\phi. \end{aligned} \tag{A.17}$$

Equations (A.16) and (A.17) are the basis for estimating systematic errors in the mean divergence and vorticity estimates, $\Delta\bar{D}$ and $\Delta\bar{\zeta}$, due to the offsets in airflow angles, $\Delta\alpha$ and $\Delta\beta$. Taking into account the constraint that the airplane can measure wind only when the airflow angles are small (less than 5°)[†], it becomes clear that the offsets in these angles are also small, which allows for simplification of the equations based on the properties of trigonometric functions that $\tan(\alpha + \Delta\alpha) \simeq \tan\alpha + \Delta\alpha$, and similarly for small β. In addition, as LKS calculated, for a 30-min flight time around the circle, roll angle has a value of only $\simeq 2°$, which we denote as $\delta\phi$, and which also allows for the simplification of the equations by $\sin\delta\phi \simeq \delta\phi$. Calculating the systematic errors in mean divergence as $\Delta\bar{D}(\Delta\alpha, \Delta\beta) = \bar{D}(\alpha + \Delta\alpha, \beta + \Delta\beta) - \bar{D}(\alpha, \beta)$ and similarly for vorticity, $\Delta\bar{\zeta}$, equations (A.16) and (A.17) lead to:

$$\Delta\bar{D}(\Delta\alpha, \Delta\beta) \simeq \frac{-2U_a D_a^{-1}}{R}\delta\phi\,\Delta\alpha \tag{A.18}$$

[†] The constraint of small airflow angles originates in the construction of the RAMS that restricts the range of values of the airflow angles that the RAMS can accurately measure.

and

$$\Delta\bar{\zeta}(\Delta\alpha, \Delta\beta) \simeq \frac{2U_a D_a^{-1}}{R} \sin\theta \, \delta\phi \, \Delta\beta, \tag{A.19}$$

This analysis confirms the suggestion of LKS that the systematic error in the wind measurements due to the offset in sideslip angle can be removed from the divergence estimates by averaging the results from two circles flown at the same level with opposing directions. In addition, this analysis points out that for circular flight tracks, due to the existence of roll angle, the offset in the attack angle becomes a source of systematic error in the divergence measurements that is not so obvious how to account for. On the other hand, because $\sin\theta$ modulates the systematic error in mean vorticity measurements, one can see that the value of the error is significantly reduced when compared to the systematic error in the mean divergence. Keeping in mind that the mean vorticity is typically an order of magnitude stronger than the mean divergence, this systematic error in mean vorticity becomes negligible.

To illustrate the biases in the mean divergence and vorticity estimates due to the offset in the attack angle, which we isolated in our analysis, let us examine an idealized case of an airplane that flies along a circular flight track in a motionless atmosphere, and in which RAMS and IRS are stationed at the same location. If there were no biases in the measured angles, the airplane would measure an airplane-relative airflow velocity that would be equal to, but with the opposite sign of, the airplane ground velocity. In the case of positive bias in the angle of attack, the measured airplane-relative airflow velocity would have both vertical and horizontal spurious components. The spurious vertical component would be upward, while the intensity of the spurious horizontal component would be stronger than the airplane ground velocity. When transformed to the earth-relative vector, the vertical component would project onto the spurious convergent wind component, regardless of whether the airplane flew in a CW or CCW circle, while the horizontal component would project on the spurious rotational wind component, which would be positive (cyclonic) for a CCW and negative (anticyclonic) for a CW circle. When averaging the divergence and vorticity estimates over the two circular flight paths, the spurious convergent wind components would add and give a spurious divergence estimate, while the spurious rotational components would cancel to give an accurate vorticity estimate.

To quantify the bias in the estimate of the mean divergence due to the offset in the attack angle, let us assume $\Delta\alpha = 1^\circ$ and use the values for the true airspeed, circle radius and airplane roll as in LKS, namely U_a = 100 m s^{-1}, R = 29 km and $\delta\phi = 2^\circ$. With these values, eq. (A.18) leads to $\Delta\bar{D} = -4 \times 10^{-6}$ s^{-1}. Because 4×10^{-6} s^{-1} is approximately the value that divergence is expected to have in the Subtropical Stratocumulus region, the same value for $\Delta\bar{D}$ indicates a high sensitivity of the divergence measurement to the offsets in the attack angle. In addition, a negative sign of $\Delta\bar{D}$ indicates that the spurious sign in the initial results of the DYCOMS-II estimates of divergence could be related to the offset in the attack angle. From this analysis, one could argue that if the mean divergence is expected to be measured routinely, this high value of the bias in the mean divergence due to the offset in the attack angle puts quite a high demand on the accuracy of the measurement of the airflow angles.

Because the measurement of the attack angle is not a direct process, but instead relies on the measurement of static and dynamic air pressures, a higher accuracy of the measurement of the attack angle also involves more accurate calibration of these pressures. A DYCOMS-II wind data set that has been recalibrated by incorporating a correction to the static pressure based on a more accurate inflight calibration using a trailing cone pressure calibration technique (Brown 1988) shows improvement in the divergence estimates. Using the regression method outlined in section A.2.b, these recalibrated wind data result in $\bar{D} = 5.2 \times 10^{-6}\ \mathrm{s}^{-1}$. This is very encouraging in terms of both intensity and sign, especially when compared to the initial puzzling estimate of divergence of $-8 \times 10^{-6}\ \mathrm{s}^{-1}$. These results imply that, although the primary motivation for the recalibration was the discovery that momentum flux measurements were slightly heading-dependent, which is independent from our analysis, the more accurate calibration of static pressure has led to a great improvement of the wind measurement.

The impact of small biases in the measurement of the attack angle discussed here was not previously appreciated, but highlights the need for high accuracy in the absolute angle of attack. LSS, who started with these recalibrated data, further build on our findings and describe additional improvement of the measurement technique by correcting for the possible residual misalignments between the IRS and RAMS coordinates. In particular, they reflect on the in-flight calibration maneuvers that are performed at high altitudes, where the mean vertical velocity is assumed to be zero. This assumption is then used as a constraint for estimating offsets in the angles in the vertical plane. Because for measurements of the mean wind in straight and level flight it makes no difference whether the offset is introduced in either θ or α, this constraint is traditionally satisfied by introducing an offset in θ. LSS, however, suggest that such a procedure is problematic for a turning aircraft, for which the absolute value of the attack angle becomes important. They argue that because $\bar{w}$ is the component of the flow perpendicular to the geopotential, which is the reference for θ, and because θ is continuously measured very accurately by the IRS, there is no basis for introducing the offset in θ. Instead, the offset estimated during the maneuver should be incorporated in α, which would lead the α measurement to be aligned to the local horizontal, and thus define an absolute α.

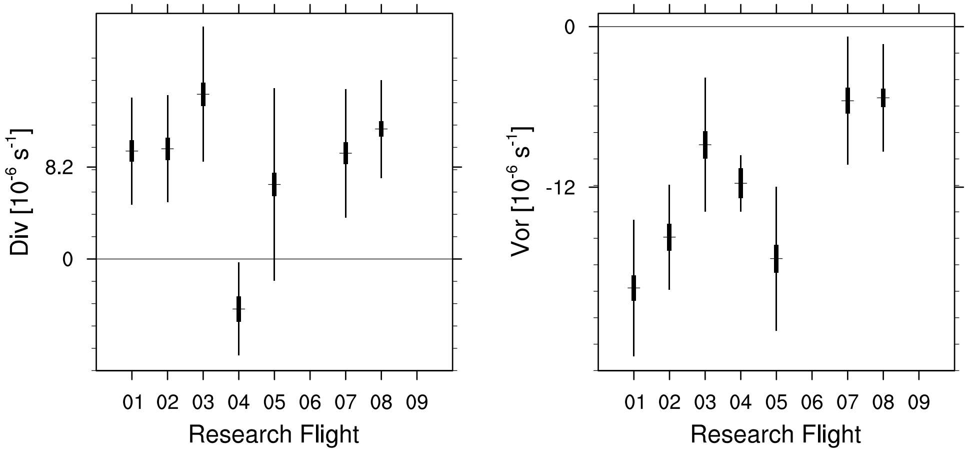

Figure A.4: Divergence (left) and vorticity (right) for seven DYCOMS-II flights. The thick vertical bar is twice the random error estimated by Lenschow et al. (2007) and the thin vertical bar is twice the standard deviation of the mean from the measurements. From Lenschow et al. (2007).

Figure A.4 depicts the estimates of mean divergence and vorticity for each fight of DYCOMS-II with included corrections suggested by LSS. These are calculated from the data after removing a bias from the sideslip angle by equating estimates from CW and CCW circles. The mean divergence over all flights is estimated to be 8.2×10^{-6} s^{-1}, while the mean vorticity is estimated to be -12×10^{-6} s^{-1}, which is in general agreement with the expected values. As discussed by LSS, these values for $\bar{D}$ are somewhat high when compared with other estimates from the literature (that are for the same region and time period). However, because of the lack of error analysis for the other estimates, it is still inconclusive what the exact value of mean divergence during DYCOMS-II is. Figure A.4 also depicts the random error due to the limited sampling (discussed by LSS) by thick vertical bars and the measured standard deviation of the estimates by thin vertical bars. These bars indicate that the estimated random error is significantly smaller than the measured standard deviation of the estimates. LSS therefore suggest that DYCOMS-II measurements are not limited by the effects of small-scale turbulent wind fluctuations but by real day-to-day and level-to-level variability in the mean divergence and vorticity. That is, the standard deviation of the estimates for each flight would be an overly conservative measure of the random error since the estimates include real temporal and spatial variability, which further challenges our attempts to provide the routine measurement of mean vertical velocity and warrants careful interpretation of results.

A.4. Summary

A possibility for the routine measurement of mean vertical velocity is revisited. In particular, a new improved method has been developed for estimating mean divergence, which through continuity allows for the estimate of mean vertical velocity. The improvements in this novel method, which we call the regression method, follow from the application of the least-square fit to the wind data. They include independence from the closure of the flight track and the ability to address the time evolution of the wind field. In addition, LSS showed that this new method is more suitable for the measurement of mean divergence in the turbulent environment because it is less sensitive to the small scale variability of the wind.

Given the initial negative estimates of DYCOMS-II divergence even when using the regression method, the sensitivity of the mean divergence and vorticity estimates to the assumptions in the wind measurement techniques is also revisited. The previously not appreciated sensitivity to the offset in the attack angle is isolated and described. This sensitivity arises in the measurements along the circular flight path due to the airplane roll, which projects spurious airplane-relative vertical airflow velocity onto the spurious convergent earth-relative wind component. The analysis shows that an offset of only 1° in the attack angle leads to a bias of -4×10^{-6} s^{-1} in the divergence estimate, which is comparable to (but with the opposite sign of) the values expected in the Stratocumulus climate regime and emphasizes the need for high accuracy in the measurement of the angle of attack. A more precise calibration of the static pressure (Brown 1988), which was initiated by the problems with the momentum flux measurements, has shown to improve the divergence results as well because it directly influences the accuracy of the attack angle measurement. More precisely, the use of these recalibrated data seems to be necessary to get reasonable estimates of divergence.

The newly developed regression method for estimating divergence and vorticity (outlined in A.2.b), as well as the recognition of yet another challenge for obtaining accurate airborne wind measurements during the circular flight paths (analyzed in A.3) provide a foundation for the LSS study. In addition to presenting the method and the challenge, starting from the recalibrated wind data, they offer a procedure to account for the error. In particular, they recognize that the practice of assigning the bias to the pitch angle during the in-flight calibration maneuvers leads to a spurious offset in the attack angle that propagates into the divergence measurements. After removing this spurious offset from the recalibrated DYCOMS-II data set, they calculated flight-mean divergence and vorticity for all flights and estimated the random error in mean divergence and vorticity estimates (Fig. A.4). In their analysis of resulting divergence, from the comparison of the random error and the standard deviation of the estimates for each flight, they concluded that the real temporal and spatial variability causes the standard deviation of the estimates for each flight to be an overly conservative measure of the random error. Furthermore, from the comparison of these *in situ* results with the other results published in the literature, LSS concluded that there is general agreement between the various estimates, with the values they calculated being somewhat high for the mean divergence.

The results presented here together with their further improvement by LSS indicate that the routine airborne measurement of mean vertical velocity is feasible in the Stratocumulus region. However, this routine measurement requires high accuracy of the wind measurements, especially in terms of the accuracy of the airplane-relative airflow measurements. Our analysis shows that the current calibration techniques (that provide the original DYCOMS-II wind data) lack the necessary accuracy, but that the calibration of static pressure described in Brown (1988) and the additional correction for the attack angle suggested by LSS could improve the quality of the airborne wind measurements to allow for the desired routine mean divergence measurement. With this indirect routine mean vertical velocity measurement we could eventually focus on real day-to-day and level-to-level variability of the air motion.

Appendix B

Equations

B.1. Equations for LES

UCLA LES solves the Ogura-Phillips anelastic equations that exclude sound waves, but represent all other types of motion in the atmosphere. In particular, it solves for the three components of velocity, $\bar{u}_i$, and any number of scalars, $\bar{\phi}$:

$$\frac{\partial \bar{u}_i}{\partial t} = -\bar{u}_j \frac{\partial \bar{u}_i}{\partial x_j} - c_p \Theta_0 \frac{\partial \bar{\pi}}{\partial x_i} + \frac{g \bar{\theta}_v''}{\theta_0} \delta_{i3} + f_k(\bar{u}_j - u_{jg})\epsilon_{ijk} + \frac{1}{\rho_0} \frac{\partial (\rho_0 \tau_{ij})}{\partial x_j}, \qquad \text{(B.1)}$$

$$\frac{\partial \bar{\phi}}{\partial t} = -\bar{u}_j \frac{\partial \bar{\phi}}{\partial x_j} + \frac{1}{\rho_0} \frac{\partial (\rho_0 \gamma_{\phi j})}{\partial x_j} + \frac{\partial F_\phi}{\partial x_j} \delta_{j3}, \qquad \text{(B.2)}$$

while pressure is diagnosed at each time step by solving the Poisson equation for the Exner function (the non-dimnesionalized pressure, $\pi = (p/p_{00})^{R/c_p} = T/\theta$):

$$\begin{aligned} \frac{\partial}{\partial x_i}\left(\rho_0 \frac{\partial \bar{\pi}}{\partial x_i}\right) = \frac{1}{c_p \Theta_0} \frac{\partial}{\partial x_i} \\ \left(-\rho_0 \bar{u}_j \frac{\partial \bar{u}_i}{\partial x_j} + \frac{\rho_0 g \bar{\theta}_v''}{\theta_0} \delta_{i3} + \rho_0 f_k (\bar{u}_j - u_{jg})\epsilon_{ijk} + \frac{\partial (\rho_0 \tau_{ij})}{\partial x_j}\right). \end{aligned} \qquad \text{(B.3)}$$

The Poisson equation for π follows from the momentum and continuity ($\frac{\partial(\rho_0 \bar{u}_j)}{\partial x_j} = 0$) equations. UCLA LES conforms to the First Law of thermodynamics, which is represented by Eq. (B.2) when applied to the liquid-water potential temperature defined as $\theta_l = \theta \exp(-\frac{L_v r_l}{c_p T})$.

In the Eqs. (B.1) - (B.3), $\theta_v = \theta(1+(R_v/R_d-1)r_t-(R_v/R_d)r_l)$ is virtual potential temperature that characterizes the buoyancy, with θ being potential temperature, and r_t and r_l being total-water and liquid-water mixing ratios, respectively. The reference state, given by $(p_0, \theta_0, \rho_0, u_g, v_g)$, is chosen to be in the hydrostatic and geostrophic balances and to satisfy the ideal gas law for a dry atmosphere. The reference state is height dependent, except for Θ_0 in the hydrostatic equation $\frac{d\pi_0}{dz} = -\frac{g}{c_p\Theta_0}$ that is constant. Superscript $''$ denotes the thermodynamic perturbations from the horizontal average. The sub-filter scale contributions to the momentum ($\tau_{ij} \doteq \overline{u_i u_j} - \bar{u}_i \bar{u}_j$) and the scalar ($\gamma_{\phi j} \doteq \overline{u_j \phi} - \bar{u}_j \bar{\phi}$) fields, as well as diabatic fluxes, F_ϕ, are parameterized in a manner described below. The remaining symbols have a common meaning: c_p is isobaric specific heat, R_d is a gas constant for dry air, R_v is a gas constant for water vapor, L_v is enthalpy of vaporization, T is the absolute temperature, g is gravitational acceleration, $f_k = (0, 0, f)$ is the Coriolis parameter, δ_{ij} is the Kronecker delta, and ϵ_{ijk} is the Levi-Civita symbol.

Sub-filter fluxes are modeled using the Smagorinsky model, which an eddy viscosity model:

$$\tau_{ij} = -\rho_0 K_m \, D_{ij}, \tag{B.4}$$

$$\gamma_{\phi j} = -P_r^{-1} \, K_m \, \frac{\partial \bar{\phi}}{\partial x_j}. \tag{B.5}$$

Here K_m is eddy viscosity, $D_{ij} = \frac{\partial \bar{u}_i}{\partial x_j} + \frac{\partial \bar{u}_j}{\partial x_i}$ is resolved deformation tensor and P_r is eddy Prandtl number. In the model, eddy viscosity is assumed to be proportional to the characteristic turbulent velocity and to the mixing length scale that is modified to include the effects of the stabilization:

$$K_m = (C_s l)^2 \, S \, \sqrt{1 - P_r^{-1} R_i}. \tag{B.6}$$

Here, $R_i = \frac{S^2}{N^2}$ is the Richardson number, S is the strain rate ($S^2 \doteq \frac{\partial \bar{u}_i}{\partial x_j} D_{ij}$), N is the Brunt-Vaisala frequency ($N^2 = \frac{g}{\Theta_0}\frac{\partial \bar{\theta}_v}{\partial z}$), C_s is the Smagorinsky constant, and l is mixing length ($l^2 = (\Delta x \Delta y \Delta z)^{-2/3} + (z\kappa/C_s)^2$), with $\kappa = 0.35$ being the von Karman constant.

Diabatic fluxes include the radiative and precipitation fluxes, F_r and F_d respectively, and affect the evolution of θ_l and r_t through their vertical divergence:

$$\frac{\partial F_{\theta_l}}{\partial z} = \frac{\partial F_r}{\partial z} - \frac{L}{c_p}\frac{\theta_l}{T}\frac{\partial F_d}{\partial z} \tag{B.7}$$

$$\frac{\partial F_{r_t}}{\partial z} = \frac{\partial F_d}{\partial z}. \tag{B.8}$$

To reduce computational costs, both diabatic fluxes are parameterized with simplified models. In particular, radiative forcing is parameterized with a simple model of the net long-wave radiative flux that has been developed by Stevens et al. (2005a), who showed that the model reasonably approximates radiative fluxes calculated by the computationally-expensive δ-four stream radiative-transfer code developed by Fu and Liou (1993). It is a diagnostic model in which the three terms represent the effects of cloud top cooling, cloud base warming, and cooling in the free troposphere just above the cloud top:

$$F_r(x,y,z,t) = F_0 e^{-Q(z,\infty)} + F_1 e^{-Q(0,z)} + \rho_i c_p D \alpha_z \left[\frac{(z-z_i)^{4/3}}{4} + z_i (z-z_i)^{1/3}\right], \tag{B.9}$$

where

$$Q(a,b) = \kappa \int_a^b \rho r_l dz. \tag{B.10}$$

Also, ρ_i is the air density just below cloud top, D is the large scale divergence, and F_0, F_1, α_z and κ are the tuning parameters, adjusted in a manner that the simple model fits the profile from the full model for a given initial state. The horizontal and temporal dependence of F_r follows from the spatio-temporal variability in both r_l and z_i (inversion height).

Drizzle fluxes are introduced with a simple model that follows Seifert and Beheng (2001, 2006) and is described in Section 2.2 with detailed expressions for microphysical processes, sedimentation and evaporation presented in the following section.

B.2. Bulk Rain Formation

a. *Microphysical Processes*

Microphysical processes introduced to the UCLA LES follow Seifert and Beheng (2001). In particular, intra- and interspecies interactions of cloud droplets and drizzle drops are modeled as:[*]

Auto-conversion Drizzle formation occurs through intraspecies interaction of cloud droplets, i.e. by collision and coalescence of cloud droplets. It augments both the mass and number of drizzle drops and is modeled as:

$$C_{cc}(r_c, r_p; m^*, n_c) = \frac{k_c}{20m^*}\frac{(\nu_c+2)(\nu_c+4)}{(\nu_c+1)^2}r_c^2 m_c^2\left(1+\frac{\Phi_{au}}{(1+\tau)^2}\right)\rho_0. \qquad \text{(B.11)}$$

Here, $m^* = 6.5 \cdot 10^{-11}$ kg is a separation mass between cloud droplets and drizzle drops that we chose to agree with the observations (vanZanten et al. 2005), while $m_c = r_c/n_c$ is the mean mass of cloud droplets. Furthermore, $k_c = 9.44 \cdot 10^9$ m^3

---

[*] UCLA LES is defined in terms of mixing ratios, while the work of Seifert and Beheng (2001, 2006) is based on the concentrations. To derive equations from Seifert and Beheng (2001, 2006), one needs to multiply the equations here with the air density ρ and follow with transformation of all the relevant terms.

kg^{-2} s^{-1} is a cloud-droplet related coefficient in Long kernel, $\nu_c = 0$ corresponds to the Gamma distributed cloud droplets, $\tau = 1 - \frac{r_c}{r_c+r_p}$, $\Phi_{au} = k_1\tau^{k_2}(1-\tau^{k_2})^3$, where $k_1 = 600$ and $k_2 = 0.68$, and ρ_0 is air density at the surface.

Accretion Growth of drizzle drops through interspecies interaction of drizzle drops and cloud droplets, i.e. by collection of cloud droplets, increases the mean mass of drizzle and is modeled following:

$$C_{pc}(r_c, r_p) = k_r r_c r_p \Phi_{ac}\sqrt{\rho_0\rho}. \tag{B.12}$$

Here, $k_r = 5.78$ m^3 kg^{-1} s^{-1} is a drizzle-drop related coefficient in Long kernel, $\Phi_{ac} = (\frac{\tau}{\tau+k_1})^4$, with $k_1 = 5\cdot 10^{-4}$ and ρ is air density.

Self-collection Growth of drizzle drops through intraspecies interaction of drizzle drops, i.e. by collection of smaller drizzle drops by the larger ones, reduces the number of drizzle drops and is modeled as:

$$C_{pp}(r_p, n_p) = -k_r n_p r_p \sqrt{\rho_0\rho}. \tag{B.13}$$

b. *Sedimentation*

Sedimentation of drizzle drops introduced to the UCLA LES is in the accordance with what Seifert and Beheng (2001) used in their study (personal communication). In particular, mass- and number-weighted mean fall velocities are modeled following:

$$v_r(r_p, n_p) = 4a(1-(1+bD_p)^{-5})D_p, \tag{B.14}$$

$$v_n(r_p, n_p) = a(1-(1+bD_p)^{-2})D_p. \tag{B.15}$$

Here, $a = 4 \cdot 10^3$ m s^{-1}, $b = 12 \cdot 10^3$ m^{-1} and

$$D_p = (6r_p/(\pi \rho_l n_p))^{1/3}$$

is a drizzle-drop diameter. The sedimentation fluxes are then calculated using the upwind Eulerian scheme for both mass and number mixing ratios. However, only the sedimentation flux of mass mixing ratio of drizzle affects the evolution of the thermodynamic properties of the air.

Cloud-droplet sedimentation flux in the UCLA LES is based on the mass weighted mean fall velocities and is modeled as:

$$F_c(r_c, n_c) = c\,(3/(4\pi \rho_l n_c))^{2/3}\,\rho\, r_c^{5/3}\, exp(5ln^2\sigma_g), \tag{B.16}$$

where $c = 1.19 \cdot 10^8$ m^{-1} s^{-1} (Rogers and Yau 1989), σ_g is a geometric standard deviation, and ρ_l is the liquid-water density.

c. *Evaporation*

Evaporation of drizzle drops introduced to the UCLA LES is modeled following Seifert and Beheng (2006), but neglecting the ventilation effect:

$$E(r_p, r_v, r_s, n_p) = 2\pi G S n_p D_p. \tag{B.17}$$

Here, $G = ((\rho r_s D_v)^{-1} + \frac{L}{K_T T}(\frac{L}{R_v T} - 1))^{-1}$, with $K_T = 2.5 \cdot 10^{-2}$ J s^{-1} K^{-1} m^{-1} being heat conductivity, $D_v = 3 \cdot 10^{-5}$ m^2 s^{-1} the diffusivity of water vapor, $R_v = 461$ J kg^{-1} K^{-1} the water vapor gas constant and $S = r_v/r_s - 1$ the supersaturation. Drizzle drops are not allowed to grow through condensation, but instead condensation produces new, or increases mass of existing cloud droplets.

Appendix C

Notation

Table C.1: Abbreviations

ACE-I	Aerosol Characterization Experiment
BL	boundary layer
CCN	cloud condensation nuclei
CCW	counter clockwise
CTEI	cloud top entrainment instability
CW	clockwise
DYCOMS-II	the second dynamics and chemistry of marine stratocumulus field study
DCBL	dry convective boundary layer
DS	drizzling simulation
DWES	drizzling without evaporation simulation
EPIC	the east pacific investigation of climate
GEWEX	global energy and water cycle experiment
GPS	global positioning system
GCSS	GEWEX cloud system study
INS	inertial navigation system
LCL	lifting condensation level
LES	large-eddy simulation
LTS	lower troposphere stability
LWP	liquid-water path
MFS	mean-forcing simulation
MHS	mean-heating simulation
MMS	mean-moistening simulation
MLM	mixed-layer model

continued on next page

continued from previous page

NCAR	National Center for Atmospheric Research
NS	non-drizzling simulation
PBL	planetary boundary layer
POCs	pocket of open cells
RAMS	radome air-motion system
RF01	research flight 01
RF02	research flight 02
RF07	research flight 07
SST	sea surface temperature
STBL	stratocumulus-topped boundary layer
TKE	turbulence kinetic energy
UCLA LES	University of California Los Angeles large-eddy simulation

Bibliography

Ackerman, A. S., M. P. Kirkpatrick, D. E. Stevens, and O. B. Toon, 2004: The impact of humidity above stratiform clouds on indirect aerosol climate forcing. *Nature*, **432**, 1014–1017.

Ackerman, A. S., O. B. Toon, and P. V. Hobbs, 1993: Dissipation of marine stratiform clouds and collapse of the marine boundary layer due to the depletion of cloud condensation nuclei by clouds. *Science*, **262**, 226–229.

Ackerman, A. S., M. vanZanten, B. Stevens, V. Savic-Jovcic, C. S. Bretherton, A. Chlond, J.-C. Golaz, H. Jiang, M. Khairoutdinov, S. K. Krueger, D. C. Lewellen, A. Lock, C.-H. Moeng, K. Nakamura, M. Ovtchinnikov, M. D. Petters, J. R. Snider, S. Weinbrecht, and M. Zulauf, 2007: Large-eddy simulations of a drizzling, stratocumulus-topped marine boundary layer. *in preparation for Mon. Wea. Rev.*.

Agee, E. M., 1984: Observations from space and thermal convection: A historical perspective. *Bull. Amer. Meteor. Soc.*, **65**, 938–949.

Agee, E. M., T. S. Chen, and K. E. Dowell, 1973: A review of mesoscale cellular convection. *Bull. Amer. Meteor. Soc.*, **54**, 1004–1012.

Albrecht, B. A., 1989: Aerosols, cloud microphysics, and fractional cloudiness. *Science*, **245**, 1227–1230.

Bevington, P., 1969: *Data reduction and error analysis for the physical sciences*. McGraw-Hill Book Company, New York, 336 pp.

Bretherton, C. S., T. Uttal, C. W. Fairall, S. Yuter, R. Weller, D. Baumgardner, K. Comstock, R. Wood, and G. Raga, 2004: The epic 2001 stratocumulus study. *Bull. Amer. Meteor. Soc.*, **85**, 967–977.

Bretherton, C. S. and M. C. Wyant, 1997: Moisture transport, lower-tropospheric stability, and decoupling of cloud-topped boundary layers. *J. Atmos. Sci.*, **54**, 148–167.

Brost, R. A., D. H. Lenschow, and J. C. Wyngaard, 1982a: Marine stratocumulus layers. part i: Mean conditions. *J. Atmos. Sci.*, **39**, 800–817.

Brost, R. A., J. C. Wyngaard, and D. H. Lenschow, 1982b: Marine stratocumulus layers. part ii: Turbulence budgets. *J. Atmos. Sci.*, **39**, 818–836.

Brown, E. N., 1988: Position error calibration of a pressure survey aircraft using a trailing cone. Technical report, NCAR/TN-313+STR, NCAR Technical Note, Available from: http://www.library.ucar.edu/uhtbin/hyperion-image/DR000579.

Comstock, K. K., C. S. Bretherton, and S. E. Yuter, 2005: Mesoscale variability and drizzle in southeast pacific stratocumulus. *J. Atmos. Sci.*, **62**, 3792–3807.

Comstock, K. K., R. Wood, S. E. Yuter, and C. S. Bretherton, 2004: Reflectivity and rain rate in and below drizzling stratocumulus. *Quart. J. Roy. Met. Soc.*, **130**, 2891–2918, doi:10.1256/qj.03.187.

Comstock, K. K., S. E. Yuter, R. Wood, and C. S. Bretherton, 2007: The three-dimensional structure and kinematics of drizzling stratocumulus. *Mon. Wea. Rev.*, **135**, 3767–3784.

de Roode, S. R., P. G. Duynkerke, and H. J. J. Jonker, 2004: Large-eddy simulation: How large is large enough? *J. Atmos. Sci.*, **61**, 403–421.

Deardorff, J. W., 1980: Cloud top entrainment instability. *J. Atmos. Sci.*, **37**, 131–147.

Duynkerke, P. G., S. R. de Roode, M. C. van Zanten, J. Calvo, J. Cuxart, S. Cheinet, A. Chlond, H. Grenier, P. J. Jonker, M. Köhler, G. Lenderink, D. Lewellen, C.-L. Lappen, A. P. Lock, C.-H. Moeng, F. Müller, D. Olmeda, J.-M. Piriou, E. Sánchez, and I. Sednev, 2004: Observations and numerical simulations of the diurnal cycle of the eurocs stratocumulus case. *Quart. J. Roy. Met. Soc.*, **130**, 3269–3296.

Faloona, I., D. H. Lenschow, T. Campos, B. Stevens, M. C. vanZanten, B. Blomquist, D. Thornton, A. Bandy, and H. Gerber, 2005: Observations of entrainment in eastern pacific marine stratocumulus using three conserved scalars. *J. Atmos. Sci.*, **62**, 3268–3285.

Fu, Q. and K. N. Liou, 1993: Parameterization of the radiative properties of cirrus clouds. *J. Atmos. Sci.*, **50**, 2008–2025.

Garay, M. J., R. Davies, C. Averill, and J. A. Westphal, 2004: Actinoform clouds: Overlooked examples of cloud self-organization at the mesoscale. *Bull. Amer. Meteor. Soc.*, **85**, 1585–1594.

Gerber, H., G. Frick, S. P. Malinowski, J. L. Brenguier, and F. Burnet, 2005: Holes and entrainment in stratocumulus. *J. Atmos. Sci.*, **62**, 443–459.

Gultepe, I., A. J. Heymsfield, and D. H. Lenschow, 1990: A comparison of vertical velocity in cirrus obtained from aircraft and lidar divergence measurements during fire. *J. Atmos. Oceanic Technol.*, **7**, 58–67.

Jensen, J. B., S. Lee, P. B. Krummel, J. Katzfey, and D. Gogoasa, 2000: Precipitation in marine cumulus and stratocumulus.: Part i: Thermodynamic and dynamic observations of closed cell circulations and cumulus bands. *Atmos. Res.*, **54**, 117–155.

Jonker, H. J. J., P. G. Duynkerke, and J. W. M. Cuijpers, 1999: Mesoscale fluctuations in scalars generated by boundary layer convection. *J. Atmos. Sci.*, **56**, 801–808.

Khairoutdinov, M. and Y. Kogan, 2000: A new cloud physics parameterization in a large-eddy simulation model of marine stratocumulus. *Mon. Wea. Rev.*, **128**, 229–243.

Klein, S. A. and D. L. Hartmann, 1993: The seasonal cycle of low stratiform clouds. *J. Climate*, **6**, 1587–1606.

Klein, S. A., D. L. Hartmann, and J. R. Norris, 1995: On the relationships among low-cloud structure, sea surface temperature, and atmospheric circulation in the summertime northeast pacific. *J. Climate*, **8**, 1140–1155.

Lenschow, D. H., 1986: Aircraft measurements in the boundary layer. *Probing the Atmospheric Boundary Layer*, D. H. Lenschow, ed., American Meteorological Society, Boston, MA, 39–55.

Lenschow, D. H., P. B. Krummel, and S. T. Siems, 1999: Measuring entrainment, divergence, and vorticity on the mesoscale from aircraft. *J. Atmos. Oceanic Technol.*, **16**, 1384–1400.

Lenschow, D. H., V. Savic-Jovcic, and B. Stevens, 2007: Divergence and vorticity from aircraft air motion measurements. *J. Atmos. Oceanic Technol.*, **24**, 2062–2072.

Lilly, D. K., 1968: Models of cloud topped mixed layers under a strong inversion. *Quart. J. Roy. Met. Soc.*, **94**, 292–309.

MacVean, M. K. and P. J. Mason, 1990: Cloud-top entrainment instability through small-scale mixing and its parameterization in numerical models. *J. Atmos. Sci.*, **47**, 1012–1030.

Medeiros, B., A. Hall, and B. Stevens, 2005: What controls the mean depth of the pbl? *J. Climate*, **18**, 3157–3172.

Nicholls, S., 1984: The dynamics of stratocumulus: aircraft observations and comparisons with a mixed layer model. *Quart. J. Roy. Met. Soc.*, **110**, 783–820.

Ogura, Y. and N. A. Phillips, 1962: Scale analysis of deep and shallow convection in the atmosphere. *J. Atmos. Sci.*, **19**, 173–179.

Orlanski, I., 1975: Rational subdivision of scales for atmospheric processes. *Bull. Amer. Meteor. Soc.*, **56**, 527–530.

Paluch, I. R. and D. H. Lenschow, 1991: Stratiform cloud formation in the marine boundary layer. *J. Atmos. Sci.*, **48**, 2141–2158.

Petters, M. D., J. R. Snider, B. Stevens, G. Vali, I. Faloona, and L. M. Russell, 2006: Accumulation mode aerosol, pockets of open cells, and particle nucleation in the remote subtropical pacific marine boundary layer. *J. Geophys. Res.*, **111**, doi:D02206, doi:10.1029/2004JD005694.

Pincus, F. and M. B. Baker, 1994: Effect of precipitation on the albedo susceptibility of clouds in the marine boundary layer. *Nature*, **372**, 250–252.

Randall, D. A., 1980: Conditional instability of the first kind upside-down. *J. Atmos. Sci.*, **37**, 125–130.

Rogers, R. R. and M. K. Yau, 1989: *A Short Course in Cloud Physics*. Butterworth-Heinemann, Oxford, UK, 3rd edition, 290 pp.

Savic-Jovcic, V. and B. Stevens, 2007: The structure and mesoscale organization of precipitating stratocumulus. *J. Atmos. Sci.*, in press.

Schmidt, H. and U. Schumann, 1989: Coherent structure of the convective boundary layer derived from large-eddy simulations. *J. Fluid Mech.*, **200**, 511–562.

Seifert, A. and K. Beheng, 2001: A double-moment parameterization for simulating autoconversion, accretion and selfcollection. *Atmos. Res.*, **59-60**, 265–281.

Seifert, A. and K. D. Beheng, 2006: A two-moment cloud microphysics parameterization for mixed-phase clouds. part 1: Model description. *Meteor. Atmos. Phys.*, **92**, 45–66.

Sharon, T. M., B. A. Albrecht, H. H. Jonsson, P. Minnis, M. M. Khaiyer, T. M. van Reken, J. Seinfeld, and R. Flagan, 2006: Aerosol and cloud microphysical characteristics of rifts and gradients in maritime stratocumulus clouds. *J. Atmos. Sci.*, **63**, 983–997.

Siebesma, A. P., C. S. Bretherton, A. Brown, A. Chlond, J. Cuxart, P. G. Duynkerke, H. Jiang, M. Khairoutdinov, D. Lewellen, C.-H. Moeng, E. Sanchez, B. Stevens, and D. E. Stevens, 2003: A large eddy simulation intercomparison study of shallow cumulus convection. *J. Atmos. Sci.*, **60**, 1201–1219.

Slingo, A., 1990: Sensitivity of the earth's radiation budget to changes in low clouds. *Nature*, **343**, 49–51.

Stevens, B., 2000: Cloud transition and decoupling in shear-free stratocumulus-topped boundary layers. *Geophys. Res. Lett.*, **27**, 2557–2560.

— 2002: Entrainment in stratocumulus-topped mixed layers. *Quart. J. Roy. Met. Soc.*, **128**, 2663–2690.

— 2004: Atmospheric moist convection. *Annu. Rev. Earth Planet. Sci.*, submitted.

— 2006: Bulk boundary-layer concepts for simplified models of tropical dynamics. *Theor. Comput. Fluid Dyn.*, **20**, 279–304, doi:10.1007/s00162-006-0032-z.

Stevens, B., W. R. Cotton, G. Feingold, and C.-H. Moeng, 1998: Large-eddy simulations of strongly precipitating, shallow, stratocumulus-topped boundary layer. *J. Atmos. Sci.*, **55**, 3616–3638.

Stevens, B., D. H. Lenschow, I. Faloona, C.-H. Moeng, D. K. Lilly, B. Blomquist, G. Vali, A. Bandy, T. Campos, H. Gerber, S. Haimov, B. Morley, and D. Thornton, 2003a: On entrainment rates in nocturnal marine stratocumulus. *Quart. J. Roy. Met. Soc.*, **129**, 3469–3493.

Stevens, B., D. H. Lenschow, G. Vali, H. Gerber, A. Bandy, B. Blomquist, J. L. Brenguier, C. S. Bretherton, F. Burnet, T. Campos, S. Chai, I. Faloona, D. Friesen, S. Haimov, K. Laursen, D. K. Lilly, S. M. Loehrer, S. P. Malinowski, P. Szymon, B. Morely, M. D. Petters, D. C. Rogers, L. Russell, V. Savic-Jovcic, J. R. Snider, D. Straub, M. J. Szumowski, H. Takagi, D. C. Thorton, M. Tschudi, C. Twohy,

M. Wetzel, and M. C. van Zanten, 2003b: Dynamics and chemistry of marine stratocumulus - DYCOMS-II. *Bull. Amer. Meteor. Soc.*, **84**, 579–593.

Stevens, B., C.-H. Moeng, A. S. Ackerman, C. S. Bretherton, A. Chlond, S. de Roode, J. Edwards, J.-C. Golaz, H. Jiang, M. Khairoutdinov, M. P. Kirkpatrick, D. C. Lewellen, A. Lock, F. Muller, D. E. Stevens, E. Whelan, and P. Zhu, 2005a: Evaluation of large-eddy simulations via observations of nocturnal marine stratocumulus. *Mon. Wea. Rev.*, **133**, 1443–1462.

Stevens, B., G. Vali, K. Comstock, R. Wood, M. C. vanZanten, P. H. Austin, C. S. Bretherton, and D. H. Lenschow, 2005b: Pockets of open cells (POCs) and drizzle in marine stratocumulus. *Bull. Amer. Meteor. Soc.*, **86**, 51–57.

Turton, J. D. and S. Nicholls, 1987: A study of the diurnal variation of stratocumulus using a multiple mixed layer model. *Quart. J. Roy. Met. Soc.*, **113**, 969–1009.

Vali, G., R. D. Kelly, J. French, S. Haimov, D. Leon, R. E. McIntosh, and A. Pazmany, 1998: Finescale structure and microphysics of coastal stratus. *J. Atmos. Sci.*, **51**, 773–384.

vanZanten, M. C. and B. Stevens, 2005: Observations of the structure of heavily precipitating marine stratocumulus. *J. Atmos. Sci.*, **62**, 4327–4342.

vanZanten, M. C., B. Stevens, G. Vali, and D. H. Lenschow, 2005: Observations of drizzle in nocturnal marine stratocumulus. *J. Atmos. Sci.*, **62**, 88–106.

Wood, R. and D. L. Hartmann, 2006: Spatial variability of liquid water path in marine low cloud: The importance of mesoscale cellular convection. *J. Climate*, **19**, 1748–1764.

Xue, H., G. Feingold, and B. Stevens, 2007: Aerosol effects on clouds, precipitation, and the organization of shallow cumulus convection. *J. Atmos. Sci.*, in press.

Zhang, Y., B. Stevens, and M. Ghil, 2005: On the diurnal cycle and susceptibility to aerosol concentration in a stratocumulus-topped mixed layer. *Quart. J. Roy. Met. Soc.*, **131**, 1567–1583.